Aerospace Engineering Sciences Graduate Theses & Dissertations

Aerospace Engineering Sciences

Spring 1-1-2014

Structural Stability of Asteroids

Masatoshi Hirabayashi
University of Colorado Boulder, masatoshi.hirabayashi@colorado.edu

Structural Stability of Asteroids

by

Toshi Hirabayashi

B.A., Nagoya University, 2007

M.S., University of Tokyo, 2010

M.S., University of Colorado, 2013

A thesis submitted to the

Faculty of the Graduate School of the

University of Colorado in partial fulfillment

of the requirements for the degree of

Doctor of Philosophy

Department of Aerospace Engineering Sciences

2014

This thesis entitled:
Structural Stability of Asteroids
written by Toshi Hirabayashi
has been approved for the Department of Aerospace Engineering Sciences

_____

Prof. Daniel J. Scheeres

_____

Prof. Carlos Felippa

Date _____

The final copy of this thesis has been examined by the signatories, and we find that both the content and the form meet acceptable presentation standards of scholarly work in the above mentioned discipline.

Hirabayashi, Toshi (Ph.D., Aerospace Engineering Sciences)

Structural Stability of Asteroids

Thesis directed by Prof. Prof. Daniel J. Scheeres

This thesis develops a technique for analyzing the internal structure of an irregularly shaped asteroid. This research focuses on asteroid (216) Kleopatra, a few-hundred-kilometer-sized main belt asteroid spinning about its maximum moment of inertia axis with a rotation period of 5.385 hours [97], to motivate the techniques. While Ostro et al. [117] reported its dog bone-like shape, estimation of its size has been actively discussed. There are at least three different size estimates: Ostro et al. [117], Descamps et al. [36], and Marchis et al. [102]. Descamps et al. [36] reported that (216) Kleopatra has satellites and obtained the mass of this object. This research consists of determination of possible failure modes of (216) Kleopatra and its subsequent detailed stress analysis, with each part including an estimation of the internal structure. The first part of this thesis considers the failure mode of Kleopatra and evaluates the size from it. Possible failure modes are modeled as either material shedding from the surface or plastic failure of the internal structure. The surface shedding condition is met when a zero-velocity curve with the same energy level as one of the dynamical equilibrium points attaches to the surface at the slowest spin period, while the plastic failure condition is characterized by extending the theorem by Holsapple (2008) that the yield condition of the averaged stress over the whole volume is identical to an upper bound for global failure. The prime result shows that while surface shedding does not occur at the current spin period and thus cannot result in the formation of the satellites, the neck may be situated near its plastic deformation state. From the failure condition, we also find that the size estimated by Descamps et al. (2011) is the most structurally stable. The second part of this thesis discusses finite element analyses with an assumption of an elastic-perfectly plastic material and a non-associated flow rule. The yield condition is modeled as the Drucker-Prager yield criterion, which is a smooth shear-pressure dependent condition. The result shows that the failure mode highly depends on

the body size. As the body size increases, the failure mode transits from a compression-oriented mode to a tension-oriented mode. This asteroid should have a cohesive strength of at least 200 kPa to keep its original shape, although we argue that its cohesion may be less. In addition, the upper bound technique for structural failure and the dynamical analysis for surface shedding are also applied to 21 different shapes to determine their failure modes (either surface shedding or structural failure) on the assumption of zero-cohesion. Finally, we apply these concepts to analyze the breakup event of main belt comet P/2013 R3.

Acknowledgements

The author thanks Dr. Keith A. Holsapple for his dedicated support in helping to develop the present technique.

Contents

Chapter

Tables

Table

Figures

Figure

Chapter 1

Introduction

1.1   Research Background

In the last few decades, scientists have revealed that many asteroids have unique characteristics. The most remarkable feature of these asteroids includes (i) that they are gravitational aggregations of small geological materials, usually called rubble piles, and (ii) that they have their unique shapes.

One of the remarkable examples is (25143) Itokawa, a near-earth asteroid with dimensions of 535 m by 294 m by 209 m, which was observed by the Hayabusa spacecraft (ISAS/JAXA) [48]. As seen in Fig. 1.1, Itokawa is a rubble pile and its shape looks like a peanut. Currently, scientists believe that the shape of Itokawa came from a catastrophic collision of its parent body followed by a soft contact of two aggregates [48]. The bulk density of this object is estimated as 1.9 g/cm^3 [48], which is much lower than the material densities of geological materials, and the porosity reaches up to 40 % [1]. The Hayabusa spacecraft brought the Itokawa sample to the Earth in 2010, and the sample included particles with sizes ranging from 1 μm to 100 μm [180].

Rubble pile asteroids change their configuration over their lifetime due to several different effects. Such a process may be through their mutual, catastrophic impacts. This causes them to scatter, to re-accumulate, and to form a new configuration. The time scale of an accretion process due to a catastrophic impact is probably less than several days [106], negligibly shorter than the life time of asteroids. The collisional probability of a main belt asteroid larger than 50 km in diameter is 2.86×10^{-18} km^{-2} yr^{-1}, while that of a near-earth asteroid is 15.34×10^{-18} km^{-2} yr^{-1} [11, 10].

Another possibility is the YORP effect, solar radiation torque that causes an asteroid to have a semi-static spin-up and to change its structural figurations (e.g., [134, 181]). Remarkable examples of the latter case are active asteroids P/2013 P5 [83] and P/2013 R3 [82]. P/2013 P5 includes a 0.24 ± 0.04 km radius nucleus that is losing mass probably due to rotational instability (Fig. 1.2), while P/2013 R3 is breaking up into multiple components (Fig. 1.3). Interestingly, the spin states of many asteroids are very close to the gravitational bound [127]; therefore, such failure modes may be common in our solar system.

However, regardless of scientists' efforts in developing theoretical and numerical models, the mechanisms of these configuration changes have been poorly understood. Since the late 1800s, elastic analyses have been popular to study the stress state of the internal body (e.g., [30, 31, 94, 37, 185]). The main issue of elastic theory, however, is that the elastic solutions ignore any possibility of residual stresses and therefore do not include all possible equilibrium stress states.

Recently, theoretical developments using plastic theory have made some contributions to understanding permanent deformations of rubble pile asteroids. Davidsson [34] considered the zero-tension condition of stress-average over a cross section to determine the condition when a body experiences catastrophically permanent deformation somewhere (later, known as structural failure). Holsapple [70] used limit analysis to construct a condition at which upper and lower bounds for structural failure of a uniformly rotating ellipsoid are the same. Holsapple [63] developed a technique for taking moments of the stress equilibrium equation and confirmed that this averaging technique gave the same solutions as his limit analysis method [70]. Holsapple [64] analyzed the condition of structural failure with cohesion to explain the mechanism of the gravitational barrier [127]. Holsapple [65] numerically investigated the relation between actual structural failure and limit analysis for a rod, a disk, and an ellipsoid.

Numerical techniques have also been developed to better understand the formations of fluid bodies and rubble asteroids. Eriguchi et al. [42] studied deformation processes of a uniformly rotating incompressible fluid ellipsoid. Using a soft-sphere discrete element method, Sánchez and Scheeres [137] analyzed shape changes of a sphere and of an ellipsoid due to a YORP-type spin-up.

The mechanisms of re-aggregation after a high-velocity impact have also been studied (e.g. [105], [104], and [41]).

For the mechanism of surface shedding, scientists have preferred to use dynamical analyses. Scheeres [146] revealed that as an increment of the total angular momentum causes surface particles to move to a different stable spot. Guibout and Scheeres [52] investigated stability of the motion of a particle on the surface of a uniformly rotating ellipsoid. Note that these analyses implicitly assume zero-cohesion.

1.2   Size Uncertainty and Formation of (216) Kleopatra

These earlier analyses focused on simple shapes such as spheres and ellipsoids. However, as seen in Fig. 1.1, the shape of an asteroid is neither a sphere nor an ellipsoid. The main purpose of this research is to develop a technique for evaluating the shape effect of an asteroid on its failure condition due to rotational instability.

Asteroid (216) Kleopatra, classified as a M-type in the Tholen taxonomy [176] or as a Xe-type in the Bus taxonomy [17], has been of interest for the last few decades because of its odd shape and fast spin period (Figs. 1.4 and 1.5). Since it is orbiting in the main belt and asteroids of this type have not been targeted yet, this asteroid has not been well understood. Although we have significant information on (216) Kleopatra including the shape, the spin period, and the mass (Table 1.1), not as certain, and subject to different interpretations, is its total size. In addition, since this asteroid was also observed to have satellites [36], scientists have been interested in their formation as well.

1.2.1   History of Observations

Past researches have investigated the shape of this asteroid with different observational techniques. From lightcurve observations, Scaltrity and Zappalá [138] confirmed shape elongation of this asteroid and small differences of the magnitudes at the maxima and the minima (see Fig.4 in their paper). They pointed out that those differences came from either different reflectivity

or a shadowing effect. Weidenschilling [186] argued that (624) Hektor might be a nearly contact binary that is in its hydrostatic stable equilibrium. Then, with this model, he concluded that (216) Kleopatra has a (624) Hektor-like lightcurve and an amplitude of 3.3 slightly exceeds the value of a contact binary, but a contact binary model with its spin period recovers a reasonable density of 3.9 g/cm^3. Lightcurve observations by Zappalá et al. [196] revealed that a triaxial ellipsoid model fits their observations. On the other hand, Cellino et al. [23] found that a binary model is compatible with their lightcurve data. They also pointed out that the amplitude, 0.9, by Zappalá et al. [196] is an estimation, while the amplitude of this asteroid highly depends on the phase. Occultations by Dunham et al. [39] estimated the size dimensions to be 230 km by 55 km. Furthermore, Mitchell et al. [109] performed radar observations; however, although they obtained the Kleopatra echoes which are similar to those of bifurcated asteroid (4769) Castalia, their coarse data set precluded them from determining the shape. They also attempted to detect the shape from occultation data; however, since the model used was simplistic, they could obtain no evidence for a bifurcation.

From comprehensive radar observations, Ostro et al. [117] constructed a three-dimensional bi-lobed polyhedral shape model with dimensions of 217 km by 94 km by 81 km, although they indicated that the absolute size uncertainty was up to 25 %. On the other hand, from the Fine Guidance Sensors (FGS) aboard HST, Tanga et al. [174] confirmed that their shape model is consistent with radar observations by Ostro et al. [117]. Hestroffer et al. [56] showed that a larger and more elongated model is consistent with the occultations, the photometric and the interferometric HST/FGS results. Adaptive optics observations by Hestroffer et al. [57] showed that their model is consistent with the Ostro et al. model, although these observations could not rule out the possibility that this asteroid is a binary asteroid. With the binary model by Cellino et al. [23], the contact binary model by Tanga et al. [174], and the polyhedron model by Ostro et al. [117], Takahashi et al. [173] performed lightcurve simulations to report that while the binary model and the contact binary model fit their lightcurve simulations, the Ostro et al. model could not. It is worth noting that for simulations using the Ostro et al. model, they used the size estimated by Ostro et al. [117], which may be smaller than the actual size.

1.2.2 Exact Mass and Size Uncertainties

From the mutual gravity interaction between (216) Kleopatra and its satellites, Descamps et al. [36] calculated the mass as 4.64×10^{18} kg. Kaasalainen and Viikinkoski [86] attempted to construct a new shape model with multiple observation data (photometry, adaptive optics, occultation timings, and interferometry); however, they mentioned that the data were not compatible and thus further analyses are necessary. We look forward to their new shape model.

In contrast to the exact mass by Descamps et al. [36], there is an uncertainty of the size estimations. So far, at least three estimates have been reported. Ostro et al. [117] estimated the equivalent diameter[1] as 108.6 km by radar observations and the surface bulk density as 3.5 g/cm^3 from the surface reflectivity. Note that the latest version of the shape model provides a volume of 7.09×10^5 km^3, which is equal to an equivalent diameter of 111.1 km. Tedesco et al. [175] reported the IRAS equivalent diameter as 135.07 km, while the estimation by Descamps et al. [36] is consistent with the Tedesco et al. size [175]. On the other hand, from observations with Spitzer/IRS, Marchis et al. [102] derived the equivalent diameter as 152.5 km by the Near-Earth Asteroid Thermal Model (we referred to Table 5 in their paper). Figure 1.6 shows the comparison between the estimated size scale and the bulk density. Scale size means an equivalent diameter relative to that of the Ostro et al. (2000) size, i.e., 55.3 km [117]. The Ostro et al. (2000) size is 1.00, the Descamps et al. (2011) size is 1.22, and the Marchis (2012) et al. size is 1.37. For the Ostro et al. (2000) estimation, we only show the error bar of the size scale (the region of the horizontal axis). Note that the Ostro et al. (2000) density is based on their surface reflectivity estimation.

From these backgrounds, it seems that the Ostro et al. (2000) shape has been confirmed by other researches, but that the size has not. Given a constant mass, variations in the size cause (216) Kleopatra to have different densities, stronger centrifugal forces and weaker gravitational forces. Because of its fast spin period, as the size increases, the internal structure becomes closer to structural failure. This study investigates possible failure modes of (216) Kleopatra dynamically

---

[1] An equivalent diameter is a diameter of a sphere with the same volume as the shape.

and structurally with hope for evaluating the size. Here, the shape is fixed as the Ostro et al. (2000) shape.

1.2.3   Satellite Formation

(216) Kleopatra was observed to have two small satellites (Table 1.2) [36]. To obtain relevant orbit solutions for the satellites, Descamps et al. [36] gave a hypothesis that the orbital planes of the satellites are parallel to the equatorial plane of (216) Kleopatra[2] . They also pointed out that these satellites might result from surface shedding, although the detailed analysis has not been reported yet. The present study investigates a possible formation scenario of these satellites.

1.3   Research Goal and Outlines

The goal of this research includes (i) a better understanding of a possible failure mode of (216) Kleopatra, (ii) a determination of a structurally stable size of this body, and (iii) an investigation into possible formations of its small satellites. We consider surface shedding and structural failure (defined in the later sections) to be common failure modes and investigate these conditions for (216) Kleopatra. The condition of surface shedding is determined by zero-velocity curves, which are quasi-energy contours. On the other hand, the condition of structural failure is obtained by limit analysis, a technique for giving lower and upper bound conditions, and by finite element analysis. For a calculation of an upper bound, we assume that (216) Kleopatra is symmetric about the principal moment of inertia axes.

We focus on (216) Kleopatra to establish analytical techniques. This study is organized as follows. First, we introduce a method for obtaining the spin period of surface shedding (Chapter 2). Second, we discuss techniques for determining lower and upper bound conditions for structural failure (Chapter 3). Third, we develop a finite element analysis technique for calculating a more precise failure condition (Chapter 4). Then, we investigate (i) a structurally stable size of (216)

---

[2] With the data of stellar occultations in 1980, they could interpret the reported secondary event from their simple solution (Descamps, 2013, personal communication).

Kleopatra, (ii) a possible formation scenario of its satellites, and (iii) detailed failure modes of this object (Chapter 5). The present technique will enable us to give stronger constraints on its internal structure once further observations are carried out.

The technique is also applied to other objects. First, we use the upper bound technique and the dynamical analysis established here to determine the failure modes of 21 different shapes on the assumption of zero-cohesion (Section 6). Second, main belt comet P/2013 R3 has undergone a recent breakup event, and we give constraints on the internal structure based on this event (Section 7).
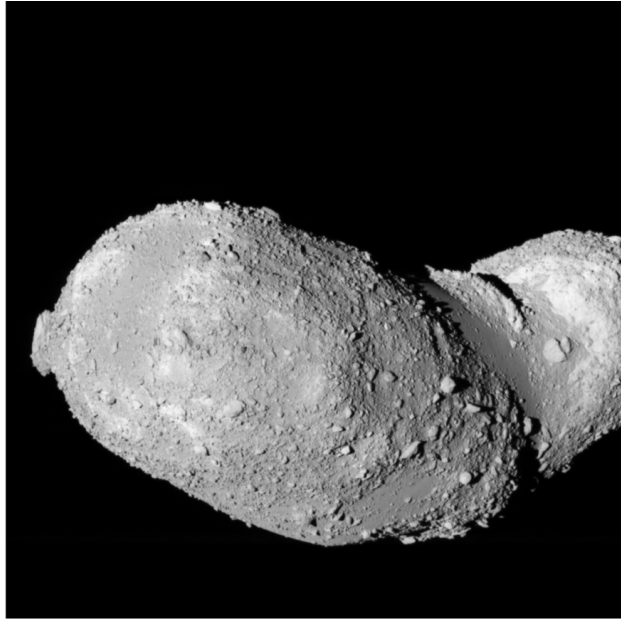
Figure 1.1: Image of (25143) Itokawa taken by the Hayabusa spacecraft (ISAS/JAXA).
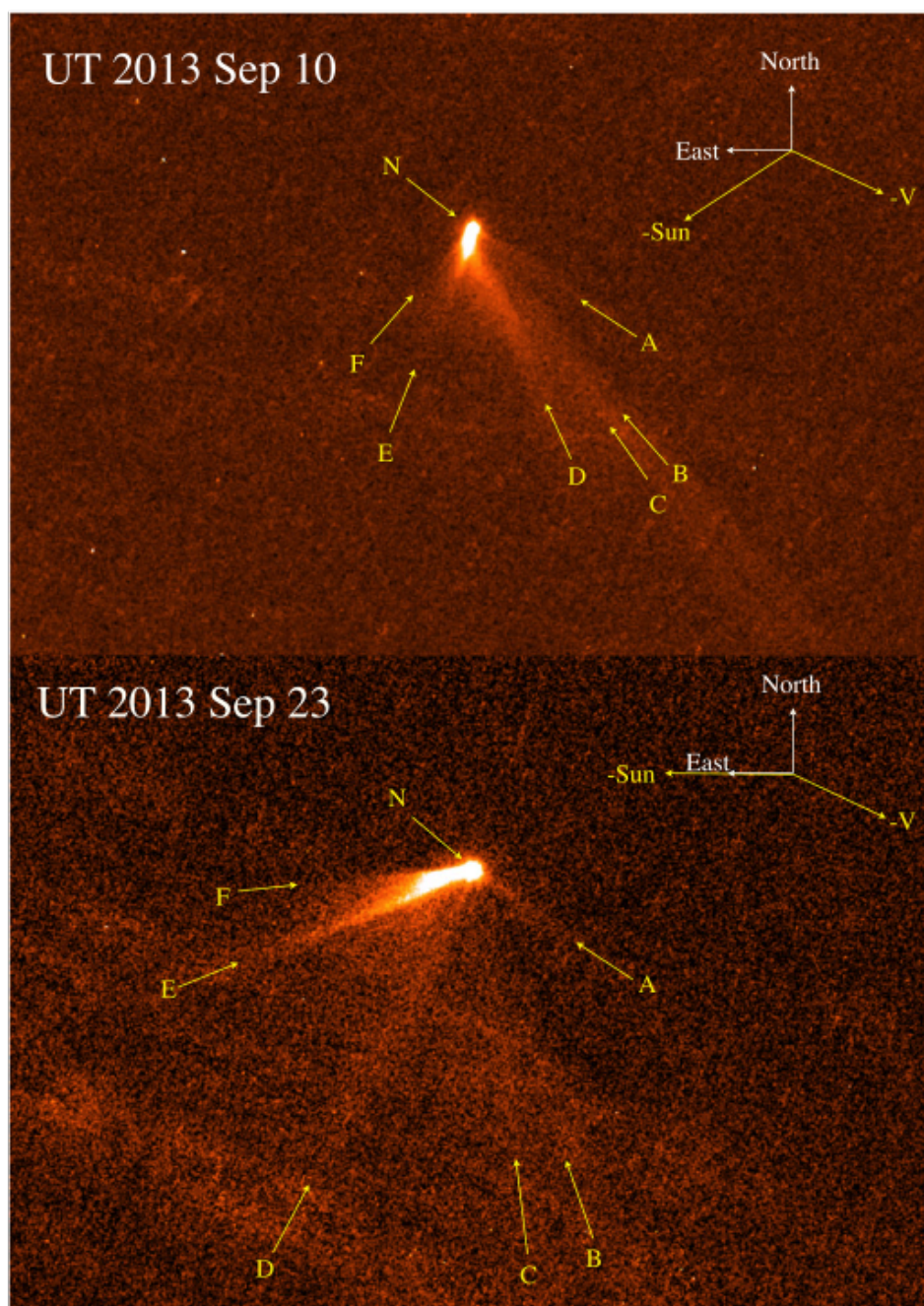
Figure 1.2: Mass loss of P/2013 P5 [83].
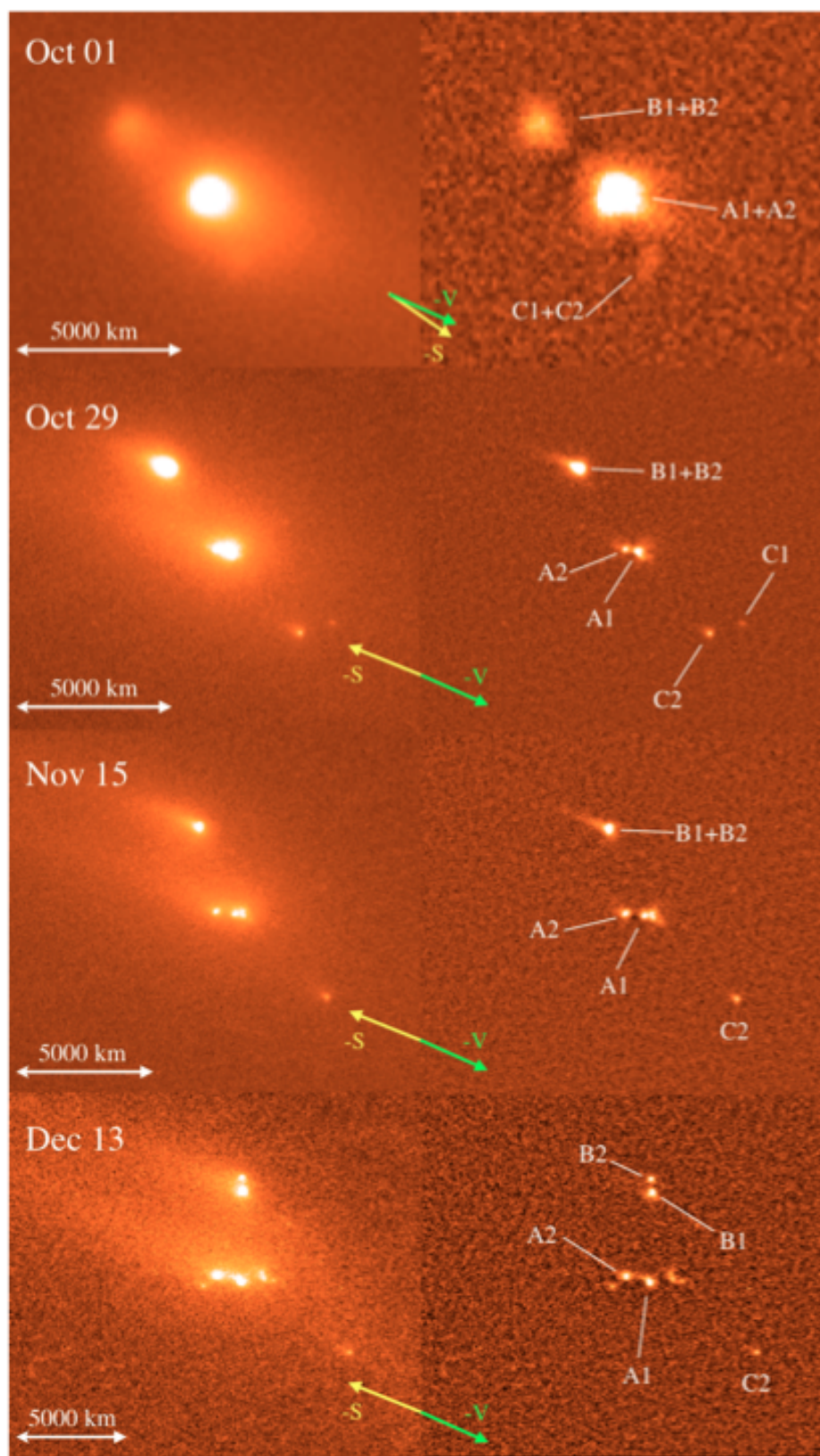
Figure 1.3: Breakup mode of P/2013 R3 [82].
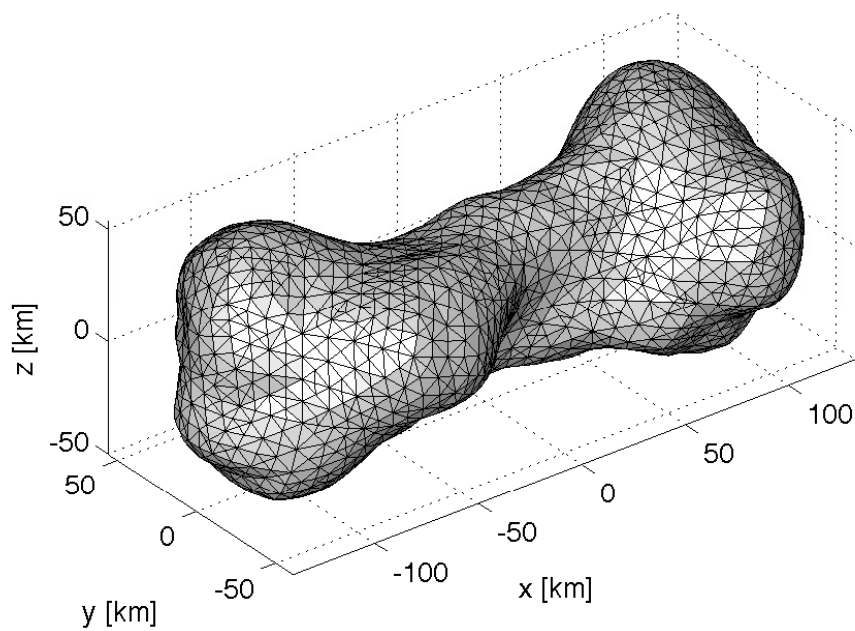
Figure 1.4: Three-dimensional shape of (216) Kleopatra by Ostro et al. [117]. This shape model consists of surface points (vertices) and the order of surface elements (faces). The size scale of this plot is 1.22, i.e., the Descamps et al. (2011) size.
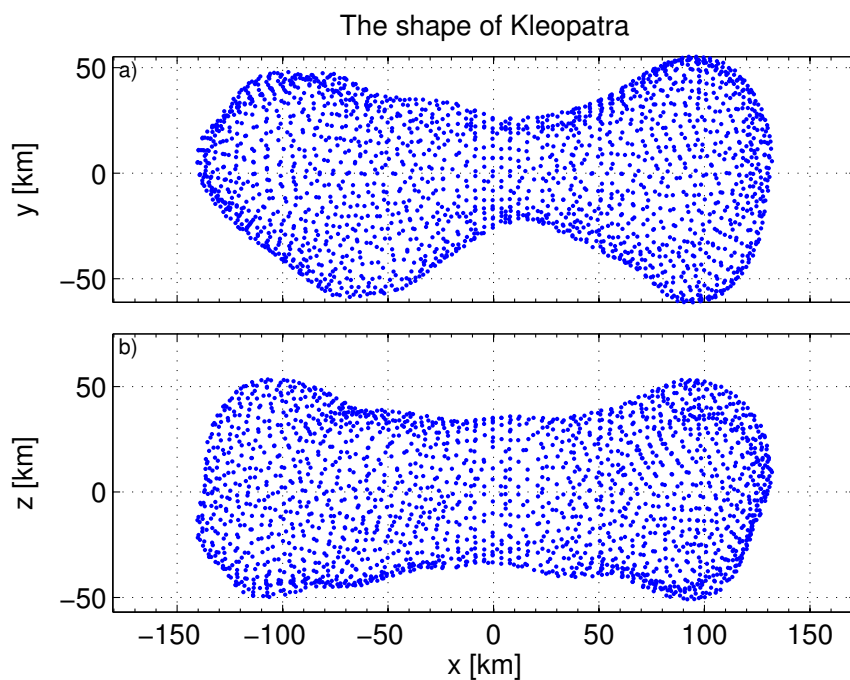
Figure 1.5: Projection of (216) Kleopatra. The upper plot shows the projection onto the $x - y$ plane, while the lower plot is that onto the $x - z$ plane. The x, y, and z axes correspond to the minimum, intermediate, and maximum moment of inertia axes, respectively. Similar to Fig. 1.4, the size scale of these plots is the same as the Descamps et al. (2011) size.
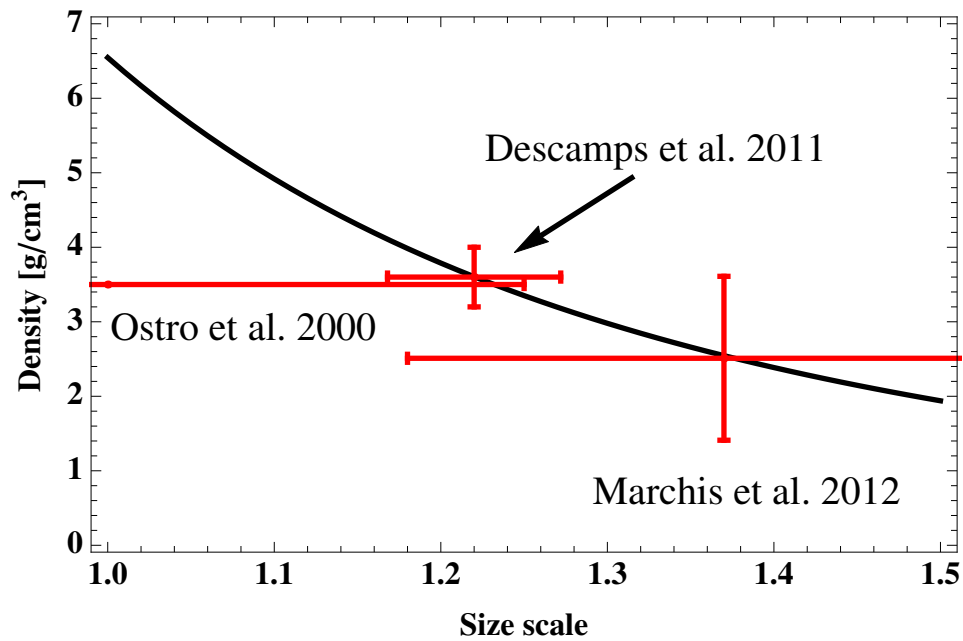
Figure 1.6: Relation between the size scale and the density. Given a constant mass of 4.64×10^{18} kg [36] and a constant shape [117], the curve describes the ideal density as a function of the size scale. The actual density and size scale should be on this curve. The error bars show observational values by Ostro et al. [117], Descamps et al. [36], and Marchis et al. [102].

Table 1.1: Constant properties of (216) Kleopatra

Property	Value	Units	Reference
Mass	4.64×10^{18}	kg	[36]
Period	5.385	hr	[97]
Shape	-	-	[117]

Table 1.2: Physical properties of (216) Kleopatra's satellites. The spin pole of (216) Kleopatra is given as $\lambda = 76 \pm 3°$ and $\beta = 16 \pm 1°$ in J2000 ecliptic coordinates [36].

Property	Satellite (outer)	Satellite (inner)
Diameter [km]	8.9 ± 1.6	6.9 ± 1.6
Orbital period [days]	2.32 ± 0.02	1.24 ± 0.02
Semi-major axis [km]	678 ± 13	454 ± 6
Orbit pole right ascension [deg]	74 ± 2	79 ± 2
Orbit pole declination [deg]	16 ± 1	16 ± 1

Chapter 2

Surface Shedding

This chapter introduces a method for determining the spin condition of surface shedding. A change of the size of (216) Kleopatra causes a variation of the gravitational and centrifugal forces. Thus, the location of the dynamical equilibrium points[1] also move. The present study assumes the shape of (216) Kleopatra to be constant. We first introduce the definition of surface shedding. Then, we discuss a technique for determining the spin condition of surface shedding.

2.1 Definition

Consider a uniformly rotating rubble pile asteroid affected by gravitational and centrifugal forces. Surface shedding is a process where small particles on the surface are shed due to the centrifugal force exceeding the gravitational force (Fig.2.1). This first occurs when a dynamical equilibrium point off the asteroid touches the asteroid surface. This condition is considered to be a necessary condition of surface shedding.

We use the method by Guibout and Scheeres [52] to determine the spin condition of surface shedding. The Guibout and Scheeres method [52] considered the stability of motion of a massless particle on a rotating ellipsoid by the following methods. The first technique was a linear stability analysis about the dynamical equilibrium points on the surface, and the second technique was to analyze Hill's stability by zero-velocity curves.

Surface shedding and landslides may be related. This fact may cause the actual spin of surface

---

[1] Dynamical equilibrium points are the points where all the external forces are balanced.

shedding to be earlier than the condition calculated by the present technique. Landslides could occur if a plastic flow propagates over a plane beneath, but near, the surface [91, 55]. Considering the effect of landslides on the stability of an asteroid's shape, Minton [108] and Harris et al. [54] explained the formation of equatorial ridges on an asteroid (e.g., 1999 KW4). However, the major issue of their studies was that their analyses reach a singular point on the equator of a body. Walsh et al. [183] reported that the YORP effect could cause landslides, which may shed small particles from the surface, and a secondary body could gravitationally form in the cloud of these particles.

Although these studies imply strong correlations between surface shedding and landslides, we do not consider the effects of landslides on the first spin of surface shedding in this study. It means that the condition calculated here becomes more conservative than the actual condition. Our future work will improve this aspect of our research.

2.2   Methods for Determining Surface Shedding

Classically, the gravity slope analysis that determines the direction of the total force acting on small elements on the surface has been used to analyze surface conditions (e.g., [119]). The direction is given as the angle between the force direction and the normal vector pointing inward. Consider the gravity slope at some point on the surface. If the angle is $0°$, a small particle sitting on there does not move from the original point. As the angle increases, it could start moving from this point. Once this angle reaches $90°$, the small particle is about to take off the surface.

This study tracks the locations of the dynamical equilibrium points to determine the condition where one of these points attaches to the surface first. This method has an advantage in terms of clear visualizations of (i) the location of surface shedding and (ii) the trajectories of small particles. Specifically, we calculate the locations of the dynamical equilibrium points and obtain the zero-velocity curves on the equatorial plane. This section introduces the technique for obtaining the locations of the dynamical equilibrium points and the zero-velocity curves on the equatorial plane. We use the Scheeres method [150] to calculate the zero-velocity curves about an irregular shape.

2.2.1 Zero-Velocity Curves and Dynamical Equilibrium Points

Consider an irregular body uniformly spinning about its maximum moment of inertia axis. $\boldsymbol{r} = (x, y, z)$ and $\boldsymbol{v}$ are a position vector and a velocity vector in a frame rotating with the body, respectively. ω is the angular velocity of the spin. Dots over a letter indicate time derivatives. The absolute value of $\boldsymbol{v}$ is denoted as v. The x, y, and z axes lie along the minimum, intermediate, and maximum moment of inertia axes, respectively.

On the assumption that only the gravitational and centrifugal forces affect the orbital motion of a small particle, the equation of motion is written as

$$
\begin{aligned}
\ddot{x} - 2\omega\dot{y} &= -U_x(\boldsymbol{r}) + \omega^2 x, \\
\ddot{y} + 2\omega\dot{x} &= -U_y(\boldsymbol{r}) + \omega^2 y, \\
\ddot{z} &= -U_z(\boldsymbol{r}),
\end{aligned}
\tag{2.1}
$$

where U is the gravitational potential and the subscripts of U mean the partial derivatives with respect to position. The Jacobi integral $J(\boldsymbol{r}, \boldsymbol{v})$ is given as

$$
J(\boldsymbol{r}, \boldsymbol{v}) = \frac{1}{2}v^2 - \frac{1}{2}\omega^2(x^2 + y^2) + U(\boldsymbol{r}).
\tag{2.2}
$$

For a given value of the Jacobi integral C, the following inequality is obtained:

$$
C + \frac{1}{2}\omega^2(x^2 + y^2) - U(\boldsymbol{r}) \geq 0.
\tag{2.3}
$$

This inequality comes from $v^2 \geq 0$ and indicates constraints on the motion of a small particle as a function of position. In other words, a small particle is prohibited to enter any areas where this inequality is violated.

Define the function of $f(\boldsymbol{r}) = \omega^2(x^2 + y^2)/2 - U(\boldsymbol{r}) \geq 0$. Then, Eq. (2.3) becomes $f(r) \geq -C$, which provides constraints on where motion can occur. If $C \geq 0$, there are no constraints. However,

if C is negative, the motion may be constrained. Define an equilibrium point $\boldsymbol{r}_1$ such that

$$
\begin{aligned}
U_x(\boldsymbol{r}_1) - \omega^2 x &= 0, \\
U_y(\boldsymbol{r}_1) - \omega^2 y &= 0, \\
U_z(\boldsymbol{r}_1) &= 0.
\end{aligned}
\tag{2.4}
$$

We denote the Jacobi integral at $\boldsymbol{r}_1$ as C_1. We extend this discussion to other equilibrium points $\boldsymbol{r}_i$ for $i = 1, ..., n$, where n is the total number of the equilibrium points in the system. If $\boldsymbol{r}_i$ is an extremum, when $C > C_i$, the motion is restricted on the place centered at $\boldsymbol{r}_i$. On the other hand, if $\boldsymbol{r}_i$ is a saddle point, as $C(< C_i)$ comes close to and is finally equal to C_i, non-allowable regions connect with each other at this point. We define the indices of the dynamical equilibrium points so that $f(\boldsymbol{r}_i) > f(\boldsymbol{r}_j)\,(i > j)$.

On zero-velocity curves, the gradient of a contour curve represents the force as well. When a massless particle is on a zero-velocity curve, the force direction is normal to the curve and toward the allowable region and its magnitude is the same as the absolute value of the gradient (Eq.(2.1)). Figure 2.2 shows the zero-velocity curves in the restricted three-body problem. It describes constraints on the motion of a small particle having a energy level equal to L_3. The shaded area is the allowable region.

2.2.2   Numerical Search for the Spin Period of Surface Shedding

This paper uses the Werner and Scheeres algorithm [189] to obtain the gravitational force from an irregular body. Since their algorithm includes the second order partial derivatives of the potential, it is useful to obtain dynamical equilibrium points.

The method for searching for the dynamical equilibrium points uses a Newton-Raphson method to solve Eq.(2.4). Consider some size scale of this body and assume that a test solution $\boldsymbol{r}_n$ is close to the actual solution $\boldsymbol{r}_*$. Since $\boldsymbol{r}_* = \boldsymbol{r}_n + \Delta\boldsymbol{r}_n$, where $\Delta\boldsymbol{r}_n$ is the relative position of $\boldsymbol{r}_*$ from $\boldsymbol{r}_n$, we rewrite Eq. (2.4) as

$$
\nabla U(\boldsymbol{r}_*) + \omega^2 \boldsymbol{r}_* = \nabla U(\boldsymbol{r}_n + \Delta\boldsymbol{r}_n) + \omega^2(\boldsymbol{r}_n + \Delta\boldsymbol{r}_n) = 0,
\tag{2.5}
$$
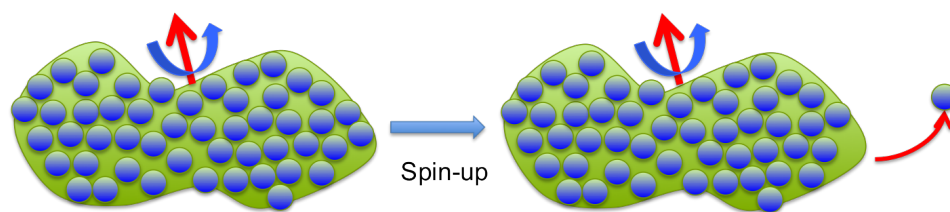
Figure 2.1: Surface shedding due to a static spin-up.
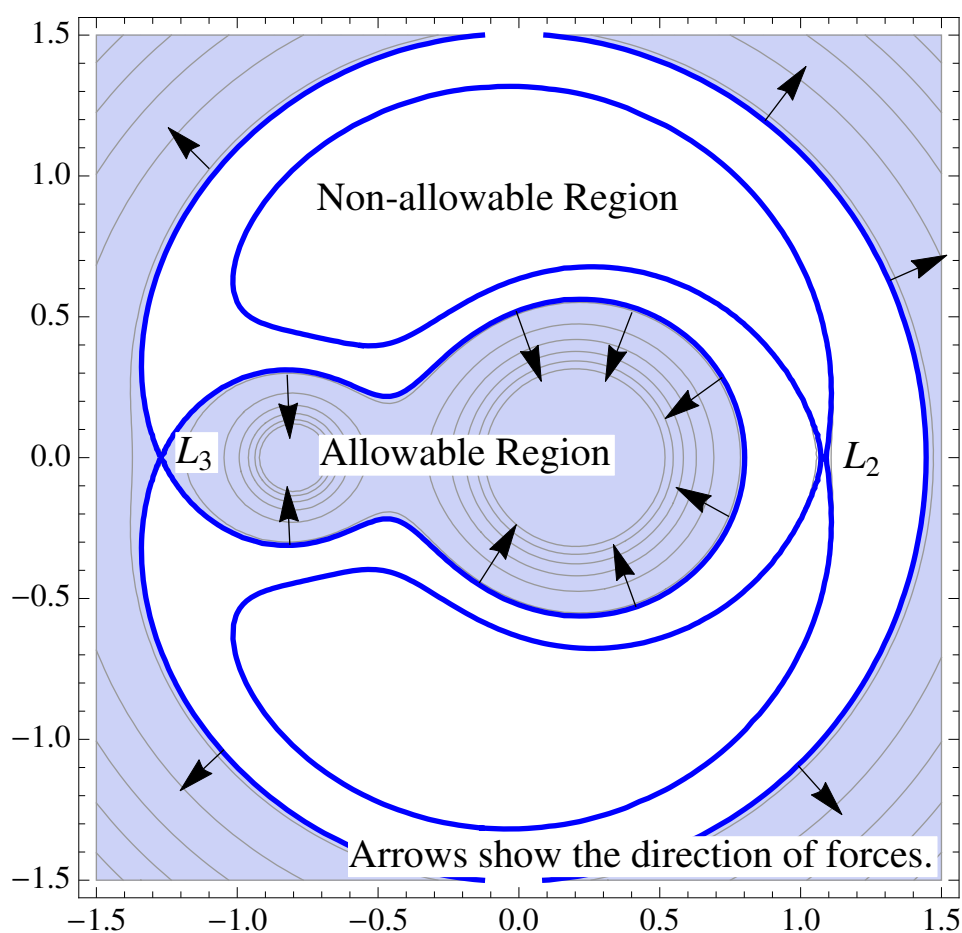
Figure 2.2: Zero-velocity curves in the restricted three body problem. The ratio of a smaller mass to the total mass is 0.2. The blue solid curves indicate the lines with energy levels of L_2 and L_3. These curves intersect these equilibrium points. If a massless particle has the same energy of L_3, it is allowed to move in the shaded area. The arrows show the directions of the forces acting on a massless particle on the curve.

and thus

$$\nabla U(\boldsymbol{r}_n) + \nabla \otimes \nabla U(\boldsymbol{r}_n)\Delta \boldsymbol{r} + \boldsymbol{\omega}^2(\boldsymbol{r}_n + \Delta \boldsymbol{r}_n) = 0, \tag{2.6}$$

where ∇ is the nabla operator, i.e., $\boldsymbol{i}\partial/\partial x + \boldsymbol{j}\partial/\partial y + \boldsymbol{k}\partial/\partial z$ ($\boldsymbol{i}$, $\boldsymbol{j}$, and $\boldsymbol{k}$ are orthogonal unit vectors.), $\otimes$ is the dyad operator, and $\boldsymbol{\omega}$ is an angular velocity matrix defined as

$$\boldsymbol{\omega} = \begin{bmatrix} \omega & 0 & 0 \\ 0 & \omega & 0 \\ 0 & 0 & 0 \end{bmatrix}. \tag{2.7}$$

Finally, the relative position $\Delta \boldsymbol{r}_n$ is given as

$$\Delta \boldsymbol{r}_n = -(\nabla \otimes \nabla U(\boldsymbol{r}_n) + \boldsymbol{\omega}^2)^{-1}(\nabla U(\boldsymbol{r}_n) + \boldsymbol{\omega}^2 \boldsymbol{r}_n). \tag{2.8}$$

We iterate this process ($\Delta \boldsymbol{r}_n$ should be added to update the test solution) until the equilibrium condition is satisfied with an acceptable degree of precision. There are at least four equilibrium points, besides with additional symmetry may have more, but always an even number. To find all the equilibrium points, we set a large number of external points near the surface as the initial conditions.

We calculate the condition of surface shedding by the following iteration scheme. First, we search for all the dynamical equilibrium points at a given condition and check if all these points are outside the body. Second, we calculate zero-velocity curves at the same condition to determine constraints on the motion of a massless particle and to evaluate the force direction. If one of these points touches the surface, then the iteration ends. If none of them attaches to the surface, then we change the spin period of the asteroid and iterate these processes until one of the equilibrium points touches the surface.

Chapter 3

Structural Failure: Limit Analysis

Chapters 3 and 4 discuss methods for determining the condition of structural failure. We characterize structural failure by plastic theory. This chapter gives the definition of structural failure and methods for determining lower and upper bounds for structural failure, while chapter 4 discusses a finite element model for plastic deformation. In this chapter, we first define structural failure and the rheology of materials and second describe techniques for determining lower and upper bound conditions of structural failure.

3.1   Definition

As a body experiences slow changes in its configuration, it may deform somewhere, but may not fail plastically if the stress configuration balances between plasticity and elasticity. If plastic regions are unloaded, the stress configuration comes back to elastic states and residual stresses sustain these regions [24]. Once plastic deformation propagates across the majority of the body, such regions experience catastrophic permanent deformations, leading to a dramatic change of the original shape.

We consider structural failure as a case when plastic deformation propagates over a critical cross section in a body. Again, we only take into account the gravitational and centrifugal forces. In such a case, these forces mainly affect the stress configuration across the minimum moment of inertia axis. Thus, we focus on the condition of structural failure of a slice perpendicular to this principal axis. The scenario of this mode is permanent deformation over the slice and may

eventually lead to a breakup into two smaller components (Fig. 3.1). Note that we will use the term "structural failure of a total volume" with the same meaning as the term "global failure" often used by Holsapple.

3.2   Rheology of Materials: Mohr-Coulomb Yield Criterion

The yield condition defines the limit of elastic behavior. Here, the yield condition of a material of an asteroid is considered to depend on hydrostatic pressure and shear. For the limit analysis technique, we use the Mohr-Coulomb (MC) yield criterion, which is written as

$$g(\sigma_1, \sigma_3, \phi) = (\sigma_1 - \sigma_3)\sec\phi + (\sigma_1 + \sigma_3)\tan\phi \leq 2Y, \tag{3.1}$$

where ϕ is a friction angle and Y is cohesive strength [28]. σ_i $(i = 1, 2, 3)$ is the principal stress component and satisfies $\sigma_1 > \sigma_2 > \sigma_3$. This condition indicates a slope attaching to the Mohr circle centered at $(\sigma_1 + \sigma_3)/2$ with a radius of $(\sigma_1 - \sigma_3)/2$ in the hydrostatic pressure-shear stress space (Fig.3.2). If we assume zero-cohesion, then $Y = 0$ and the slope intersects the origin. The angle between the slope and the σ axis is identical to friction angle ϕ. The inequality shown in Eq.(3.1) describes that if the stress state is within that region, it is elastic.

In a principal-stress space, the MC envelope becomes a hexagonal cone opening to the negative side in the hydrostatic pressure direction. This cone is discontinuous at the tension and the compression meridians. Since this paper considers real shapes, stress conditions at these meridians may not appear in general.

3.3   Computation of Body Forces

This study considers that only the gravitational and centrifugal forces act on the internal structure of a body. Since the shape is irregular, it is necessary to discretize the body to calculate the body forces. We make a high resolution mesh so that its elements are small enough to model body force calculation. In this case, since we can use a classical two-body problem for each interaction,

the gravitational acceleration of element s is described as

$$\boldsymbol{b}_{sg} = -G\rho \sum_{t \neq s} \frac{V_t}{r_{st}^3}(\boldsymbol{r}_s - \boldsymbol{r}_t),$$ (3.2)

where G is the gravitational constant, V is the volume of an element, and element t does not overlap s. $\boldsymbol{r}$ is a position vector from the origin to an element, and r is the Euclidean norm of $\boldsymbol{r}$. Here, the density ρ is assumed to be constant everywhere in the body. The centrifugal acceleration is simply described as

$$\boldsymbol{b}_{sc} = -\boldsymbol{\Omega} \times \boldsymbol{\Omega} \times \boldsymbol{r}_s = \Omega^2 \begin{bmatrix} x_{s1} \\ x_{s2} \\ 0 \end{bmatrix}.$$ (3.3)

where $\boldsymbol{\Omega}$ is the spin vector $\Omega[0, 0, 1]^T$. With index notations, the body force is now given as

$$b_i = b_{sgi} + b_{sci}.$$ (3.4)

3.4 Theorems for Limit Analysis

Limit analysis provides a technique for determining lower and upper bounds for structural failure. For a uniformly rotating ellipsoid, Holsapple (e.g., [70, 65]) constructed lower and upper bounds that are the same. We assume that materials in a body follow elasticity-perfect plasticity and its plastic deformation is small. The condition of elasticity-perfect plasticity idealizes the behaviors of materials. The critical features of this assumption include zero-hardening and zero-softening. The assumption of small deformation allows for the use of the virtual work principle:

$$\oint_A T_i u_i^* + \int_V F_i u_i^* dV = \int_V \sigma_{ij} \epsilon_{ij}^* dV,$$ (3.5)

where A means area, V is the volume, T_i is the surface traction force, F_i is the body force, σ_{ij} is the stress component, ϵ_{ij} is the strain component, and u_i is the displacement. A dot over a letter indicates the rate of the quantity. Quantities with $*$ are associated with the virtual work. The following sections discuss the lower and upper bound theorems, based on the earlier studies (e.g., [28], [24], [70], and [65]). The present study will use the upper bound theorem to find an upper bound for structural failure.

3.4.1 Preparatory Theorem

Theorem 1. *If a load reaches the limit condition, then the deformation proceeds under a constant load, all stresses remain constant, and only plastic (not elastic) increments of strain occur [28].*

Proof. Consider the rate form of the virtual work equation:

$$\oint_{A_T} \dot{T}_i^c \dot{u}_i^c dA_T + \oint_{A_u} \dot{T}_i^c \dot{u}_i^c dA_u + \int_V \dot{F}_i^c \dot{u}_i^c dV = \int_V \dot{\sigma}_{ij}^c \dot{\epsilon}_{ij}^c dV, \tag{3.6}$$

where A_T and A_u are the boundary conditions of T_i and u_i, respectively. We use superscript c to emphasize that this equation satisfies an actual collapse state. $\dot{u}_i^c$ should be zero on A_u. At the limit load, since $\dot{F}_i^c = 0$ in V, $\dot{T}_i^c = 0$ on A_T, and $\dot{u}_i^c = 0$ on A_u, the left-hand side becomes zero:

$$\int_V \dot{\sigma}_{ij}^c \dot{\epsilon}_{ij}^c dV = \int_V \dot{\sigma}_{ij}^c (\dot{\epsilon}_{ij}^{ec} + \dot{\epsilon}_{ij}^{pc}) dV = 0. \tag{3.7}$$

We used the fact that the total strain rates $\dot{\epsilon}_{ij}^c$ consist of elastic and plastic parts. The associated flow rule yields $\dot{\sigma}_{ij}^c \dot{\epsilon}^p c_{ij} = 0$. Finally, we obtain

$$\int_V \dot{\sigma}_{ij}^c \dot{\epsilon}_{ij}^{ec} dV = 0. \tag{3.8}$$

However, from Drucker's stability postulate, for elastic materials, the work done by any systems on elastic deformation is always positive definite. We obtain $\dot{\sigma}_{ij}^c = 0$, and thus $\epsilon_{ij}^{ec} = 0$. □

3.4.2 The Lower-Bound Theorem

Theorem 2. *If an equilibrium distribution of stress σ_{ij}^E can be found which balances the body force F_i in V and the applied loads T_i on the stress boundary A_T and is everywhere below yield, $f(\sigma_{ij}^E) < 0$, then the body at the loads T_i, F_i will not collapse [28].*

Proof. Assuming that the body at the loads will collapse, we give the contradiction of this assumption. If the body is at this load, there exists a collapse condition represented by the actual stress σ_{ij}^c, the strain rate $\dot{\epsilon}_{ij}^c$, and the displacement rate $\dot{u}_i^c$. The displacement rate is zero on A_u, i.e.,

$\dot{u}_{ij}^c = 0$. From the statement, two equilibrium states may exit, i.e.,

$$\oint_A T_i \dot{u}_i^c + \int_V F_i^c \dot{u}_i^c dV \;=\; \int_V \sigma_{ij}^c \dot{\epsilon}_{ij}^c dV, \tag{3.9}$$

$$\oint_A T_i \dot{u}_i^c + \int_V F_i^c \dot{u}_i^c dV \;=\; \int_V \sigma_{ij}^E \dot{\epsilon}_{ij}^c dV, \tag{3.10}$$

These equations yield

$$\int_V (\sigma_{ij}^c - \sigma_{ij}^E)\epsilon_{ij}^c dV = 0. \tag{3.11}$$

At the limit load, all deformation is plastic (see Theorem 1). Therefore,

$$\int_V (\sigma_{ij}^c - \sigma_{ij}^E)\epsilon_{ij}^{pc} dV = 0. \tag{3.12}$$

However, for perfect plasticity, because of convexity and normality, $(\sigma_{ij}^c - \sigma_{ij}^E)\epsilon_{ij}^{pc} > 0$, which contradicts the assumption. $\qquad\square$

3.4.3   The Upper-Bound Theorem

Theorem 3. *Assume that the zero-displacement condition $\dot{u}_i^{p*} = 0$ on A_u. Then, the loads T_i and F_i determined by the virtual work equation*

$$\oint_{A_T} T_i \dot{u}_i^{p*} + \int_V F_i \dot{u}_i^{p*} dV = \int_V \sigma_{ij}^{p*} \dot{\epsilon}_{ij}^{p*} dV. \tag{3.13}$$

will be either higher than or equal to the actual limit load. σ_{ij}^{p*} is a stress state that yields $\dot{\epsilon}_{ij}^{p*}$. The left-hand side is called the work by the external forces, while the right-hand side is called the rate of internal dissipation [28]:

$$\int_V \dot{D}(\epsilon_{ij}^{p*})dV = \int_V \sigma_{ij}^{p*} \dot{\epsilon}_{ij}^{p*} dV. \tag{3.14}$$

Proof. Assume that the condition is neither higher than or equal to the actual limit load. From the lower-bound theorem, in this condition, there exits an equilibrium distribution of elastic stresses σ_{ij}^E that satisfy $f(\sigma_{ij}^E) < 0$ everywhere:

$$\oint_{A_T} T_i \dot{u}_i^{p*} + \int_V F_i \dot{u}_i^{p*} dV = \int_V \sigma_{ij}^E \dot{\epsilon}_{ij}^{p*} dV. \tag{3.15}$$

Since Eq. (3.13),

$$\int_V (\sigma_{ij}^{p*} - \sigma_{ij}^E) \dot{\epsilon}_{ij}^{p*} dV = 0. \tag{3.16}$$

However, since $(\sigma_{ij}^{p*} - \sigma_{ij}^E) \dot{\epsilon}_{ij}^{p*} > 0$, the statement leads to a contradiction. $\qquad\square$

3.5 Lower Bound for Structural Failure of a Body

We use the lower bound theorem (Sec. 3.4.2) to obtain a lower bound for structural failure. The theorem indicates that if an elastic solution is always below the yield condition everywhere, then the stress configuration is below the lower bound. This study develops a finite element model of (216) Kleopatra to calculate its elastic stress solution and check whether or not the stresses at all the nodes are below the yield condition.

3.6 Upper Bound for Structural Failure of a Partial Volume

Based on Sec. 3.4.3, the present study considers an upper bound condition for structural failure of a partial volume in a body to approximate the condition of structural failure. This technique enables us to compare sensitive volumes to structural failure and to find a possible mode of this failure. We assume that the shape of a body is symmetric about the intermediate and maximum moment of inertia axes. In such a case, the minimum moment of inertia axis is the most sensitive to structural failure because of the symmetry of the body forces. Thus, we choose a slice perpendicular to the minimum moment of inertia axis as a partial volume. Based on the theorem by Holsapple [65], this section shows that for such a slice, there is a condition at which an upper bound for its structural failure is identical to the yield condition of the averaged stress over this volume.

3.6.1 Calculation of The Partial Volume Stress

3.6.1.1 General Expression

Consider an irregularly shaped body spinning about the maximum moment of inertia axis in free space (Fig. 3.3). The maximum, intermediate, and minimum moment of inertia axes are defined as the x_1, x_2, and x_3 axes, respectively. These axes are identical to the x, y, and z axes defined in the previous chapters, respectively.

Then, cut this body at two different locations so that the given cross sections S_A and S_B are always perpendicular to the x_1 axis (Fig. 3.3). This operation creates three partial components, and we take the middle one, which is shaded in the figure (later, simply called the "slice"). The partial volume stress is defined as the averaged stress over the slice:

$$\bar{\sigma}_{ij} \;=\; \frac{1}{V}\int_V \rho x_j b_i dV + \frac{1}{V}\oint_S x_j t_i dS, \tag{3.17}$$

where V is the volume of the slice, S is the whole area of the cross sections, i.e., $S = S_A + S_B$, and b_i is the body force. A traction $t_i = l\sigma_{i1}$, where l is the direction cosine normal to the cross sections perpendicular to the x_1 axis (the outward direction is positive), is not affected by other direction cosines. ρ is the bulk density, which is currently assumed to be constant over the whole volume. σ_{ij}, where i and j are indices varying from 1 to 3, indicates the stress component of a small element.

Consider the off-diagonal components of the partial volume stress. In a static condition, since a planetary body experiences neither motion nor deformation in the rotating frame, the torques on a given slice along the x_k axis ($k = 1, 2, 3$)

$$\tau_k \;=\; \int_V \rho(x_j b_i + x_i b_j)dV + \oint_S (x_j t_i + x_i t_j)dS, \tag{3.18}$$

where t_j is a traction on the cross sections and the indices satisfy $i \neq j \neq k$, are always zero. However, the right hand side is equivalent to $\bar{\sigma}_{ij} + \bar{\sigma}_{ji}$. Then, in the static case, $\bar{\sigma}_{ij} = \bar{\sigma}_{ji}$, so $\bar{\sigma}_{ij} = \bar{\sigma}_{ji} = 0$. Therefore, all the off-diagonal components are always zero in general cases. This indicates that the partial volume stresses of any arbitrary slices correspond to the principal stresses.

On the other hand, the diagonal components are nonzero. For $\bar{\sigma}_{11}$, since $x_j = x_1$ in Eq. (3.17), it comes out of the surface integral:

$$\bar{\sigma}_{11} \;=\; \frac{1}{V}\int_V \rho x_1 b_1 dV + \frac{x_{1A}}{V}\oint_{S_A} t_1 dS + \frac{x_{1B}}{V}\oint_{S_B} t_1 dS, \tag{3.19}$$

where x_{1A} and x_{1B} are the x_1 components of S_A and S_B, respectively. Since the surface integrals of the second and third terms on the right-hand side in Eq. (3.19) correspond to the forces acting on the cross sections, this component can be determined without solving the equilibrium equation. For $\bar{\sigma}_{kk}$ $(k = 2, 3)$, the surface integral term cannot easily be calculated because it includes the integrand $x_k t_k$. However, if the slice is symmetric (the detailed definition is given in the next section), these components can also be obtained.

3.6.1.2   Symmetry Assumption

Hereafter, we define the x_1, x_2, and x_3 axes as the minimum, intermediate, and maximum moment of inertia axes, respectively. Also, it is assumed that a body is uniformly spinning about the x_3 axis. To determine $\bar{\sigma}_{22}$ and $\bar{\sigma}_{33}$, we introduce the symmetric assumption that a slice defined by S_A and S_B is symmetric about the x_2 and x_3 axes (Fig. 3.3).

For cross section $S_A(x_1, x_2)$, the symmetric assumption is defined as follows; that is $x_3 = S_{A+}(x_1, x_2) = S_{A+}(x_1, -x_2) = -S_{A-}(x_1, x_2) = -S_{A-}(x_1, -x_2)$, where $S_{A+}(x_1, x_2)$ for $x_3 \geq 0$ and $S_{A-}(x_1, x_2)$ for $x_3 < 0$. The symmetry assumption is also applied to cross section $S_B(x_1, x_2)$. These cross sections are not necessarily identical; in other words, the shape of the cross section can vary along the x_1 axis.

3.6.1.3   Body Forces and Stress States

We assume that the body is affected by the gravitational and centrifugal forces. The gravity force at $\boldsymbol{r}_c$ is written as

$$\boldsymbol{b}_g \;=\; -\int_V \frac{G\rho(\boldsymbol{r}_c - \boldsymbol{r})dV}{\|\boldsymbol{r}_c - \boldsymbol{r}\|^3}, \tag{3.20}$$

$$=\; [b_{g1} \; b_{g2} \; b_{g3}]^T, \tag{3.21}$$

where $\boldsymbol{r}$ is the position vector of the internal element and G is the gravitational constant. The centrifugal force at $\boldsymbol{r}_c$ is described as

$$
\begin{aligned}
\boldsymbol{b}_c &= \boldsymbol{\omega} \times \boldsymbol{\omega} \times \boldsymbol{r}_c, \\
&= [b_{c1} \ b_{c2} \ b_{c3}]^T,
\end{aligned}
\tag{3.22}
$$

where $\boldsymbol{\omega} = [0 \ 0 \ \omega]^T$ is the angular velocity vector. Thus, the body force is described as $\boldsymbol{b} = \boldsymbol{b}_g + \boldsymbol{b}_c = [b_1 \ b_2 \ b_3]^T$. Because of the symmetry assumption, the body forces at $\boldsymbol{r}'_c = [x_{1c} - x_{2c} \ x_{3c}]^T$, $\boldsymbol{r}''_c = [x_{1c} \ x_{2c} - x_{3c}]^T$, and $\boldsymbol{r}'''_c = [x_{1c} - x_{2c} - x_{3c}]^T$ can also be described as

$$
\begin{aligned}
b_1(\boldsymbol{r}_c) &= b_1(\boldsymbol{r}'_c) = b_1(\boldsymbol{r}''_c) = b_1(\boldsymbol{r}''_c), \\
b_2(\boldsymbol{r}_c) &= -b_2(\boldsymbol{r}'_c) = b_2(\boldsymbol{r}''_c) = -b_2(\boldsymbol{r}'''_c), \\
b_3(\boldsymbol{r}_c) &= b_3(\boldsymbol{r}'_c) = -b_3(\boldsymbol{r}''_c) = -b_3(\boldsymbol{r}'''_c).
\end{aligned}
\tag{3.23}
$$

The symmetry assumption allows for giving the symmetry of the stress solution. Given the equilibrium equation, which is written as

$$
\frac{\partial \sigma_{ij}}{\partial x_j} + \rho b_i = 0,
\tag{3.24}
$$

we obtained stress states at $\boldsymbol{r}_c$, $\boldsymbol{r}'_c$, $\boldsymbol{r}''_c$, and $\boldsymbol{r}'''_c$. The off-diagonal components are

$$
\begin{aligned}
\sigma_{12}(\boldsymbol{r}_c) &= -\sigma_{12}(\boldsymbol{r}'_c) = \sigma_{12}(\boldsymbol{r}''_c) = -\sigma_{12}(\boldsymbol{r}'''_c), \\
\sigma_{13}(\boldsymbol{r}_c) &= \sigma_{13}(\boldsymbol{r}'_c) = -\sigma_{13}(\boldsymbol{r}''_c) = -\sigma_{13}(\boldsymbol{r}'''_c), \\
\sigma_{23}(\boldsymbol{r}_c) &= -\sigma_{23}(\boldsymbol{r}'_c) = -\sigma_{23}(\boldsymbol{r}''_c) = \sigma_{23}(\boldsymbol{r}'''_c),
\end{aligned}
\tag{3.25}
$$

and the diagonal components are

$$
\sigma_{ii}(\boldsymbol{r}_c) = \sigma_{ii}(\boldsymbol{r}'_c) = \sigma_{ii}(\boldsymbol{r}''_c) = \sigma_{ii}(\boldsymbol{r}'''_c).
\tag{3.26}
$$

3.6.1.4   Calculation of $\bar{\sigma}_{22}$ and $\bar{\sigma}_{33}$

Equation (3.25) yields

$$
\begin{aligned}
\oint_S t_k x_k dS &= \oint_{S_A} \sigma_{k1} x_k dS - \oint_{S_B} \sigma_{k1} x_k dS, \\
&= \oint_{S_{A+}+S_{A-}} \sigma_{k1} x_k dS - \oint_{S_{B+}+S_{B-}} \sigma_{k1} x_k dS, \\
&= \oint_{S_{A+}} \sigma_{k1}(x_k - x_k)dS - \oint_{S_{B+}} \sigma_{k1}(x_k - x_k)dS, \\
&= 0.
\end{aligned}
\tag{3.27}
$$

The operation from the second row to the third row used the relations of $\sigma_{12}(\boldsymbol{r}_c) = -\sigma_{12}(\boldsymbol{r}'_c)$ and $\sigma_{13}(\boldsymbol{r}_c) = -\sigma_{13}(\boldsymbol{r}''_c)$. This indicates that the surface integrals over S_A and S_B become zero, respectively. Therefore,

$$
\bar{\sigma}_{kk} = \frac{1}{V} \int_V \rho x_k b_k dV.
\tag{3.28}
$$

where $k = 2, 3$.

3.6.2   Error Analysis

Since we apply the Mohr-Coulomb yield criterion to determine a limit condition of a partial volume, neglecting the surface integral of $x_3 t_3$ causes an error of $\bar{\sigma}_{33}$.

Consider the surface integral of $x_3 t_3$ over S_A. Since

$$
\oint_{S_A} x_3 t_3 dS = \int_{x_{2-}}^{x_{2+}} [x_{3+} f(x_{3+}) - x_{3-} f(x_{3-})]dx_2 - \oint_{S_A} t_3 dS,
\tag{3.29}
$$

where x_{3-} and x_{3+} are the minimum and maximum distance from $x_3 = 0$ at given x_2 on S_A, respectively, and f is an indefinite integral given as

$$
f(x_3) = \int t_3 dx_3,
\tag{3.30}
$$

the following inequality is obtained:

$$
\begin{aligned}
\oint_{S_A} x_3 t_3 dS &< \int_{x_{2-}}^{x_{2+}} [x_{3max} f(x_{3+}) - (-x_{3max}) f(x_{3-})]dx_2 - \oint_{S_A} t_3 dS, \\
&= (x_{3max} - 1) \oint_{S_A} t_3 dS,
\end{aligned}
\tag{3.31}
$$

where x_{3max} is the maximum position in the x_3 direction in the whole volume. The inequality of the first row appears on the assumption that $x_{3max} > \|x_{3min}\| > 0$. If $\|x_{3min}\| > x_{3max}$, where x_{3min} is the minimum position in the x_3 direction in the whole volume and is always negative, x_{3max} is replaced with $\|x_{3min}\|$. Since this formulation can also be obtained for the other cross section S_B, the absolute value of the surface integral for the total cross section $S = S_A + S_B$ is given as

$$\| \oint_S x_3 t_3 dS \| < x_{3max} \| \oint_S t_3 dS \|. \tag{3.32}$$

For $\bar{\sigma}_{33}$, we only calculate the body integral term, which can be obtained accurately. Based on Eq. (3.32), the error of this stress component is defined as

$$\epsilon = \frac{x_{3max} \| \oint_S t_3 dS \|}{\| \int_V x_3 b_3 dV \|}. \tag{3.33}$$

Since σ_{33} does not depend on the centrifugal force, ϵ is constant.

3.6.3 Upper Bound Theorem

The previous section showed that under the symmetry assumption, the volume integrals over a partial volume, i.e., the slice, and the surface integrals over its cross sections can yield the partial volume stresses. With this fact, the upper bound theorem determines the condition at which structural failure must occur. Keeping the symmetry assumption, this section constructs such a condition for the slices defined above. We assume that (i) mechanical behavior of materials can be modeled by elasticity-perfect plasticity and (ii) plastic deformation is negligibly small and follows the associated flow rule. We use the Mohr-Coulomb yield criterion (Eq. 3.1). Note that from Sec. 3.6.1.1, for the partial volume stresses, $\sigma_1 = \bar{\sigma}_{11}$, $\sigma_2 = \bar{\sigma}_{22}$, and $\sigma_3 = \bar{\sigma}_{33}$. The following discussion focuses on the principal stress components and keeps these notations without confusion.

We introduce a kinematically admissible velocity field such that the rate of internal dissipation is equal to the rate of the external work (the upper bound theorem). A kinematically admissible velocity field is characterized as a compatibility condition that the stress state satisfies

the equilibrium equation anywhere, and the rate of plastic deformation is zero at any velocity boundary conditions, i.e., $\dot{\boldsymbol{u}}^p(\boldsymbol{x}) = 0$, for $\forall \boldsymbol{x} \in A_u$, where A_u is the boundary condition space of plastic deformation. If a suitable kinematically admissible velocity field is found, the condition obtained is identical to an upper bound [28].

In the present study, since elastic and plastic parts can coexist in the whole volume at some critical period, A_u is not an empty space there. To avoid the complexity of A_u, we consider that the assumed plastic region is slightly thicker than the slice so that in the slice A_u is an empty space (Fig. 3.4). This idealization process can also remove any discontinuities between elastic and plastic regions and allow for the use of the Holsapple [65] result.

The symmetry assumption guarantees the symmetry of the body force and the stress state (Sec. 3.6.1.3), implying that a static spin-up does not break the symmetry of the stress state and any plastic deformations are also symmetric. Also, the gravitational and centrifugal force are mainly affecting the x_1 direction and could cause deformation along this axis. Since we use the Mohr-Coulomb yield criterion, the associated flow rule indicates that the rate of the plastic strain, $\dot{\epsilon}_i^p$, is constant:

$$
\begin{aligned}
\dot{\epsilon}_i^p &= \dot{\lambda}\frac{\partial g(\sigma_j)}{\partial \sigma_i}, \\
&= [m\dot{\lambda}\ 0\ -\dot{\lambda}]^T,
\end{aligned}
\tag{3.34}
$$

where $\dot{\lambda}$ is the rate of a scale factor and $m = (1 + \sin\theta)/(1 - \sin\theta)$. Thus, with the symmetric assumption, we choose a kinematically admissible velocity field as

$$
\dot{u}_1^p = (x_1 - x_{10})m\dot{\lambda}, \quad \dot{u}_2^p = 0, \quad \dot{u}_3^p = -x_3\dot{\lambda},
\tag{3.35}
$$

where x_{10} is a constant value representing the location of the slice. The choice of this velocity field is based on the Holsapple [65] result.

Consider the rate of the internal energy dissipation, $\dot{D}$, and the rate of the external work,

$\dot{W}$. With the use of Eq. (3.17), $\dot{D}$ is written as

$$
\begin{aligned}
\dot{D} &= V \sum_{i=1}^{3} \bar{\sigma}_i \dot{\epsilon}_i^p, \\
&= \sum_{i=1}^{3} \left[\dot{\epsilon}_i^p \int_V \rho x_i b_i dV + \dot{\epsilon}_i^p \oint_S x_i t_i dS \right].
\end{aligned}
\tag{3.36}
$$

On the other hand, Eq. (3.35) yields $\dot{W}$ as

$$
\begin{aligned}
\dot{W} &= \sum_{i=1}^{3} \left[\int_V \rho \dot{u}_i^p b_i dV + \oint_S u_i^p t_i dS \right], \\
&= \sum_{i=1}^{3} \left[\dot{\epsilon}_i^p \int_V \rho x_i b_i dV + \dot{\epsilon}_i^p \oint_S x_i t_i dS \right].
\end{aligned}
\tag{3.37}
$$

The process from the first row to the second row on the right-hand side eliminates the terms including x_{10} because of the symmetry assumption. Therefore, $\dot{D} = \dot{W}$. This shows that the yield condition of the partial volume stress is identical to an upper bound for structural failure. We emphasize that choices of the slice and the deformation mode may not correspond to actual failure states; therefore, it is necessary to compare the upper bounds of several slices that may experience structural failure.
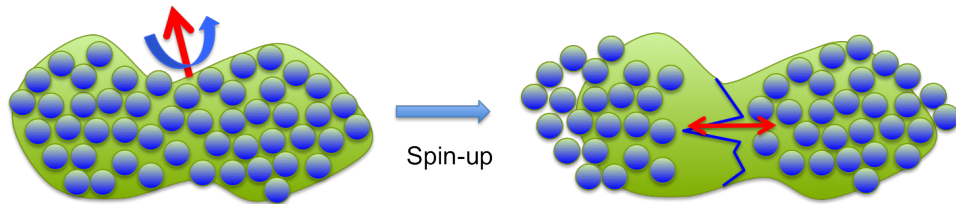
Figure 3.1: Structural failure mode. When the spin of an asteroid reaches the condition of structural failure, a plastic region spreads over the cross section in the middle. If the asteroid spins up further, it eventually breaks up into multiple components.
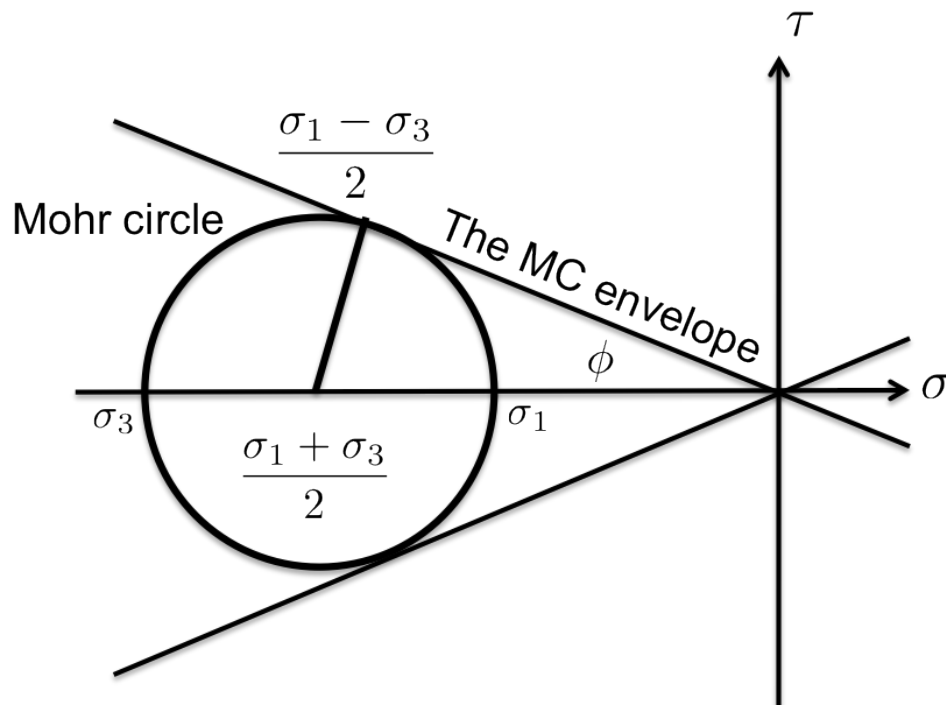
Figure 3.2: Mohr-Coloumb yield envelope and Mohr circle. The slope touching a Mohr circle is the Mohr-Coulomb yield envelope. The inclination depends on a material's properties. If a stress state is within the Mohr-Coulomb envelope, it is elastic. If a stress state is on the envelope, it is plastic. σ is the normal stress and τ is the stress stress.
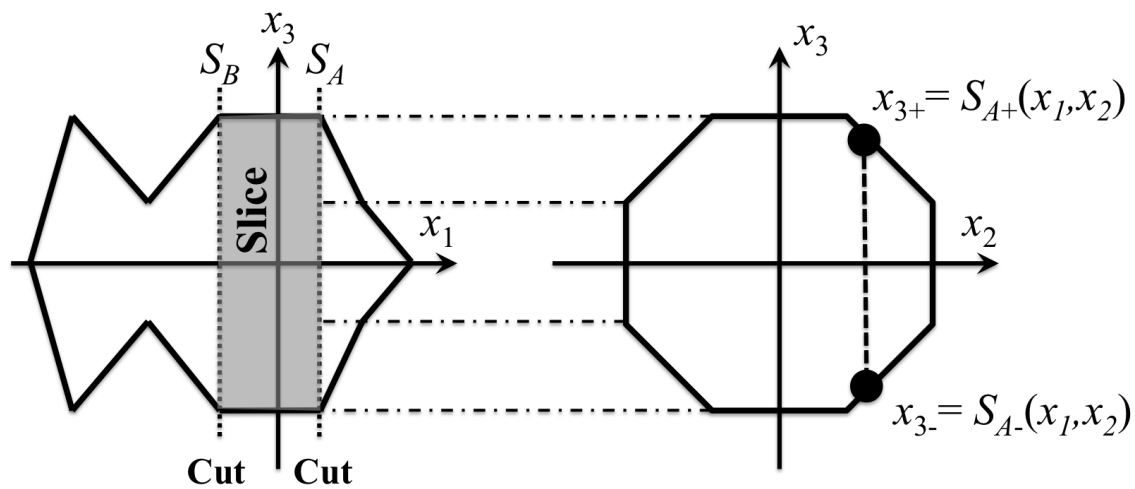
Figure 3.3: Partial volume of a planetary body, here simply called the "slice", and its symmetric assumption. Consider an arbitrary coordinate frame having the x_1, x_2, and x_3 axes. The slice is a volume given by two arbitrary cuts through cross sections perpendicular to the x_1 axis (the shaded area). The cross sections on the positive and negative sides are denoted as S_A and S_B, respectively. The symmetry assumption defines the symmetry of any cross sections perpendicular to the x_1 axis. For cross section S_A, for example, by defining the functions $x_{3+} = S_{A+}(x_1, x_2)$ for $x_3 \geq 0$ and $x_{3-} = S_{A-}(x_1, x_2)$ for $x_3 < 0$, $S_{A+}(x_1, x_2) = S_{A+}(x_1, -x_2) = -S_{A-}(x_1, x_2) = -S_{A-}(x_1, -x_2)$. These cross sections are not necessarily identical, e.g., $S_A \neq S_B$.
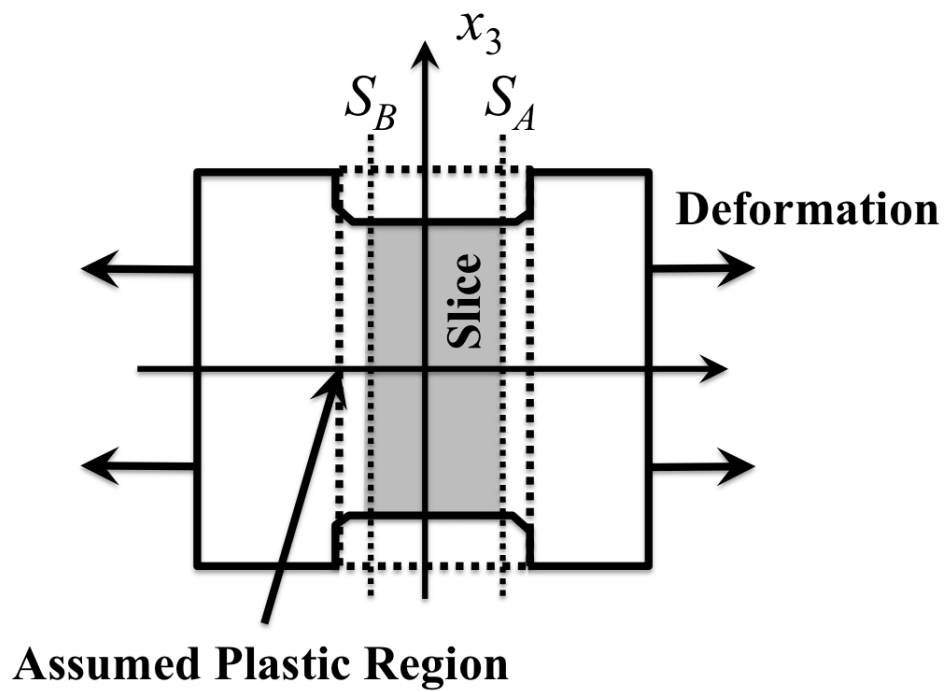
Figure 3.4: Possible plastic deformation mode of a symmetric body. We consider that the assumed plastic region is wider than the slice. By doing so, we avoid any discontinuities and the velocity boundary condition A_u. For this case, there may be a linear velocity field in the location.

Chapter 4

Structural Failure: Finite Element Analysis

This chapter discusses a finite element analysis for structural failure. Since the model includes plastic deformation, it can determine a more precise condition of structural failure of (216) Kleopatra and its failure mode. First, we summarize finite element modeling. Second, the rheology of materials used in the present finite element model is introduced. Third, we define the boundary conditions. Then, we introduce the load steps and parameter representations given in this study. The following sections introduce our modeling by focusing on (216) Kleopatra.

4.1 Finite Element Modeling

The present finite model includes plastic deformation. The behavior of materials is supposed to be elastic-perfectly plastic and to follow a non-associated flow rule. Also, plastic deformation is assumed to be small. The assumption of elasticity-perfect plasticity is an idealized condition that materials do not have hardening and softening. For plastic solutions, load paths change the final plastic solutions.

This study uses commercial finite element software ANSYS (Academic research 14.0) to calculate finite element solutions. The theories of computational techniques on ANSYS are given in standard textbooks and ANSYS tutorials (http://www.ansys.com/). For static cases, ANSYS solves the following equations:

$$\boldsymbol{K}\boldsymbol{u} = \boldsymbol{F}, \tag{4.1}$$

where $\boldsymbol{K}$ is a stiffness matrix, $\boldsymbol{u}$ is a nodal displacement vector, and $\boldsymbol{F}$ is a force vector.

4.2   Rheology of Materials: Drucker-Prager Yield Criterion

To model the rheology of materials in the finite element model, we use the Drucker-Prager (DP) yield criterion, which is described as

$$f(I_1, J_2) = \alpha I_1 + \sqrt{J_2} - k, \tag{4.2}$$

where

$$I_1 = \sigma_1 + \sigma_2 + \sigma_3, \tag{4.3}$$

$$J_2 = \frac{1}{6}[(\sigma_1 - \sigma_2)^2 + (\sigma_2 - \sigma_3)^2 + (\sigma_3 - \sigma_1)^2]. \tag{4.4}$$

α and k change in cases. This yield criterion is smooth. Because of α and k, the size of the envelope cannot be determined uniquely. Usually, α and k are chosen such that the DP envelope touches some points on the MC envelope. If the DP envelope touches at the compression meridian of the MC envelope,

$$\alpha = \frac{2\sin\phi}{\sqrt{3}(3 - \sin\phi)}, \tag{4.5}$$

$$k = \frac{6c\cos\phi}{\sqrt{3}(3 - \sin\phi)}. \tag{4.6}$$

If at the tension meridian, α and k are written as

$$\alpha = \frac{2\sin\phi}{\sqrt{3}(3 + \sin\phi)}, \tag{4.7}$$

$$k = \frac{6c\cos\phi}{\sqrt{3}(3 + \sin\phi)}. \tag{4.8}$$

We will use the DP yield criterion to compute plastic solutions by finite element analysis on ANSYS. In the present finite element analysis, we newly define α and k to consider the failure condition based on pure pressure and pure shear. Take $\sigma_2 = (\sigma_1 + \sigma_3)/2$ to charcterize pure pressure and pure shear [67]. Then, α and k are given as

$$\alpha = \frac{\sin\phi}{3}, \tag{4.9}$$

$$k = \frac{c\sin\phi}{1 - \sin\phi}. \tag{4.10}$$

We use the dilatancy angle κ to describe non-associated flow. A typical soil has a change of its volume below the ideal yield point. This parameter is an effective angle that describes the ratio of the actual volume change to the ideal volume change due to associated flow [28]. The plastic strain rate $\dot{\epsilon}_{ij}^{p}$, where i and j are indices, is defined as the rate of an arbitrary coefficient λ times the partial derivative of a stress function f with respect to the stress tensor σ_{ij}, which is given as

$$\dot{\epsilon}_{ij}^{p} = \dot{\lambda}\frac{\partial f(\sigma_{ij}, \kappa)}{\partial \sigma_{ij}}, \tag{4.11}$$

In this study, f is characterized by the Drucker-Prager yield criterion and the dilatancy angle.

4.3   Boundary Conditions

In the present finite element model, we constrain six degrees of freedom of the node displacements. In nature, when seen globally, planetary bodies are spinning in free space, so there are no constraints on their deformation and motion. However, discrepancies of numerical settings violate force balance, which may provoke rotational and translational motions. Therefore, it is necessary to constrain the displacements of the nodes so that the solutions can converge appropriately. A typical method for avoiding this problem is to consider a part of a symmetric body and to insert proper boundary conditions. However, since (216) Kleopatra is not globally symmetric, its whole body has to be taken into account in the simulation. Here, to fix such motions, we constrain six degrees of freedom: three degrees of freedom being for its rotational motion and the other three degrees of freedom being for its translational motion. Specifically, the displacements in all the directions of the node at the origin are fixed to constrain the translational motion; on the other hand, the displacements in the y and z directions of the surface node along the x axis (the positive side) and the displacement in the z direction of the surface node along the y axis (the positive side) are fixed to remove the rotational motion.

The zero-traction condition over the surface is also considered. Since this condition comes from the free-spin condition mentioned above, it should be satisfied over the surface. In our finite element model, since the loads are defined at each node, including the surface nodes, the stresses

on the surface are not exactly zero. However, we confirmed that the stresses on the surface is about 10 % of the stress at the center of the knob[1] . Based on a stress solution by Holsapple [70], the scale of the stress distribution can be described as

$$\frac{\sigma_r}{\sigma_0} \sim 1 - \frac{r^2}{a^2}, \tag{4.12}$$

where σ_0 is the stress at the center of the knob, σ_r is the stress at radius r from the center, and a is the apparent radius of the knob. Since $\sigma_r/\sigma_0 \sim 0.1$ and the radius of the knob, a, is on the order of 50 km, $r \sim 47.5$ km. Therefore, the surface stress computed in the present model may be the actual stress appearing 2.5 km beneath the surface, which is the same order of the element size used here.

4.4   Load Steps

A plastic solution depends on a loading path that represents evolutional history; however, the history profile is usually unknown. To model the evolutional history of (216) Kleopatra, it is assumed that the body experiences zero body forces initially and then the load is incremented linearly. This profile assumes that the current configuration of (216) Kleopatra results from an accretion due to a catastrophic disruption that gives the gravitational and centrifugal forces simultaneously. The time scale of the accretion process due to a catastrophic impact is probably less than several days [106], negligibly shorter than the life time of asteroids. The collisional probability of a main belt asteroid with larger than 50 km in size is 2.86×10^{-18} km^{-2} yr^{-1}, much lower than that of a near-earth asteroid, 15.34×10^{-18} km^{-2} yr^{-1} [10, 11].

The YORP effect, thermal reemission causing torque on an irregularly shaped body [134], could not change the spin state over the age of this body. Since this effect is highly dependent on the size, (216) Kleopatra, having a few hundred kilometers in diameter, may not spin up sufficiently. In fact, to double the spin period of (216) Kleopatra, it takes more than 1000 Gyr, much longer than the age of the solar system, $\sim$4.6 Gyr [181].

---

[1] As seen in Fig. 1.4, the shape looks like two chunks connecting each other. Hereafter, we call these parts "knobs".

On the other hand, small impacts could cause a quasi-static spin-up. It is reported that the debris trail of asteroid P/2012 A2, orbiting in the main asteroid belt, was observed and its origin could probably be a non-catastrophic collision [170, 84]. However, since small impacts would input the spin acceleration randomly, it may be difficult to explain the present principal axis mode of (216) Kleopatra's rotation. For these reasons, assuming that an accretion process due to a catastrophic disruption originates the formation of (216) Kleopatra, we choose the linear-loading profile defined above.

4.5   Parameter Representations

We develop a 3-dimensional finite element model of (216) Kleopatra on ANSYS academic research, ver. 14.0. The constant properties used here are shown in Table 1.1. The Ostro et al. shape model will be fixed in the following analysis, but we will investigate the stress configurations for three difference size scales, i.e., the Ostro et al. size, the Descamps et al. size, and the Marchis et al. size. The rotation period and the mass were obtained by Magnusson [97] and Descamps et al. [36], respectively. Based on a typical soil on the earth, the friction angle is considered to be $35°$ [91], while the dilatancy angle is chosen to be half of the friction angle [28]. For the elastic computation, Young's modulus is defined as 1.0×10^2 MPa, allowing for elastic deformation within 1% of its total size, while Poisson's ratio is fixed at 0.25, giving compressibility of the volume. Note that different Poisson's ratios do not change the trends of elastic solutions.

In the following discussions, the ratio of the current stress to the yield stress, later known as the stress ratio [89], is used to describe the plastic state. The equivalent stress, which represents the current stress, is written as

$$\sigma_e = \alpha I_1 + \sqrt{J_2}, \tag{4.13}$$

where I_1 and J_2 are calculated by the current stress. On the other hand, the yield stress is defined as

$$\sigma_y = k, \tag{4.14}$$

where k is given in Eq. (4.10). Using σ_e and σ_y yields the stress ratio, N:

$$N = \frac{\sigma_e}{\sigma_y}. \tag{4.15}$$

Elements having $N = 1$ are in a plastic state.

Theoretically, the stress ratio does not exceed 1.0, equal to the condition at which the stress configuration is the same as the yield stress. However, since numerical errors cause the ratio to violate the theoretical condition, we monitor the present finite element model so that its error at the final step is always within 1 %, i.e., the maximum value of the stress ratio is always below 1.01.

Chapter 5

Application to Asteroid (216) Kleopatra

Using the established techniques in the previous chapters, we consider (i) size estimation of (216) Kleopatra, (ii) formation of its satellites, and (iii) possible failure modes due to different sizes. In this study, we consider surface shedding and structural failure to be common failure modes. Given the spin period (5.385 hr), the Ostro et al. shape model (Table 1.1), and the mass, we investigate these points dynamically and structurally. First, assuming that materials are cohesionless, we discuss a structurally stable size of (216) Kleopatra by the limit analysis technique introduced in Chapter 3. To apply this technique, we will define three different parts and compare the upper bounds of these volumes to determine a closer condition to the actual failure point. Second, by using the dynamical analysis discussed in Chapter 2, we analyze a possible formation of the small satellites. In this analysis, we consider a possibility of surface shedding of (216) Kleopatra and formation of the small satellites. Then, we use the finite element model developed in Chapter 4 to investigate detailed failure modes of this object. In the finite element model, we do not apply the zero-cohesion assumption used in the limit analysis technique.

For this analysis, we appreciate Dr. Pascal Descamps for the information about the estimation for the orbits of the satellites and Dr. Petr Pravec for useful discussion about the spin barrier for large elongated asteroids.

5.1   Definition of Slices

The body of Kleopatra is separated into five different slices and we take three of them (Fig: 5.1). Slices 1 and 3 includes the knobs on the left and right sides, respectively. Slice 2 is the bifurcation part. These slices are perpendicular to the minimum moment of inertia axis. The definition of these slices allows us to characterize the effect of the knobs and the bifurcation part on structural conditions.

5.2   Structurally Stable Size

In this section, we show the results given in the range of the size scale from 1.0 to 1.5. In the following section, we call this range the test scale range.

5.2.1   Structural Failure as a Function of Size by Limit Analysis Technique

First, we discuss a lower bound for structural failure of this body. Since elastic solutions are independent of Young's modulus, we set the modulus as 10 GPa, which may be larger than usual geological materials on the Earth. On the other hand, since different Poisson's ratios provide different solutions, we consider two different Poisson's ratios. The one is 0.2, while the other is 0.333. These Poisson's ratios are in a compressive region. In the experiments, we investigate 25 size scales in the test scale range, i.e., $\alpha = 1.00, 1.02, 1.04, ..., 1.50$. We find that for all the size scales stress states violate the MC condition even when $\phi = 90°$, corresponding to the condition where a material is resistant to the shear stress. Therefore, (216) Kleopatra has plastic deformation of some small elements somewhere in all the test scale range and its internal structure is above a lower bound for structural failure.

Figures 5.2 through 5.4 show elastic solutions for the cases with $\alpha = 1.00$, $\alpha = 1.30$, and $\alpha = 1.50$, respectively. Each case shows Poisson's ratios of 0.2 and 0.333. In these figures, the regions with $\phi > 50°$ by stars and those with $\phi = 90°$ by circles. The dots describe the shape of (216) Kleopatra. The finite element analyses indicate the following results. First, although different
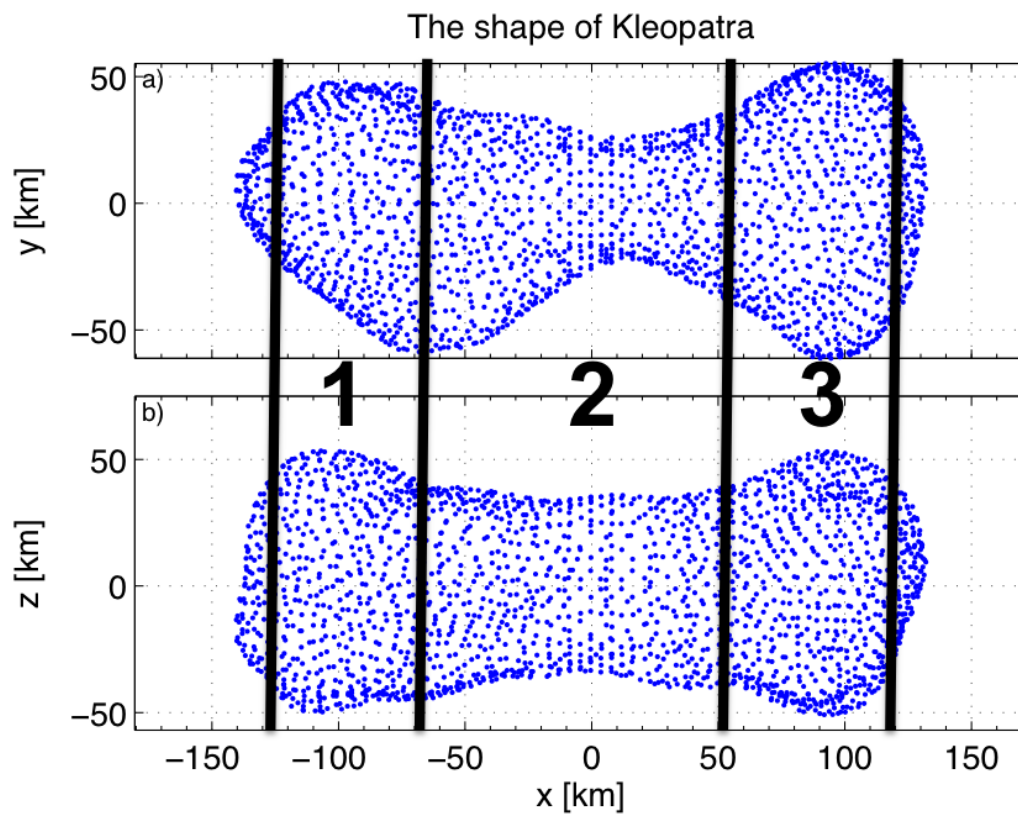
Figure 5.1: Definition of slices. The projection plot is based on Fig. 1.5.

Poisson's ratios give different trends, the stress solutions are not significantly different. In Fig. 5.2, the stars appear around the surface of the neck, while the circles are scattered on the whole surface. In Fig. 5.3, the stars are around the surface of the neck, but on the opposite side of $\alpha = 1.00$. In Fig. 5.4, the stars and the circles are condensed around the neck.

Next, we determine an upper bound condition for structural failure of the body by the partial volume technique developed in the previous sections. Assume that a material of the body is cohesionless. Figure 5.5 describes upper bound conditions for structural failure, especially, the minimum friction angle that keeps the original shape, as a function of the size scale. The narrow solid, dashed, and dotted lines show upper bounds for structural failure of slice 1, 2, and 3, respectively. The upper bold solid line shows the upper bound for the partial volume given by a comparison of these slices, while the lower bold solid line is the upper bound for the whole volume. The shadow area is a structurally stable region. Calculation of the upper bound condition for the partial volume reveals that the narrow solid and dotted lines are always lower than the condition for slice 2, so the upper bound for the partial volume (the bold solid line) corresponds to that for slice 2. The result implies that the bifurcated part is the most sensitive to structural failure. This may be because the bifurcation part is a smaller area and has to hold stronger (either tensional or compressional) stresses.

The shadow region in Fig. 5.5 indicates that the stable region highly depends on the size scale. If the body size is equal to the Ostro et al. (2000) size, then the critical friction angle is $37°$. As the size scale increases, the critical friction angle decreases down to $10°$. However, if the size scale is larger than 1.3, the critical friction angle dramatically increases and reaches $90°$ at a size scale of 1.36. Note that since the shape is not perfectly symmetric, σ_3 maximumly includes 14 % error, i.e., $\epsilon = 0.14$.

A friction angle of a typical geological material depends on the porosity of a material [160]. (216) Kleopatra's surface properties are comparable to lunar soil, and the surface bulk density is 3.5 g/cm^3, consistent with either a solid enstatite-chondritic surface or a metallic surface with porosity of less than 60 % [117]. However, since the earlier studies argued that the surface material may

be highly metallic, the latter hypothesis is more reasonable. For simplicity of our discussion, we assume the porosity of this asteroid to be 44 %, the mean of lunar soil (33 - 55 %), and the friction angle to be 32° (Figures 5(a) on p.309 in Scott [160]). Thus, the structurally stable region for this asteroid is more constrained and is now the area enclosed by the critical friction angle (the upper bold solid line) and a friction angle of 32° (the bold dot-dashed line). This actual stable region includes the size scale ranging from 1.08 to 1.34.

This gives a constraint on the size scale. (216) Kleopatra cannot hold the current neck part unless the actual size is between 1.08 and 1.34. This implies that the Ostro et al. (2000) size, 1.00, may be too small, while the Marchis et al. (2012) size, 1.37, may be too large. Thus, only the Descamps et al. (2011) size is a reasonable size that can allow the original body to be structurally stable. In addition, since this range of the size scale gives a bulk density from 2.9 to 3.8 g cm^3, our estimation is consistent with the surface reflectivity by Ostro et al. (2000) and with the mass estimation by Descamps et al. (2011).
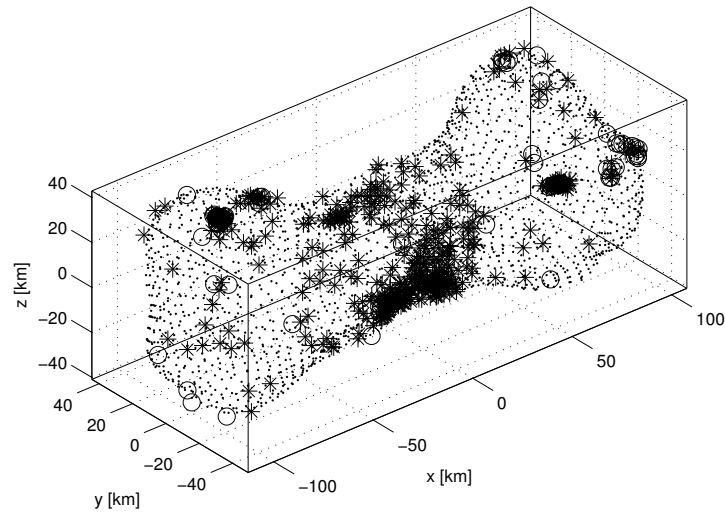
(a)
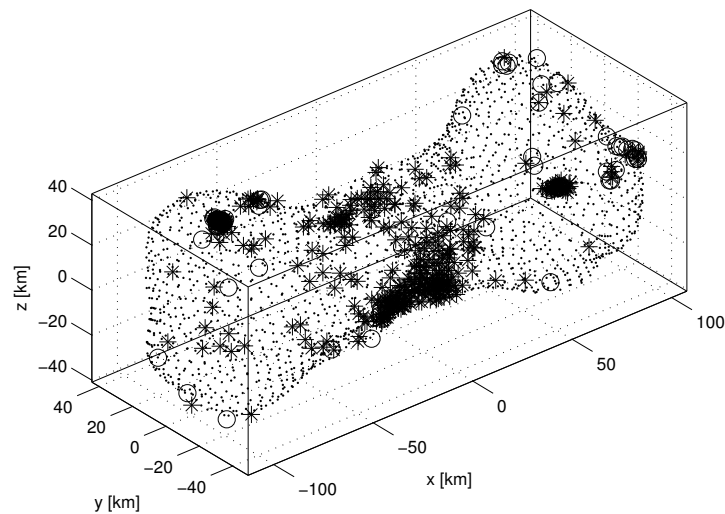
(b)

Figure 5.2: Elastic solutions for $\alpha = 1.00$. The stars describes the stress states of which friction angle exceeds $50°$. The circles mean that the stress states cannot be in the elastic region, even when the friction angle is $90°$. The dots describe the shape of (216) Kleopatra. Figure 5.2(a) indicates the solution for Poisson's ratio = 0.2, while Fig. 5.2(b) shows the solution for Poisson's ratio = 0.333. It is found that different Poisson's ratios give different results, but they have the similar features. The stars mainly appear around the surface of the neck, while the circles are scattered on the whole surface.
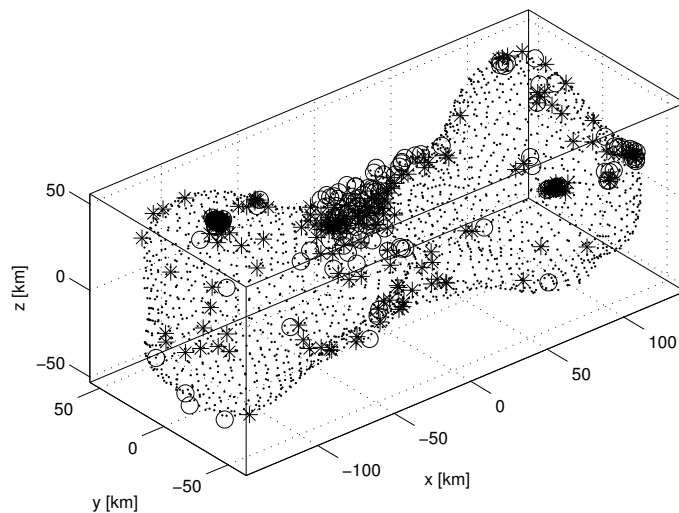
(a)
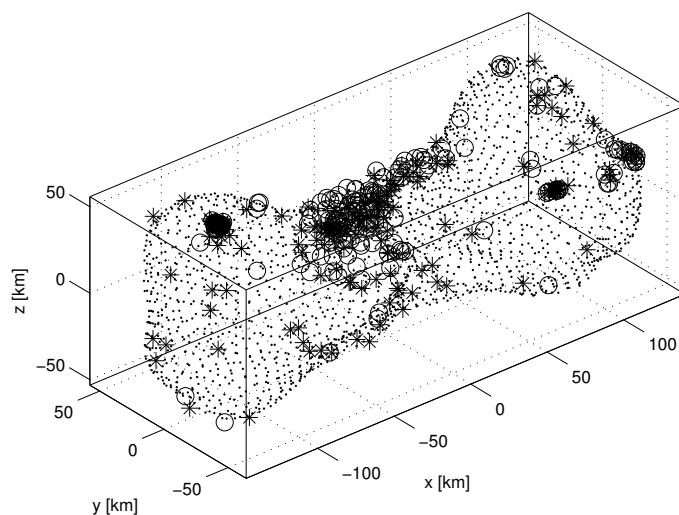
(b)

Figure 5.3: Elastic solutions for $\alpha = 1.30$. We use the definitions given in Fig. 5.2. The stars assemble on the surface of the neck; however, in contrast to $\alpha = 1.00$, their locations are the opposite side of the neck. The circles also appear near the stars.
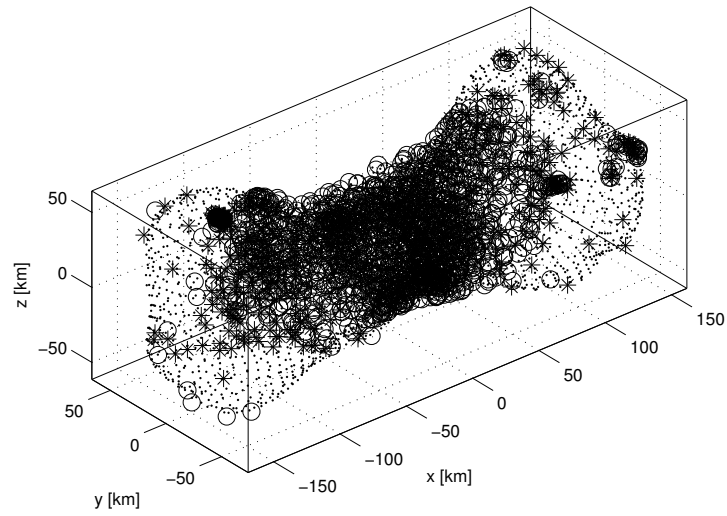
(a)
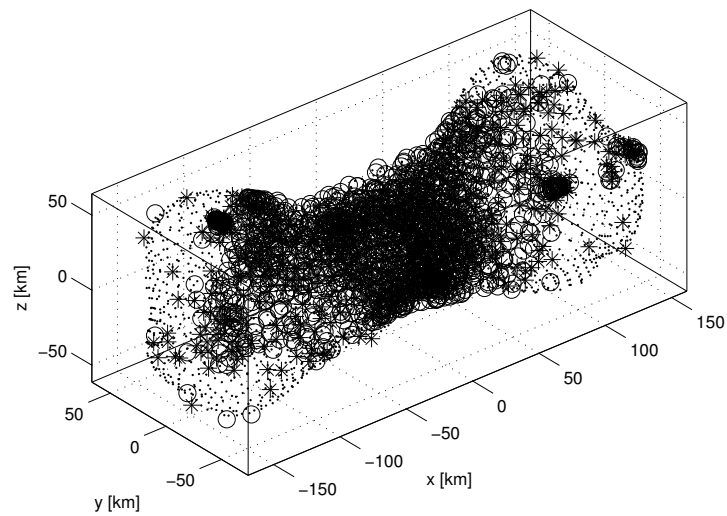
(b)

Figure 5.4: Elastic solutions for $\alpha = 1.50$. Again, we use the definitions given in Fig. 5.2. In this case, the stars and circles spread out the whole neck.

5.2.2   Surface Shedding by Dynamical Analysis

5.2.2.1   First Shedding Condition

Consider the Descamps et al. (2012) size. Figure 5.6(a) shows the zero-velocity curves at the current spin period, while Fig. 5.6(b) describes those at the spin period at the surface shedding condition (2.85 hr). In these figures, the red dots describe the shape projection onto the equatorial plane, each contour curve indicates the same energy level, the asterisks give dynamical equilibrium points. This body has four different dynamical equilibrium points: two saddle points along the minimum moment of inertia axis and two center points along the intermediate moment of inertia axis. At the current spin period, a massless particle on the surface is in Kleopatra's gravity dominant region and cannot fly off because none of the dynamical equilibrium points touch the surface (Fig. 5.6(a)). At a spin period of 2.81 hr, since the saddle point on the left side touches the surface, small particles there should take off.

We note that Yu and Baoyin [194, 195] used the same technique given above to investigate the zero velocity curves and the equilibrium points of (216) Kleopatra. However, we emphasize that our computation results are different from their results by the following reason. This paper uses a constant mass of 4.64×10^{18} kg based on comprehensive observations by Descamps et al. [36]. On the other hand, although Yu and Baoyin [194, 195] stated that Descamps et al. [36] obtained an accurate mass, they utilized the estimations by Ostro et al. [117], i.e., a volume of 7.09×10^5 km^3 and a density of 3.6 g/cm^3. Table 5.1 describes computational comparison between Yu and Baoyin [194, 195] and our calculation.

Next, we discuss the spin period at the surface shedding condition in the test scale range. Figure 5.7 indicates the relation between the spin period at the surface shedding condition (the dotted line) and the current spin period (the dashed line). It shows that the spin period at the surface shedding condition is always faster than the current spin period. To compare surface shedding with structural failure, we also plot the spin period of upper bounds for the total volume, always faster than that for the partial volume, with friction angles of 0°, 45°, and 90° by solid lines.
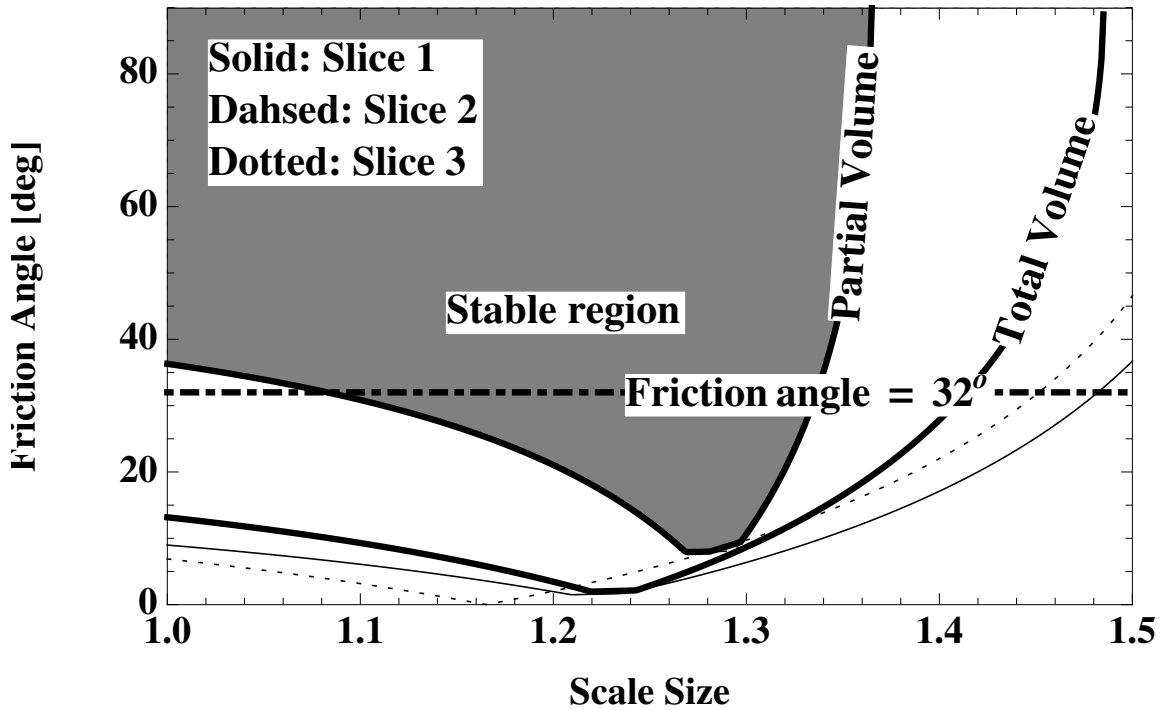
Figure 5.5: Upper bounds for structural failure of the whole volume and the partial volume. The narrow solid, dashed, and dotted lines show upper bounds for structural failure of slice 1, 2, and 3, respectively. The upper bold solid line shows the upper bound for the partial volume given by a comparison of these slices, while the lower bold solid line is the upper bound for the whole volume. The bold dot-dashed line gives a friction angle of 32°. The shadow area is a structurally stable region.

Table 5.1: Comparison of the equilibrium points by Yu and Baoyin [194, 195] and our computations. Notations E_i $(i = 1, .., 4)$ are based on Table 1 in Yu and Baoyin [194]. We recovered their results by our code. The outputs are slightly different from their values in Table 1 in [194] because of our convergent threshold defined in our code.

Property		Yu and Baoyin [194, 195]	our computation
Volume [km^3]		7.09×10^5	7.09×10^5
Density [g/cm3]		3.6	6.5
Mass [kg]		2.55×10^{18}	4.64×10^{18}
Equilibrium [km]			
	x	1.43×10^2	1.66×10^2
E_1	y	2.44	2.27
	z	1.18	7.91×10^{-1}
	x	-1.45×10^2	-1.67×10^2
E_2	y	5.19	4.97
	z	-2.72×10^{-1}	-5.47×10^{-2}
	x	2.22	1.26
E_3	y	-1.02×10^2	-1.31×10^2
	z	-2.72×10^{-1}	1.71×10^{-1}
	x	-1.17	-1.59
E_4	y	1.01×10^2	1.30×10^2
	z	-5.46×10^{-1}	-3.32×10^{-1}

Since the spin period at the surface shedding condition is always faster than that of upper bounds for structural failure of the total volume, the body experience structural failure first. The current spin period cannot be faster than the spin period at the surface shedding condition in the test scale range.

Although the spin period at the surface shedding condition is obtained numerically, the force balance between the gravity and the centrifugal force, i.e., $r_{Ostro}\alpha\Omega_{cr}^2 \propto GM/(r_{Ostro}\alpha)^2$, gives an analytical trend as

$$T_{cr} \propto \alpha^{3/2}, \tag{5.1}$$

where r_{Ostro} is the distance between the origin and the surface of (216) Kleopatra with the Ostro et al. (2000) size, M is the mass, α is the size scale, Ω_{cr} is the spin rate at the surface shedding condition, and $T_{cr} = 2\pi/\Omega_{cr}$.

5.2.2.2   Hypothesis of the Origin of the Satellites

This section discusses the formation of the satellites. Descamps et al. [36] argued that these satellites may be byproducts of a spin-up process leading to surface shedding. We use the technique for determining the surface shedding condition. Since we have already seen the zero-velocity curves of this asteroid earlier, we only track the location of the equilibrium points. The physical properties of the satellites are introduced in Descamps et al. [36] (Table 1.2) and the orbital planes of the satellites are assumed to be parallel to the equatorial plane of (216) Kleopatra.

We consider the satellites to be small, uniform spheres and call these satellites the test bodies. Initially, the test bodies are located at the edges along the minimum moment of inertia axis. The conservation of the total angular momentum gives the initial spin period, implying that we neglect any mass ejection other than surface shedding forming the satellites. On the assumption of zero eccentricity, the initial spin rate of (216) Kleopatra, ω_0, is given as

$$\omega_0 = \frac{I_z\omega_c + m_1 R_1\Omega_1^2 + m_2 R_2\Omega_2^2}{I_z + (m_1 + m_2)r_{Ostro}^2\alpha^2}, \tag{5.2}$$

where m_i and R_i, $(i = 1, 2)$, are the mass and the current distance from the center of mass, respectively. I_z is the moment of inertia of the z axis. ω_c is the current spin rate. Substitutions of the physical values on Table 1.2 into this equation determines the initial spin period as 5.086 hr.

In this model, if the shedding condition of the test bodies satisfies, it is possible for these bodies to initiate the satellites' formation. This is equivalent to the condition where the saddle points are closer to the surface than the center of mass of the test bodies at this spin period. However, in this analysis, to make a stronger condition, we define that the test bodies lift off when the distance between the saddle points and the surface is less than the sum of these bodies' diameters, i.e., 15.8 km.

Figure 5.8 shows the distance of the saddle points from the surface (the solid lines) and a distance of 15.8 km (the dashed line). Since surface shedding may occur on the left and right sides at almost the same rotation period, we track the distances of both of these points. The saddle point on the left side is always closer to the surface. The result shows that in the test scale range, the distances between the saddle points and the surfaces are never shorter than 15.8 km, and the test bodies cannot lift off the surface. It implies that the satellites do not result from surface shedding due to static spin-up, but may involve other processes such as reaccumulation of an impact-generated debris disk.

5.3   Plastic Deformation Modes by Finite Element Modeling

In the previous section, we used limit analysis to determine lower and upper bounds for structural failure. To determine a lower bound condition, we calculated elastic solutions by finite element model. To consider an upper bound condition, we investigated the yield condition of the averaged stress over a target volume. These analysis techniques are useful when used to estimate rough conditions for structural failure. However, these techniques may be limited to determine detailed failure modes of structural failure. Using the finite element model developed in the previous section, we analyze detailed failure modes of (216) Kleopatra. Here, we set a friction angle of $35°$, which is different from the setting used for the upper bound calculation, i.e., $32°$. However, this

difference is negligible for the finite element model, especially, determination of cohesive strength. The results are tabulated in Table 5.2.

Consider the Ostro et al. (2000) size, i.e., the body with a size scale of 1.00. The bulk density for this case is 6.7 g/cm^3. Figure 5.9 shows the stress ratio of the solution from different views and the total mechanical strain, i.e., the sum of plastic strain and elastic strain. Figures 5.9(a) through 5.9(c) describe the surface, the cross section normal to the y axis, and the cross section normal to the x axis, respectively. In these plots, the red regions show the stress ratio, N, ranging from 0.95 to 1.01, while the different-colored regions describe elastic regions, i.e., $N < 0.95$. Figure 5.9(d) shows the total mechanical strain in the x axis. This plot indicates that the bottom of the neck experiences strong negative strain, while the top of the neck does not; therefore, the failure mode would result from a moment bending the body downward and a strong compression of the neck. The critical cohesive strength is 1.77×10^3 kPa. If cohesive strength is lower than this value, the solution cannot converge because the plastic region expands over the cross section of the neck and the body collapses.

The Descamps et al. (2011) size is the body with a size scale of 1.22. For this case, the bulk density is calculated as 3.6 g/cm^3. Figure 5.10 describes the stress ratio and the total mechanical strain for this case. Compared to the Ostro et al. (2000) size, the Descamps et al. (2011) size does not have strong strain in the internal body (Fig. 5.10(d)), but experiences plastic deformation on the majority of the surface (Figs. 5.10(a) through 5.10(c)). This indicates that although the internal structure is stable, the majority of the surface is quite sensitive to structural failure. In other words, the internal structure is elastic and can still hold the shape of the body. The critical cohesive strength for this case is 2.54×10^2 kPa, a factor of ~ 7 less than that of Ostro et al. (2000) size.

For the Marchis et al. (2012) size, i.e., the body with a size scale of 1.36, the bulk density is 2.5 g/cm^3. The critical cohesive strength is computed as 6.85×10^2 kPa, 2.5 times as large as that of the size scale 1.22. With this cohesive strength, the top of the neck deforms plastically (Figs. 5.11(a) through 5.11(c)). The mechanical strain is tensile over the neck, especially, at the top of the

neck (Fig. 5.11(d)). Therefore, the failure mode of this size would result from a moment bending the body downward and a catastrophic stretching of the neck.

The previous section concluded that under the assumption that materials of (216) Kleopatra are cohesionless, (1) only the Descamps et al. (2011) size is structurally stable and (2) the neck is the most sensitive part to structural failure. Specifically, applying limit analysis to the cross section of the neck, they investigated its sensitivity to structural failure. From the present study, on the other hand, we give new implications of possible failure modes of (216) Kleopatra.

Although in the previous section we assumed that materials of the body are cohesionless, we confirm that for the shape model used here, cohesive strength cannot be ignored to keep its shape. To obtain converged solutions, the Ostro et al. (2000) size, the Descamps et al. (2011) size, and the Marchis et al. (2012) size need minimum cohesive strength of 1.77×10^3 kPa, 2.54×10^2 kPa, and 6.85×10^2 kPa, respectively. This indicates that it is necessary for this body to have cohesive strength on the order of 100 kPa - 1000 kPa to keep the original shape. Our results may show that cohesive strength needed for asteroids is higher than that predicted by the preceding studies. Sánchez and Scheeres [135] reported that for a hundred-meter-sized asteroid the order of cohesive strength may be less than a few hundred pascals. Considering the mutual dynamics and breakup condition, Hirabayashi et al. [58] (see Chapter 7) also obtained cohesive strength of main belt comet P/2013 R3 (about hundred meters in size) as 40 - 210 Pa.

The first explanation for this difference is that our analysis calculates not true cohesive strength but apparent cohesive strength, which depends on pressure. For the second explanation, different pressures would change the mechanism of cohesive strength. For a small body with a few hundred meters in size (on the surface, the gravitational acceleration is on the order of 1×10^{-4} m/s^2), since internal packing may be loose, it may be reasonable to model cohesive strength by van der Waals forces [135]. However, for a large body with a few hundred kilometers in size (on the surface, the gravitational acceleration is on the order of 1×10^{-2} m/s^2), the internal structure would have much higher pressure, probably causing tighter bonding and additional attractive forces, which may give stronger cohesive strength. In fact, as seen in Sullivan et al. [172], packing effects

may cause additional cohesion.

On the other hand, referring to Housen and Holsapple [71], Holsapple [64] proposed size-dependent cohesive strength. Based on impact experiments of Georgia Keystone granite specimens, he formulated it as $\kappa r^{-1/2}$, where κ is a constant value and r is the radius of an asteroid. This formula shows that cohesive strength decreases as the size increases. Applying this formula with $\kappa = 2.25 \times 10^8$ dynes/cm^2 = 22.5 MPa, defined by Holsapple [64], we obtain cohesive strength of a body of similar size to (216) Kleopatra on the order of 100 kPa, the same order as obtained in the present analysis. Furthermore, Lambe and Whitman [91] noted that the cohesive strength of overconsolidated clay is on the order of 1000 kPa, so cohesive strength on the order of 100 kPa - 1000 kPa is still in the realm of loose materials. Therefore, it is still reasonable to consider (216) Kleopatra to be a rubble pile.

While the previous section pointed out that the stress state at the neck transits from compression to tension as the size increases, the present finite element model shows a detailed deformation process for each size scale. With a bulk density of 6.7 g/cm^3 and cohesive strength of 1.77×10^3 kPa, the Ostro et al. (2000) size could have compressive failure at its neck. For this case, because of the high density, since the gravitational force exceeds the centrifugal force, the neck, the narrowest part in the body, has to hold stronger compressive stresses. The deformation process results from a moment bending the body downward (Fig. 5.9(d)). While the top of the neck experiences mild compression and its stress state is elastic, the bottom fails plastically and cannot hold the original shape. On the other hand, the Marchis et al. (2012) size, the body with a bulk density of 2.5 g/cm^3, has strong tension at the top of the neck due to the centrifugal forces exceeding the gravitational forces if cohesive strength is less than 6.85×10^2 kPa. For this case, the failure mode would result from strong tension at the top of the neck, causing downward-bending of this body and a catastrophic stretch eventually.

The Descamps et al. (2011) size has a bulk density of 3.6 g/cm^3. Although the previous section stated that this size may be structurally stable, with cohesive strength of 2.54×10^2 kPa, we identify structurally unstable regions over the surface. Since the propagation of the yield

Table 5.2: Critical failure mode conditions.

Property	Small size	Intermediate size	Large size
Size scale	1.00	1.22	1.36
Mean radius [km]	55.3	67.5	75.3
Density [g/cm^3]	6.7	3.6	2.5
Cohesive strength [kPa]	1.77×10^3	2.54×10^2	6.85×10^2
Max. stress ratio	1.004	1.008	1.002
Failure mode	Compression	Landslides	Tension

condition over an arbitrary slope triggers landslides [112, 55], a body with this size and with this critical cohesive strength would probably experience large-scale landslides, but would not have catastrophic structural failure. Note that the current regions of "landslides" could be made stable by small variations in the slope of the body due to the uncertainties in the shape model. Thus, an improved shape model could have the potential to decrease the critical cohesive strength necessary to keep the current slope at the Descamps et al. (2011) size.

5.4   Conclusion

This chapter showed the application of the dynamical analysis for determining surface shedding and the averaged technique for giving an upper bound condition of structural failure to (216) Kleopatra to determine a structurally stable size of this object. Also, we used a finite element model that takes into account plastic deformation. The result showed that a structurally stable size ranges between 1.08 and 1.34, which is consistent with the size estimated by Descamps et al. [36]. The formation of the satellites of (216) Kleopatra may not result from not surface shedding but, probably, reaccumulation due to an impact. The finite element analysis indicated that (216) Kleopatra has to have cohesion to keep its original shape and could have different failure modes with respect to its size. The Ostro et al. (2000) size, the Descamps et al. (2011) size, and the Marchis et al. (2012) size required apparent cohesive strength of 1.77×10^3 kPa, 2.54×10^2 kPa, and 6.85×10^2 kPa, respectively. For the failure modes of (216) Kleopatra, the Ostro et al. (2000) size would experience compression of the bottom of the neck, the Descamps et al. (2011) size would

have global landslides on the surface, but would not have internal failure, and the Marchis et al. (2012) size would fail due to tension of the top of the neck.
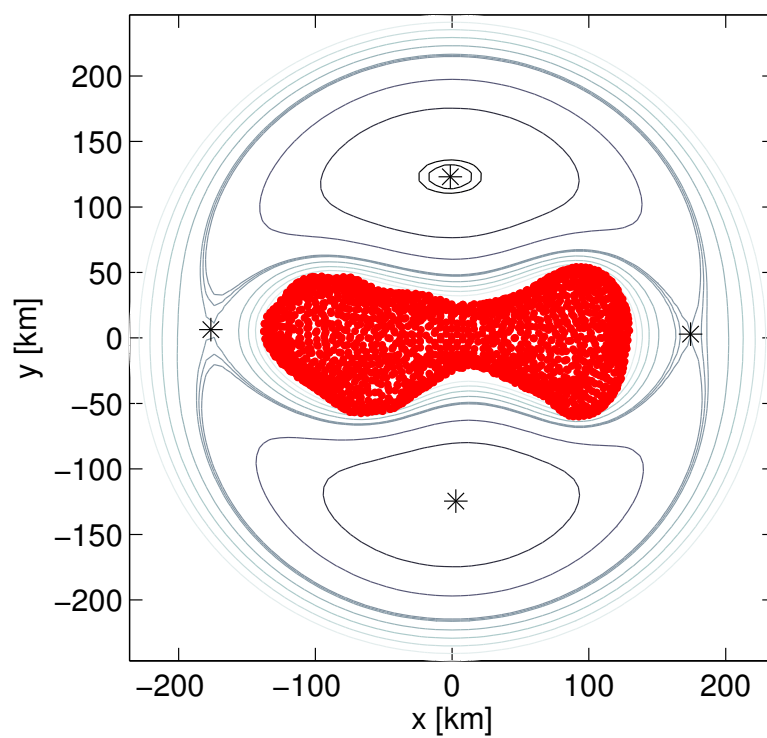
(a)
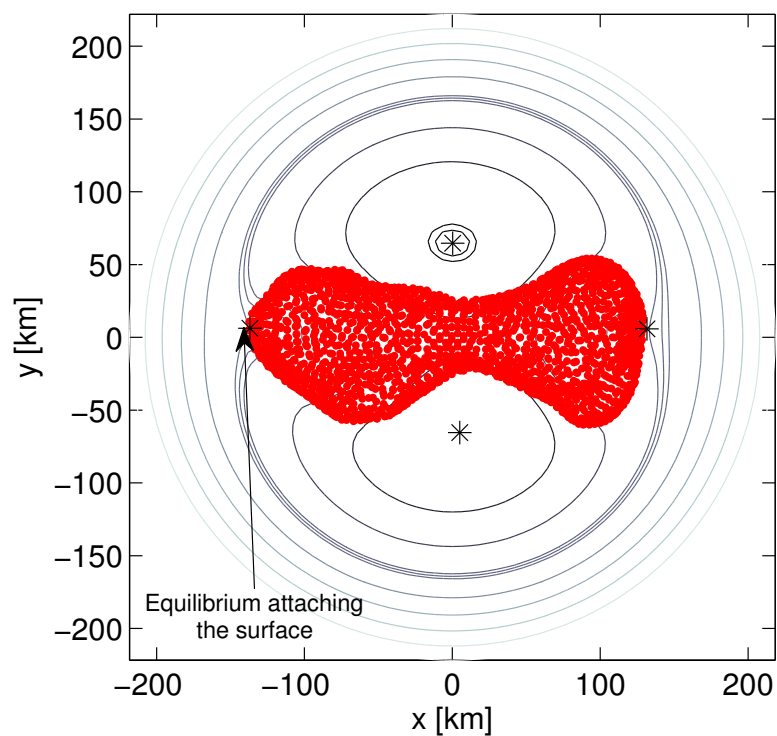
(b)

Figure 5.6: Zero-velocity curves for a size scale of 1.22, i.e., the Descamps size. Figure 5.6(a) shows the curves for the current spin period, i.e., 5.385 hr, and 5.6(b) describes those for a spin period of 2.81 hr at which the equilibrium point on the left reaches the surface.
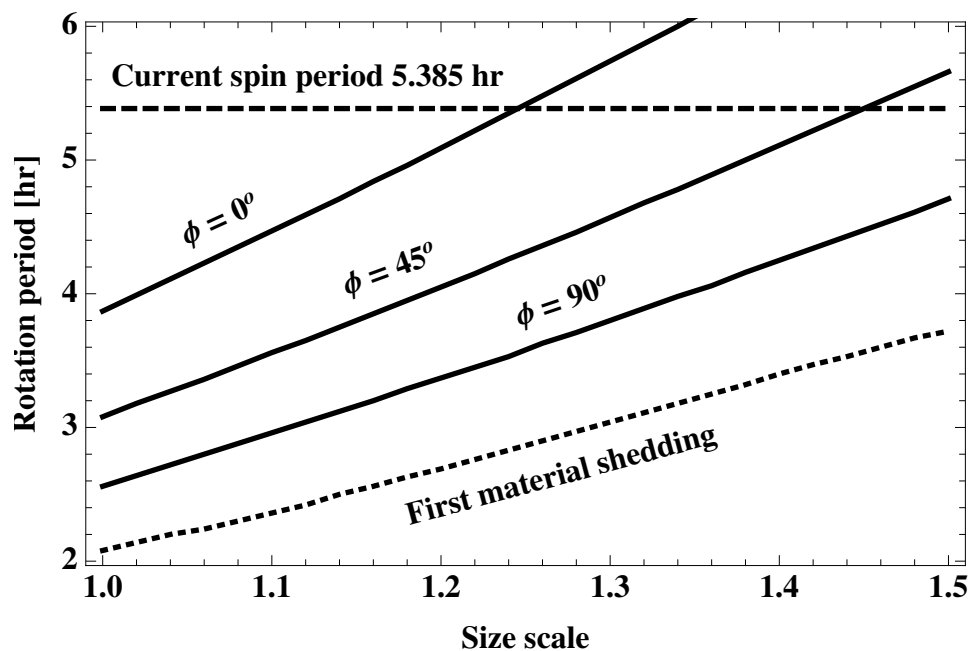
Figure 5.7: Spin period of the surface shedding condition (the dotted line) and upper bound conditions for structural failure of the partial volume (the solid lines). For the upper bound conditions, we show the cases with ϕ being 0°, 45°, and 90°.
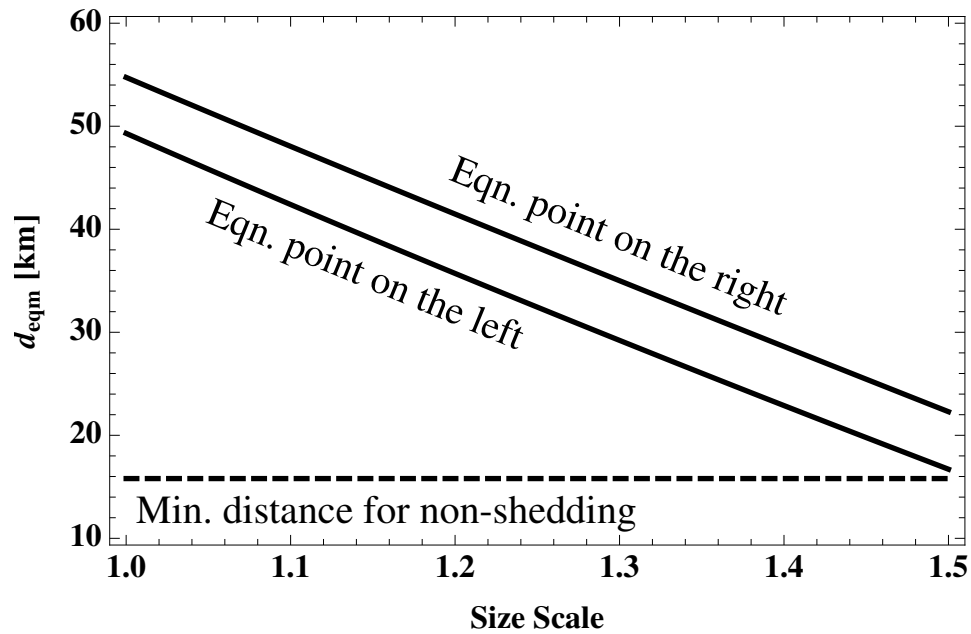
Figure 5.8: Relation between the distance of the equilibrium points from the surface (the solid lines) and the minimal distance where material shedding does not occur, i.e., 15.8 km (the dashed line). This plot shows the case of a spin period of 5.086 hr. The period is obtained by Eq. (5.2). The necessary condition of material shedding originating the satellites is that the equilibrium point on the left goes below the minimal distance.

(a)

(b)

(c)

(d)
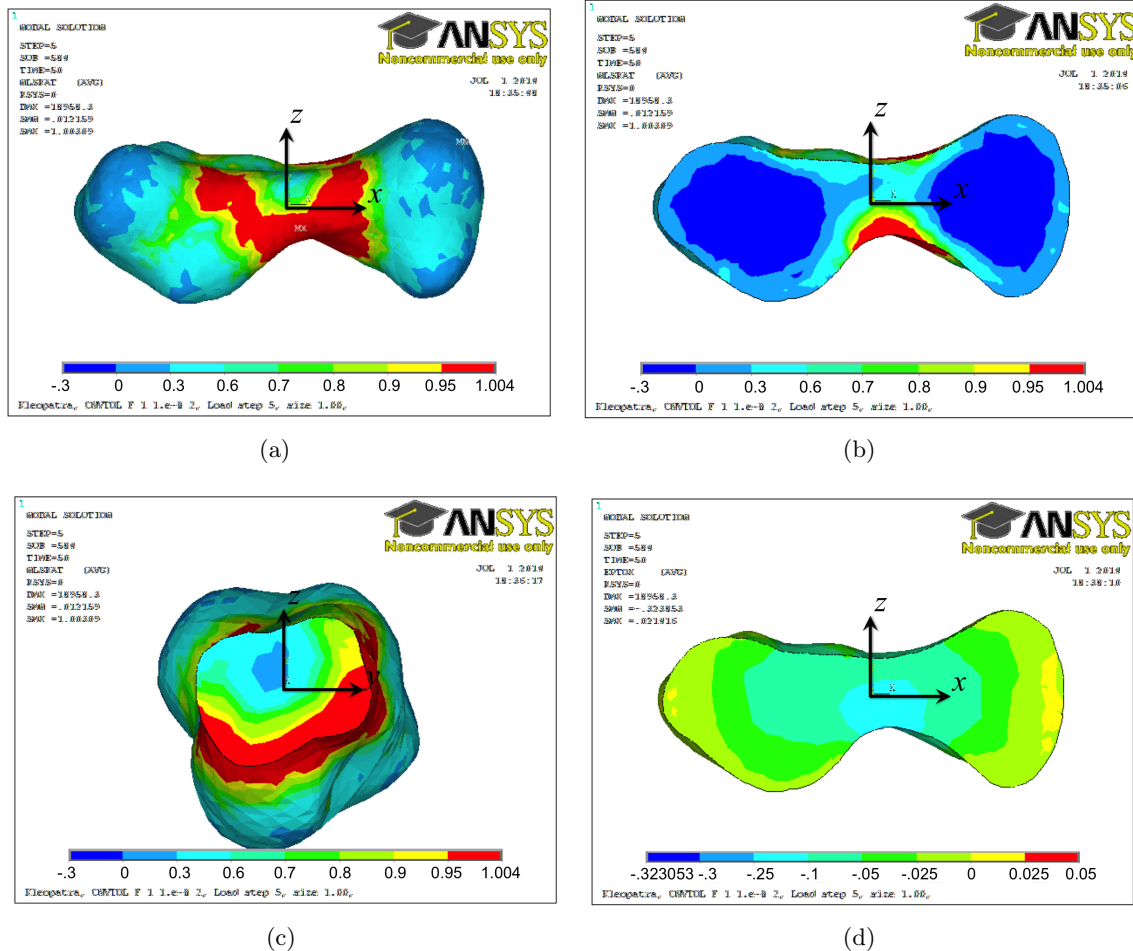
Figure 5.9: Compressional failure mode for the size scale 1.00. Figures 5.9(a) through 5.9(c) show the stress ratio, defined in Eq. (4.15), from different views. If the stress ratio is 1.0 within a 1 % error, the regions are considered to have plastic deformation. Figure 5.9(d) describes the total mechanical strain in the x axis.
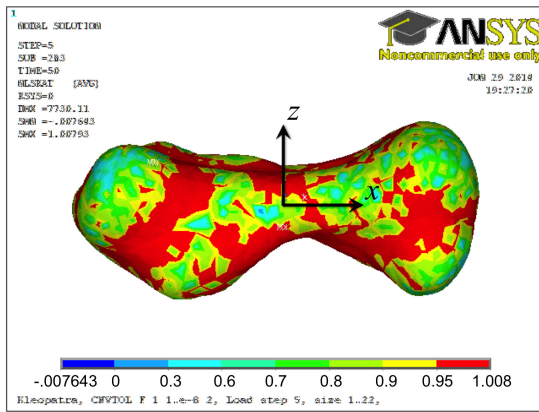
(a)
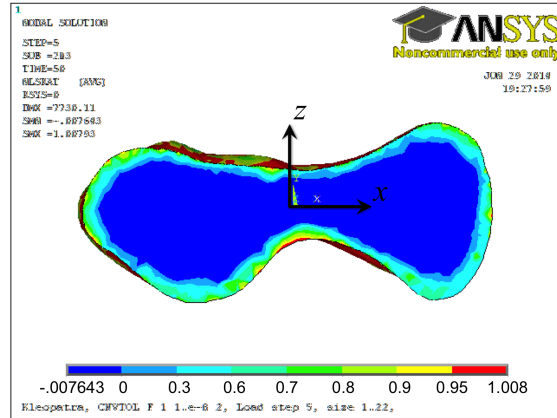
(b)
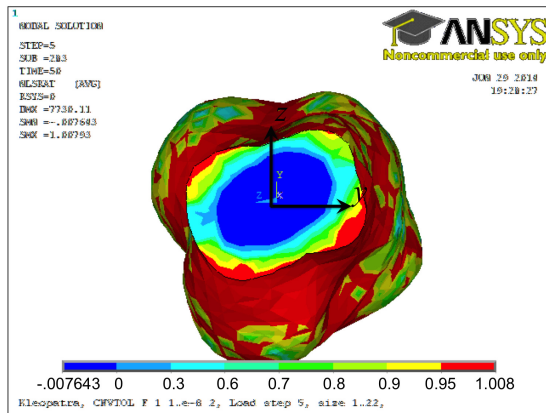
(c)
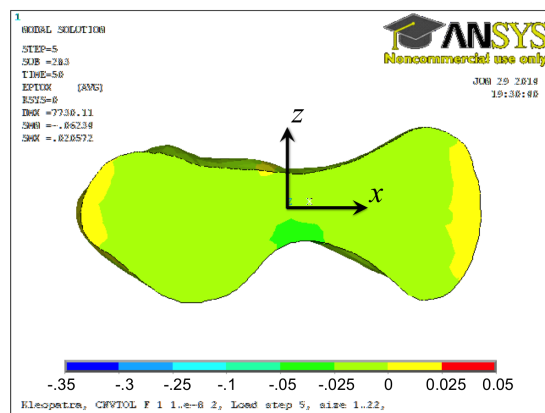
(d)

Figure 5.10: Surface failure mode for the size scale 1.22. Similar to Fig. 5.9, Figs. 5.10(a) through 5.10(c) show the stress ratio from different views. Figure 5.10(d) describes the total mechanical strain in the x axis.

(a)

(b)

(c)

(d)
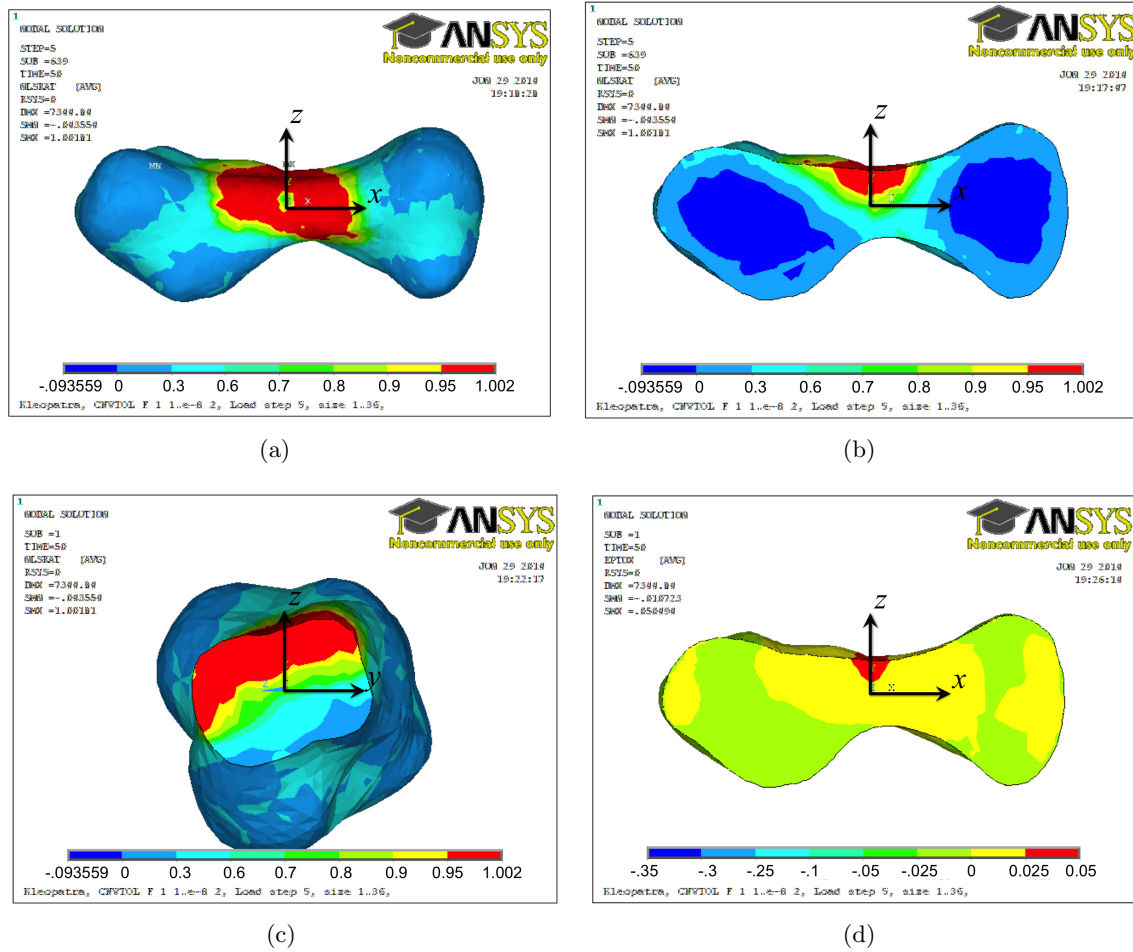
Figure 5.11: Tensional failure mode for the size scale 1.36. Figures 5.11(a) through 5.11(c) show the stress ratio, while Fig. 5.11(d) indicates the total mechanical strain in the x axis.

Chapter 6

Application: Survey

This chapter explores the first failure mode of 21 asteroid shape models due to a YORP-type spin-up. Specifically, we determine the spin rate and the friction angle for the first failure, considering two body failure modes: material shedding from an asteroid's surface and structural failure of a body. We assume that asteroids' materials are uniformly distributed (i.e., constant density) and cohesionless and the friction angle is 40°. The friction angle used here is different from that defined in the previous chapters. However, since the friction angle of a typical geological material ranges between 25° and 45° degrees, the value chosen here is still useful to consider the internal structure of an asteroid. We only take into account the centrifugal and self-gravitational accelerations. This chapter studies those failure modes by using different techniques. Surface shedding is given by the spin rate at which one of the equilibrium points touches an asteroid's surface, while structural failure is investigated by limit analysis, which provides the upper bound of structural failure. Using these methods, we determine the first failure mode of real shapes. The results show that real shapes are quite different from ellipsoids. All ellipsoids experience structural failure first, while real shapes may not. To determine the failure modes of each asteroid, we also propose a shape classification of asteroids according to their shape types ('sphere', 'ellipsoid', and 'bifurcation') and the two failure modes. It shows that all the asteroids settle into four different classes: (i) a spherical body undergoing structural failure, (ii, iii) ellipsoidal bodies experiencing either structural failure or surface shedding, and (iv) a bifurcated body failing by structural failure. Furthermore, for asteroids spinning near the spin limit, our technique re-evaluates their bulk density

estimated by earlier works. Specifically, some bifurcated shapes are sensitive to structural failure, so their bulk density can be constrained.

6.1   Outline of the Present Chapter

This chapter focuses on failure modes due to a YORP effect. Note that some asteroids are too large to be influenced by a YORP-induced spin. Those asteroids' spins may be accelerated by different mechanism such as small impacts and tidal effects. We do not discuss how they can accelerate. The main contributions of this chapter is (i) to develop a way to determine the first failure mode of general asteroids' shapes and (ii) to classify 21 shape models according to their shapes and the first failure modes.

This chapter considers two failure modes: dynamical failure due to shedding of loose material from the surface and structural failure due to plastic collapse of a body. Surface shedding is a process wherein surface particles are lofted from the surface due to centrifugal accelerations overcoming gravitational accelerations. This mode causes a body to lose material from its extremities, where it undergoes further evolution. We compute the first condition of this mode by tracking the dynamical equilibrium points. On the other hand, structural failure occurs when uncontained plastic flow propagates over a large area that connects the surface. This failure mode causes a body to catastrophically deform and eventually break into smaller components. To find the condition, we calculate the upper bound condition in terms of limit analysis. Note that some researches reported that these two modes are highly correlated. However, understanding this correlation is beyond this chapter, so we will study it in the future.

We have notes for the present research. (i) This analysis only takes into account self-gravity and centrifugal forces. (ii) We assume that a body spins in a principal axis mode, has a homogeneous density distribution, is cohesionless, and has a friction angle of $40°$, which is within usual friction angles ranging $25°$ between $45°$. (iii) We consider uncertainty of the density if the mass was accurately determined; otherwise, we assume that the density is 2.5 ± 1.5 g/cm^3. (iv) the shape models are downloaded from Asteroid radar research (http://echo.jpl.nasa.gov) and from

the planetary data system (http://sbn.psi.edu/pds). Those shapes and sizes are supposed to be accurate, so we fix them in this analysis. (v) We assume that materials of all asteroids discussed here are elastic-perfectly plastic. (vi) For (29075) 1950 DA, there are two available models: the prograde and retrograde models. Busch et al. [19] obtained these models due to uncertainty of the pole direction. Because of the large uncertainty in the pole directions ($\pm 20°$), if the prograde pole direction is changed one way, the model needs a larger equatorial extent to match the echo bandwidth, so it becomes closer to the nominal retrograde shape. Likewise, less oblateness is consistent with retrograde rotation if the pole is shifted from the retrograde nominal (Busch, 2013, personal communication). Since studying several possible models for one asteroid is also of interest, we analyze these models as different objects.

We outline the discussions of this chapter. First, we introduce techniques for determining surface shedding [52] and for obtaining structural failure [65]. Second, we use these techniques to recover the earlier studies about an uniformly rotating cohesionless ellipsoid (see [70, 52]). Note that we use a technique for determining structural failure of general bodies, so Holsapple's limit analysis [70] for an ellipsoid cannot be used. Instead, to determine the upper bound in terms of limit analysis, we apply the theorem by Holsapple [65]. Technically, this method is identical to a first moment average technique; however, since the theorem comes from limit analysis, it guarantees the upper bound of structural failure. Last, as a new scientific contribution, this chapter classifies 21 asteroid shape models according to their shape and failure modes.

6.2   Analytical Parameters for Shape Investigation by the Upper Bound Technique

In this section, we define four parameters used in the analysis of real shapes. The first and second parameters are related to structural failure, the third parameter represents the first shedding, and the last parameter characterizes the zero-tension condition in terms of the area stress.

To define the parameters related to structural failure, we review the MC yield criterion first. In Eq.(3.1), we described the criterion as a function of the friction angle and the principal stress

components of the stress-average. However, the stress-average only depends on the spin rate ω, the density ρ, and the shape geometry Θ. Since the present study considers the condition of a constant density, we can remove ρ from our discussion. Therefore, Eq.(3.1) is now rewritten as

$$g(\omega, \Theta, \phi) \leq 0. \tag{6.1}$$

Note that Θ is usually complex and cannot easily be expressed.

The first parameter is the minimal friction angle associated with the stress-average. We obtain this parameter by considering the upper bound theorem. This friction angle, which depends on the choice of the stress-average, is identical to the minimal friction angle where the original body does not experience structural failure of either the entire volume or the partial volume. This friction angle ϕ_h^*, where index h is either t or p, can be obtained as

$$\phi \geq \phi_h^* = \Psi_1(\omega, \Theta), \tag{6.2}$$

where $\Psi_1(\omega, \Theta)$ is a function given based on the equation $g(\omega, \Theta, \phi) = 0$.

The second parameter is the threshold of the spin rate associated with the stress-average. Any spin rate above this threshold leads structural failure. In contrast to the first parameter, it cannot be obtained uniquely because of ϕ in $g(\omega, \Theta, \phi)$, which is usually unknown. Here, we choose a constant value ϕ_F for ϕ. We will show ϕ_F in the next section. On this assumption, the maximal spin rate can be obtained as

$$\omega \leq \omega_h^* = \Psi_2(\Theta), \tag{6.3}$$

where $\Psi_2(\Theta)$ is given by the equation $g(\omega, \Theta, \phi_F) = 0$. Since this equation is a function of shape geometry, this parameter is useful to express it. For this reason, this chapter will use ω_t^* to characterize bodies' shapes by the failure modes and call this value an effective shape. Comparing the effective shape of real shapes with that of ellipsoids allows us to visualize the shape dependency of failure modes.

The third parameter is based on the first shedding. We define the spin rate at which material shedding starts. Any spin rate above this condition causes a body to experience surface shedding.

We can express the spin rate of the first shedding $\omega^\diamond$ as

$$\omega \le \omega^\diamond = \Psi_3(\Theta), \tag{6.4}$$

where $\Phi_3(\Theta)$ can be obtained by considering the equilibrium condition of Eq.(2.1).

The fourth parameter is the spin rate at which the area stress experiences zero-tension some-where except for the edges along the minor principal axis. The area stress, $\bar{T}_{11}^a$, is the averaged stress over a cross section perpendicular to the minimum moment of inertia axis and is a function of the location of the cross section x, as well as ω and Θ. The details are described in Sec. 6.3.2.3. Then, the zero-tension condition can be written as

$$\omega \le \omega_a^* = \Psi_4(\Theta, x), \tag{6.5}$$

where $\Psi_4(\Theta, x)$ is a function given by $\bar{T}_{11}^a(\omega, \Theta, x) = 0$. x must be $x_{min} + \epsilon \le x \le x_{max} - \epsilon$, where x_{min} and x_{max} are the location of the edges (leftmost and rightmost) and ϵ is an infinitesimal positive constant.

6.3   Surface Shedding and Structural Failure of a Uniformly Rotating Ellipsoid

Before studying surface shedding and structural failure of real shapes, we consider those of a uniformly rotating cohesionless ellipsoid. Since an ellipsoid is geometrically simple, the results obtained here are trivial, which, again, is obvious from the analysis by Holsapple [70]. However, comparing these results with real shapes is useful to show that simple theories for an ellipsoid can not be applied to real shapes any more.

We use normalized values in the following text. Let us consider an ellipsoid with dimensions of $2a$ by $2b$ by $2c$, where $a > b > c$, spinning with the spin rate ω. Dimensionless lengths are given dividing the dimensional lengths by a. The normalized size of an ellipsoid is described as $(1, \beta, \gamma) = (a/a, b/a, c/a)$. Similarly, normalized positions are denoted by (x_1, x_2, x_3). The dimensionless spin rate of ω is denoted by $\Omega = \omega/\sqrt{\pi \rho G}$. Dimensionless potential U is defined

using dimensional potential $\hat{U}$: $U = \hat{U}/\pi\rho Ga^2$. Also, the body force component b_i and the stress component σ_{ij} are normalized by $\pi\rho Ga$ and $\pi\rho^2 Ga^2$, respectively. Without confusion, we keep using the same notations to express these quantities.

According to MacMillan [96], U can be expressed as a quadratic form with shape parameters A_k ($k = 0, x_1, x_2, x_3$):

$$U = -A_0 + A_1 x_1^2 + A_2 x_2^2 + A_3 x_3^2, \tag{6.6}$$

where

$$A_0 = \beta\gamma \int_0^\infty \frac{du}{\Delta}, \tag{6.7}$$

$$A_1 = \beta\gamma \int_0^\infty \frac{du}{(u+1)\Delta}, \tag{6.8}$$

$$A_2 = \beta\gamma \int_0^\infty \frac{du}{(u+\beta)\Delta}, \tag{6.9}$$

$$A_3 = \beta\gamma \int_0^\infty \frac{du}{(u+\gamma)\Delta}, \tag{6.10}$$

where

$$\Delta = \sqrt{(u+1)(u+\beta)(u+\gamma)}. \tag{6.11}$$

Note that we fix these parameters as constant values.

b_i consists of two terms: the gravitational and centrifugal accelerations. The gravitational acceleration is given as

$$-\frac{\partial U}{\partial x_i} = -2A_i x_i. \tag{6.12}$$

The centrifugal acceleration is given as $\Omega^2[x_1,\ x_2,\ 0]^T$. Summing these accelerations, we obtain the components of the body force as

$$\begin{bmatrix} b_1 \\ b_2 \\ b_3 \end{bmatrix} = \begin{bmatrix} (-2A_1 + \Omega^2)x_1 \\ (-2A_2 + \Omega^2)x_2 \\ -2A_3 x_3 \end{bmatrix}. \tag{6.13}$$

6.3.1   Surface Shedding Condition

For a rotating ellipsoid, there are four equilibrium points: two saddle points along the minor principal axis and two center points along the intermediate principal axis [140]. As a solid ellipsoid spins faster, the centrifugal acceleration on the surface increases. The first shedding occurs when the saddle points touch the surface. Here, we can determine this condition by considering $b_i = 0$ at the extremities along the minimal principal axis. Since those extremities are $[\pm 1, 0, 0]$, the x_2 and x_3 components are always zero. On the other hand, the x_1 component gives the first shedding condition:

$$\Omega \leq \Omega^{\diamond} = \Psi_3(A_1) = \sqrt{2A_1}. \tag{6.14}$$

6.3.2   Structural Failure

The following sections introduce limit analysis associated with the volume-average stresses. We emphasize that the present chapter considers a zero-cohesion condition, which guarantees that theoretically, the lower and upper bounds of structural failure are identical. It implies that for an ellipsoid, any average techniques give the same results. However, in real shapes, this feature can no longer hold. The purpose of this section is to demonstrate the analysis technique used for real shapes.

6.3.2.1   Total Volume Stresses

We consider limit analysis associated with the total volume stress to determine the upper spin limit of structural failure of the entire volume. Here, we derive two important physical parameters: the minimal friction angle ϕ_t^* and the maximal spin rate Ω_t^* to keep the original shape. We use ϕ_t^* to determine the constraints given by the upper bound for the entire volume. On the other hand, Ω_t^* was given by Holsapple [63] who stated, "at all points, the maximal and minimal principal stresses satisfy the yield criteria; so integrating over the body, the *average* maximal and minimal principle stresses satisfy the same criteria." Again, this statement is true only if one considers a rotating

cohesionless ellipsoid.

The use of Eq. (3.17) yields the averaged stress over the whole volume of a uniformly rotating ellipsoid, later known as the total volume stress, which is written as (see e.g., [63]):

$$
\begin{aligned}
\bar{\sigma}_1^t &= \frac{1}{5}(\Omega^2 - 2A_1), \\
\bar{\sigma}_2^t &= \frac{1}{5}\beta^2(\Omega^2 - 2A_2), \\
\bar{\sigma}_3^t &= -\frac{2}{5}\gamma^2 A_3.
\end{aligned}
\tag{6.15}
$$

Substituting the total volume stress into the MC yield criterion, we obtain the relation between the friction angle and the spin rate:

$$
\Delta_1 \sec \phi + \Delta_2 \tan \phi \leq 0,
\tag{6.16}
$$

where

$$
\begin{aligned}
\Delta_1 &= \Omega^2 - 2A_1 + 2\gamma^2 A_3, \\
\Delta_2 &= \Omega^2 - 2A_1 - 2\gamma^2 A_3.
\end{aligned}
$$

From Eq.(6.16), we obtain the minimal friction angle that the body does not experience structural failure. Therefore, this inequality yields

$$
\phi \geq \phi_t^* = \arctan\left[\frac{\Omega^2 - 2A_1 + 2\gamma^2 A_3}{2\sqrt{-2\gamma^2(\Omega^2 - 2A_1)A_3}}\right].
\tag{6.17}
$$

When the equality satisfies, the stress states of all the elements in the body are on the MC yield envelope. Since A_i and γ are constant, ϕ_t^* is a function of Ω. Equation (6.17) gives an interesting insight of the stress state. In the denominator, since there is only the square root part, the inside of it should be positive. From $\gamma \geq 0$ and $A_z \geq 0$, the following condition must be satisfied:

$$
\Omega^2 - 2A_1 \leq 0.
\tag{6.18}
$$

On the other hand, in the numerator, since $\phi_t^* \geq 0$,

$$
\Omega^2 - 2A_1 + 2\gamma^2 A_3 \geq 0.
\tag{6.19}
$$

Those conditions are the necessary condition of $\phi_t^* \geq 0$.

Let us depict ϕ_t^*. Figure 6.1 shows ϕ_t^* as a function of Ω_t^*. Figure 6.1(a) and 6.1(b) indicate $\beta = 0.4$ and $\beta = 0.95$, respectively. Each line is for different γ. The results show that there is a point where $\phi_t^* = 0$, which can be written as

$$\Omega_t^\odot = \Omega(\phi_t^* = 0^\circ) = \sqrt{2(A_1 - \gamma^2 A_3)}, \tag{6.20}$$

under $\Omega^2 - 2A_1 < 0$. We denote this point by $\Omega_t^\odot$. Since $\Omega_t^\odot$ is a function of A_1, A_3, and γ, it only depends on the shape. At this point, the curves flip over non-smoothly and change the sign of their inclination. Hereafter, we call the region $\Omega < \Omega_t^\odot$ Region 1 and the region $\Omega \geq \Omega_t^\odot$ Region 2.

ϕ_t^* varies according to γ. If $\gamma \ll \beta$, ϕ_t^* keeps high values in both Region 1 and Region 2, but has high slopes near $\Omega_t^\odot$ to reach zero degrees. On the other hand, if $\gamma \sim \beta$, ϕ_t^* keeps low values, which may be near zero degrees, in Region 1, while it gradually increases as Ω gains in Region 2. It can be found that for any shapes, the body structure relaxes near $\Omega_t^\odot$, while it can be constrained at both fast and slow rotations. Note that we use a term "relax", when the minimal friction angle keeps low values.

Similarly, Ω_t^* can be given as

$$\Omega_t^* = \sqrt{\frac{2(A_1 - \gamma^2 A_3) + 2(A_1 + \gamma^2 A_3)\sin\phi}{1 + \sin\phi}}. \tag{6.21}$$

As mentioned earlier, Holsapple [63] derived a generalized form of limit spin. According to Table 1 in his paper, Eq.(6.21) is identical to the form for Case 6 where $\sigma_3 < \sigma_2 < \sigma_1$. Note that the friction angle in this equation is defined as the actual friction angle ϕ_F, so Ω_t^* becomes a function of the shape information.

Let us discuss the relation between structural failure and surface shedding. The first shedding condition was given in Eq.(6.14), while the structural failure condition was shown in Eq.(6.21). Let us take a limit of Ω_t^*, as ϕ approaches 90°:

$$\lim_{\phi \to 90^\circ} \Omega_t^* = \sqrt{2A_1}. \tag{6.22}$$
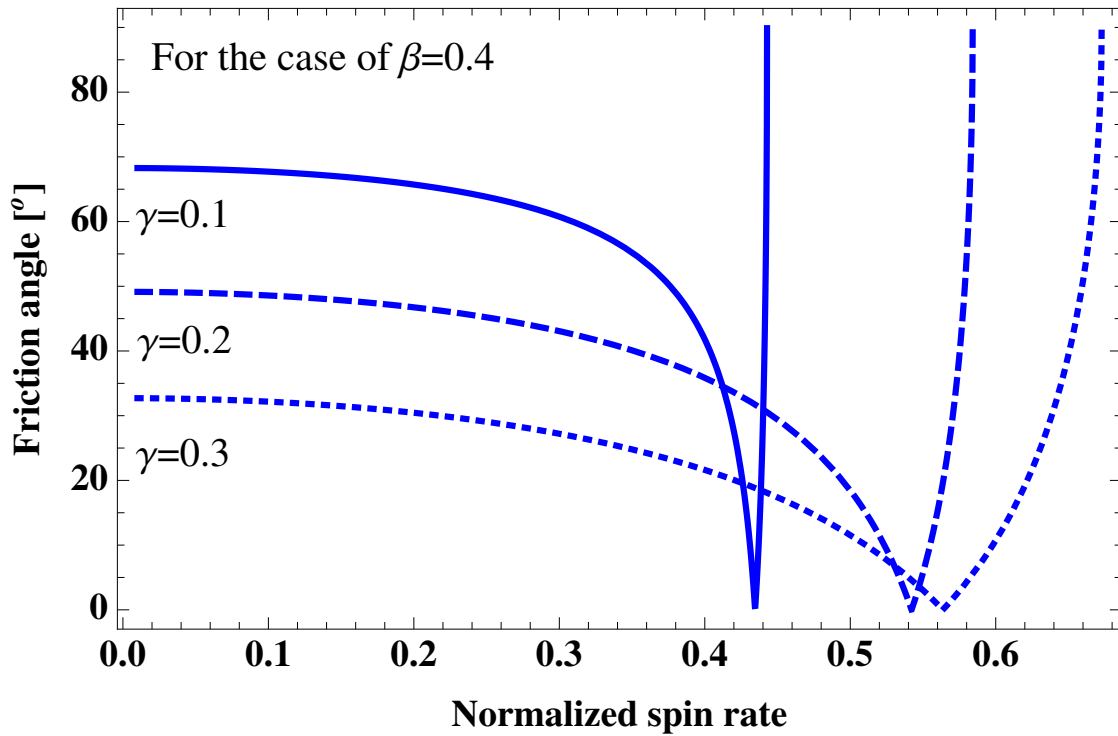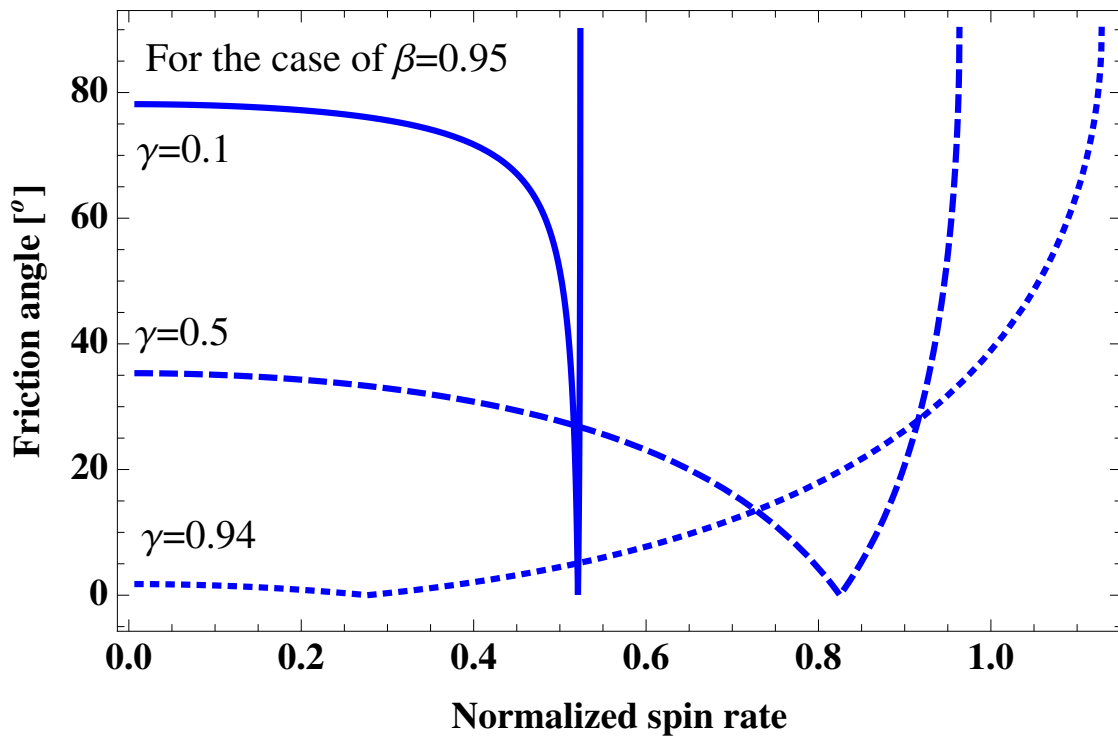
Figure 6.1: ϕ_t^* vs. Ω_t^* for an ellipsoid. (a) is for $\beta = 0.4$ and (b) is for $\beta = 0.95$.

This result is identical to $\Omega^\diamond$. It means that both structural failure and surface shedding occur at the same time only if $\phi = 90°$. Consequently, we obtain the relation:

$$\Omega_t^* \leq \Omega^\diamond. \tag{6.23}$$

We show this relation by using Holsapple's well-known limit spin plot (Fig.6.2). The blue lines describe Ω_t^* (equivalent to the results by Holsapple [63]), while the dashed red line indicates $\Omega^\diamond$. Figure 6.2(a) and 6.2(b) show the cases of $\gamma = 0.9\beta$ and $\gamma = 0.5\beta$, respectively. Note that the plots only show tension regions. It is clear that for both cases, the first shedding is equivalent to structural failure at $\phi = 90°$.

We also introduce the first shedding condition of a perfect sphere. Since $A_1 = A_3 = 2/3$ and $\gamma = 1$, the limit spin Ω_{sph}^* can be obtained analytically:

$$\Omega_{sph}^* = \sqrt{\frac{8}{3}\frac{\sin\phi}{1 + \sin\phi}}. \tag{6.24}$$

Ω_{sph}^* is always greater than or equal to Ω_t^* of any ellipsoidal shapes:

$$\Omega_{sph}^* \geq \Omega_t^*. \tag{6.25}$$

As mentioned earlier, this study assumes that asteroids are composed of materials with a friction angle of $40°$, i.e., $\phi = \phi_F = 40°$. Therefore, Ω_t^* can be rewritten as

$$\Omega_t^* = 0.78\sqrt{3.29A_1 - 0.71\gamma^2 A_3}. \tag{6.26}$$

On the other hand, Ω_{sph}^* can be

$$\Omega_{sph}^* \sim 1.07. \tag{6.27}$$

Those results must hold the relation by Eq.(6.25). For a sphere, Ω_t^* is equivalent to $\Omega_{sph}^* \sim 1.07$. Therefore, if $\Omega_t^* \sim 1.07$, the shape can be considered a body that may fail like a sphere; otherwise, the failure will look differently. Later, we classify the shapes of real asteroids based on Ω_{sph}^*.

6.3.2.2   Partial Volume Stress

The partial volume stress is a stress-average over a given slice perpendicular to the minor principal axis, which can be written in Eq.(3.17). This study considers a slice given by slicing through two different cross sections, $x = \xi^-$ and $x = \xi^+$, where $\xi^- < \xi^+$. We choose the middle component as the slice. The partial volume stress over the slice is now given as

$$
\begin{aligned}
\bar{\sigma}_1^p &= \frac{1}{4}(\Omega^2 - 2A_1)\psi(\xi^+, \xi^-), \\
\bar{\sigma}_2^p &= \frac{1}{4}\beta^2(\Omega^2 - 2A_2)\psi(\xi^+, \xi^-), \\
\bar{\sigma}_3^p &= -\frac{1}{2}\gamma^2 A_3 \psi(\xi^+, \xi^-),
\end{aligned}
\tag{6.28}
$$

where

$$
\psi(\xi^+, \xi^-) = \frac{\psi_1 - \frac{2}{3}\psi_3 + \frac{1}{5}\psi_5}{\psi_1 - \frac{1}{3}\psi_3}.
\tag{6.29}
$$

ψ_1, ψ_3, and ψ_5 are described as

$$
\begin{aligned}
\psi_1 &= \xi^+ - \xi^-, \\
\psi_3 &= \xi^{+3} - \xi^{-3}, \\
\psi_5 &= \xi^{+5} - \xi^{-5}.
\end{aligned}
$$

As mentioned earlier, for a rotating cohesionless ellipsoid, any results are identical to those of the total volume stress. Again, it comes from the fact the lower and upper bounds are the same everywhere in the body. This feature can also be seen by the partial volume stress in Eq.(6.28). The function $\psi(\xi^+, \xi^-)$ in the components can be eliminated when substituted into the MC yield criterion. As a result, for any ellipsoidal shapes, only the same terms as the total volume stress remain, which leads the same results as Eq.(6.17) and (6.21):

$$
\phi_p^* = \phi_t^*,
\tag{6.30}
$$

$$
\Omega_p^* = \Omega_t^*,
\tag{6.31}
$$

where ϕ_p^* and Ω_p^* are quantities associated with the partial volume stress.

6.3.2.3   Area Stress

The area stress is defined as the averaged stress over a cross section perpendicular to the minimum moment of inertia axis. Here, we derive the area stress from the partial volume stress to show that the area stress is a special case of the partial volume stress. We take a limit of the partial volume averaged stress, as ξ^- and ξ^- approach ξ, where ξ is the location of a cross section. Then, the limit of the partial volume stress is given as

$$
\begin{aligned}
\bar{\sigma}_1^a &= \frac{1}{4}(\Omega^2 - 2A_1)(1 - \xi^2), \\
\bar{\sigma}_2^a &= \frac{1}{4}\beta^2(\Omega^2 - 2A_2)(1 - \xi^2), \\
\bar{\sigma}_3^a &= -\frac{1}{2}\gamma^2 A_3(1 - \xi^2).
\end{aligned}
\tag{6.32}
$$

As seen by this equation, the limit case of the partial volume stress is represented by a simple quadratic function in terms of ξ. $\bar{T}_{11}^a$ defined above is identical to $\bar{\sigma}_1^a$.

Let us consider the MC yield condition associated with $\bar{\sigma}_i^a$, which can be written as

$$
\bar{\sigma}_1^a = \frac{1 - \sin\phi}{1 + \sin\phi}\bar{\sigma}_3^a.
\tag{6.33}
$$

$\bar{\sigma}_1^a$ is now dependent on ϕ and $\bar{\sigma}_3^a$. As seen in Eq.(6.32), $\bar{\sigma}_3^a$ is independent of the spin rate and is a negative constant. For this reason, $\sigma_1^a \leq 0$. If $0° \leq \phi < 90°$, then $\bar{\sigma}_1^a < 0$; on the other hand, if $\phi = 90°$, then $\bar{\sigma}_1^a = 0$. Therefore, considering the condition $\phi = 90°$ is identical to the technique by Davidsson [34]. This relation was also commented by Sharma [161]. For this reason, our partial technique gives a more accurate condition of structural failure.

The condition $\bar{\sigma}_1^a = 0$ gives another important insight for the first shedding. $1 - \xi^2$ is a non-zero term if $-1 < \xi < 1$. To obtain the zero-tension condition everywhere, we have the following condition:

$$
\Omega^2 - 2A_1 = 0.
\tag{6.34}
$$

This condition is equivalent to the first shedding condition $\Omega^\diamond$. This comes from the fact that the zero-tension condition is given by the force balance along the minor principal axis and is identical

to the first shedding condition. We can summarize those relations:

$$
\begin{aligned}
\Omega_a^* &= \Omega^\diamond = \sqrt{2A_1} \\
&= \Omega_t^*(\phi = 90^\circ) = \Omega_p^*(\phi = 90^\circ).
\end{aligned}
\tag{6.35}
$$

6.4   Asteroid Physical Properties

The physical properties of asteroid shape models used in the current survey are described in this section. Table 6.1 summarizes the properties. The following analysis considers the volume and the shape as fixed properties. For density, only a few studies estimated an accurate bulk density of an asteroid, so the bulk density of other asteroids is assumed to be 2.5 ± 1.5 g/cm^3. On the table, an asteroid's name is marked by $*$, if its density was estimated accurately. Each data type is characterized by either 'R' or 'S'. The former letter means radar observations, while the latter letter indicates spacecraft explorations. Furthermore, the dimensions and the volume are calculated based on the shape models. The following list introduces the pole direction for each asteroid by (λ, β) for the J2000 ecliptic longitude and latitude or by (α, δ) for the J2000 right ascension and declination.

6.4.1   (243) Ida

Using the Galileo images, Thomas et al. [177] resolved the shape of (243) Ida. The volume is 16100 ± 1900 km^3 and the rotation period is 4.63 hr. From orbital motion of a satellite, Belton et al. [6] estimated the primary mass as $4.2 \pm 0.6 \times 10^{16}$ kg and the density as 2.6 ± 0.5 g/cm^3. Belton et al. [6] described the mass as $4.2 \pm 0.6 \times 10^{19}$ kg, but it is a typo. The pole direction was evaluated as $\alpha = 348.8^\circ$, $\delta = 87.1^\circ$.

6.4.2   (433) Eros

(433) Eros was observed by the Near Earth Asteroid Rendezvous (NEAR) mission which determined the shape, gravity, and rotational state from radiometric tracking data, optical images,

Table 6.1: Asteroids' physical properties from observations

Asteroid System	$\hat{P}$ [hr]	$\hat{\rho}$ [g/cm³]	Dimensions [km]	V [km³]	Data	Reference
(243) Ida	4.63	$2.6 \pm 0.5^*$	$57.92 \times 30.69 \times 22.64$	1.609×10^4	S	Th96, Be95
(433) Eros	5.270	$2.67 \pm 0.03^*$	$32.87 \times 14.58 \times 11.97$	2533	S	Mi02, Ga08
(1580) Betulia	6.138	2.5 ± 1.5	$6.589 \times 5.844 \times 4.187$	81.98	R	Magri07, Ka04
(1620) Geographos	5.223	2.5 ± 1.5	$5.053 \times 2.141 \times 2.014$	8.868	R	Ma96, Os96, Hu99
(2063) Bacchus	14.90	2.5 ± 1.5	$1.107 \times 0.5275 \times 0.5183$	0.1313	R	Be99
(2100) Ra-Shalom	19.79	2.5 ± 1.5	$2.974 \times 2.478 \times 1.949$	6.203	R	Sh08
(4179) Toutatis	94.08	2.5 ± 1.5	$4.603 \times 2.290 \times 1.930$	7.670	R	Hu95, Sc98
(4660) Nereus	15.16 ± 0.04	2.5 ± 1.5	$0.5101 \times 0.3288 \times 0.2414$	0.01940	R	Br09
(4769) Castalia	4.07 ± 0.02	2.5 ± 1.5	$1.626 \times 0.9982 \times 0.8431$	0.6678	R	Os90, Hu94, Sc96
(6489) Golevka	6.029	2.5 ± 1.5	$0.6852 \times 0.4885 \times 0.5720$	0.07795	R	Hu00
(8567) 1996 HW1	8.762	2.5 ± 1.5	$3.777 \times 1.639 \times 1.492$	4.336	R	Magri11
(10115) 1992 SK	7.318	2.5 ± 1.5	$1.393 \times 0.9056 \times 0.9134$	0.5314	R	Bu06
(25143) Itokawa	12.13	$1.9 \pm 0.13^*$	$0.5629 \times 0.2985 \times 0.2432$	0.01760	S	Fu06
(29075) 1950 DA (prograde)	2.122	2.5 ± 1.5	$1.273 \times 1.207 \times 1.243$	0.8190	R	Bu07
(29075) 1950 DA (retrograde)	2.122	2.5 ± 1.5	$1.598 \times 1.450 \times 1.198$	1.146	R	Bu07
(33342) 1998 WT24	3.697	2.5 ± 1.5	$0.4756 \times 0.4328 \times 0.4037$	0.03751	R	Bu08
(52760) 1998 ML14	14.83 ± 0.15	2.5 ± 1.5	$1.036 \times 0.9666 \times 0.9869$	0.5112	R	Hu95
(66391) 1999 KW4 (Alpha)	2.765	$1.97 \pm 0.24^*$	$1.531 \times 1.494 \times 1.348$	1.195	R	Os06
(136617) 1994 CC (Alpha)	2.389	$2.6 \pm 0.6^*$	$0.6884 \times 0.6675 \times 0.6384$	0.1249	R	Fa11, Br11
2002 CE26	3.293	$0.9 + 0.5 / - 0.4^*$	$3.651 \times 3.647 \times 3.263$	21.67	R	Sh06
2008 EV5	3.725	2.5 ± 1.5	$0.4589 \times 0.4451 \times 0.4044$	0.03484	R	Bu11

$\hat{P}$ is the rotation period [hr], $\hat{\rho}$ is the bulk density [g/cm³], and V is the volume [m³]. In Reference, the author names are represented by the first two letters of their names, and the publication years are described by two digits. For exceptions, to avoid an overlap between Magri and Magnusson, we use 'Magri' for the former and 'Ma' for the latter.

and NEAR laser rangefinder (NLR) data. The mass is $6.6904 \pm 0.003 \times 10^{15}$ kg, while the rotation period is 5.270 hr. The volume was obtained as 2503 ± 25 km^3. The pole direction was estimated as $\alpha = 11.3692 \pm 0.003°$, $\delta = 17.2273 \pm 0.006°$. The bulk density was estimated as 2.67 ± 0.03 g/cm^3 [107]. The shape model was derived by Gaskell [49], using NEAR MSI images.

6.4.3 (1580) Betulia

(1580) Betulia was investigated by radar observations and photometric light curves. Magri et al. [101] confirmed that the spin period from radar observations corresponds to 6.138 hr, which was obtained by Kaasalainen et al. [85] who inverted light curve data to determine the spin vector, as well as a convex-definite shape model. Kaasalainen et al. [85] estimated the pole direction as $\lambda = 136°$, $\beta = 22°$. From the OC albedo value, Magri et al. [101] mentioned, "the near-surface bulk is less than 2.4 g/cm^3, an upper limit that is consistent with C-class taxonomy (for lunar-like 50% regolith porosity) but is not very restrictive." Also, their volume estimation was $82 \, \text{km}^3 \pm 30\%$.

6.4.4 (1620) Geographos

(1620) Geographos is considered a highly elongated shape spinning relatively fast. Magnusson [98] estimated the spin period as 5.233 hr and the pole direction as $\lambda = 55 \pm 6°$, $\beta = -46 \pm 4°$. From radar observations, Ostro et al. [118] concluded that the surface bulk density is between 2 and 3 g/cm^3. Hudson and Ostro [72] developed a physical model of this asteroid from radar and optical data.

6.4.5 (2063) Bacchus

Benner et al. [7] performed radar observations of (2063) Bacchus. Inducing a realistic bulk density for this asteroid, their modeling analysis concluded that this asteroid is not a binary configuration. The rotation pole was estimated as $\lambda = 24°$, $\beta = -26°$. They implied that the plausible density may be less than 3.6 g/cm^3 from Bacchus meteorite analogues. The side rotation period estimated by Benner [7] is 15.0 ± 0.2 hr, while that by light curve observations [128] is 14.90 hr. In

this study, the period by Pravec et al. [128] is used as a fixed value.

6.4.6   (2100) Ra-Shalom

Shepard et al. [166] investigated (2100) Ra-Shalom, a K-class asteroid, using Multi-wavelength observations. (2100) Ra-Shalom spins with a period of 19.793 ± 0.001 hr. For the pole estimation, their solution for the ecliptic longitude was $\lambda = 75° \pm 10°$, consistent with the pole reported by [85], but there were two possible solutions for the ecliptic latitude, $\beta = 16°$, $60°$. They chose the best model with a pole of $\beta = 16°$ consistent with the result from Kaasalainen et al. [85]. Using the Britt et al. [12] technique, they assumed the grain density as 3.5 g/cm^3 consistent with known C-class asteroids and estimated a bulk density of 2.4 ± 0.6 g/cm^3.

6.4.7   (4179) Toutatis

Radar observations of (4179) Toutatis revealed that this asteroid is a non-principal axis (NPA) rotator. Hudson and Ostro [75] constructed a three-dimensional shape, a spin state, and the principal moments of inertia. The rotation in a long-axis mode consists of a period of 128.84 hr for the spin about the long axis and a period of 176.4 hr for the averaged long-axis precession. Scheeres [156] assumed the homogeneous bulk density as 2.5 g/cm^3 from other asteroid properties. We assume that this asteroid spins along the maximal principal axis in the following discussion.

6.4.8   (4660) Nereus

Brozovic et al. [16] investigated a physical model of (4660) Nereus, using Arecibo and Goldstone radar observations. They obtained an ecliptic longitude of $\lambda = 25°$ and an ecliptic latitude of $\beta = 80°$. For the estimation of a shape model, they encountered an issue that all subradar latitudes remained less than $19°$, which resulted in a number of acceptable models; therefore, they introduced two reasonable models: their preferable model and alternative model (see Table 3 in their paper). In our analysis, we use their preferable model. Also, to analyze its gravitational environment, they assumed the surface bulk density as 2 to 5 g/cm^3.

6.4.9   (4769) Castalia

Radar observations by Ostro et al. [115] estimated (4769) Castalia's rotation period as 4.07 ± 0.02 hr. They also discussed that possible the grain density of this asteroid would be similar to stony iron (4.9 g/cm^3) or ordinary chondritic meteorites (3.6 g/cm^3) and the bulk density would be between 2 and 5 g/cm^3. The shape model was established by Hudson and Ostro [74] from inversion of radar images. From its shape, this asteroid is considered a contact binary. Scheeres et al. [154] used the empirical formula that relates the Fresnel power-reflection coefficient to a bulk density to estimate (4769) Castalia's bulk density as 2.1 g/cm^3. They explain, "the value 2.1 g/cm^3 corresponds to respective porosity of 60% and 40% for ordinary chondrites and stony irons, the candidate meteorite analogs for S class asteroids like this asteroid."

6.4.10   (6489) Golevka

Radar observations at Goldstone, Evpatoria, and Kashima established a physical model of (6489) Golevka [76]. The asteroid's pole direction was estimated as $\lambda = 202 \pm 5°$, $\beta = -45 \pm 5°$, and its rotation period (sidereal) was obtained as 6.0289 ± 0.0001 hr. The shape is extraordinarily angular with flat sides, sharp edges and corners. They estimated the surface density as no more than 3.7 g/cm^3, while they assumed the uniform bulk density as between 2 and 5 g/cm^3 to investigate (6489) Golevka's dynamical environment.

6.4.11   (8567) 1996 HW1

Magri et al. [100] constructed physical properties of (8567) 1996 HW1 by radar and photometric observations. This asteroid is considered a contact binary because of its highly bifurcated and elongated shape. The rotation period was estimated as 8.76243 ± 0.00004 hr and the poly direction was detected as $\lambda = 281 \pm 5°$, $\beta = -31 \pm 5°$. To investigate the asteroid's dynamical environment, they assumed bulk density of 2.0 g/cm^3 consistent with porosity of 40% of L-chondritic composition of which density is 3.37 g/cm^3.

6.4.12 (10115) 1992SK

Busch et al. [21] investigated (10115) 1992 SK by radar and optical observations. They estimated the rotation period as 7.3182 ± 0.0003 hr. The also obtained $\lambda = 99° \pm 5°$, $\beta = -3° \pm 5°$. With the technique by Magri et al. [99], they obtained a surface bulk density of more or less 2.3 g/cm^3. In addition, the dynamical environment was investigated by assuming a uniform density of 2.3 g/cm^3.

6.4.13 (25143) Itokawa

(25143) Itokawa was observed by Japanese spacecraft Hayabusa in 2005 [48]. The mass, volume, rotation period were estimated as $3.51 \pm 0.105 \times 10^{10}$ kg, $1.84 \pm 0.092 \times 10^7$ m^3, and 12.13 hr, respectively. The bulk density was determined as 1.9 ± 0.13 g/cm^3. The pole direction was estimated as $\lambda = 128.5°$, $\beta = -89.66°$. The shape was established by Gaskell [50].

6.4.14 (29075)1950 DA

Busch et al. [19] used Arecibo and Goldstone radar data and optical lightcurves to determine the shape and spin state. They obtained two different shape models of which material may be nickel-iron or enstatite chondritic composition due to two possible pole directions: $\lambda = 88.6 \pm 5°$, $\beta = 77.7 \pm 5°$ for the prograde model and $\lambda = 187.4 \pm 5°$, $\beta = -89.5 \pm 5°$ for the retrograde model. They also reported that the rotation period, 2.1216 hr, is near the spin limit. From radar albedo of this asteroid, the surface density for the prograde model and that for the retrograde model were obtained as 3.2 g/cm^3 and 2.4 g/cm^3, respectively. On the assumption of zero-cohesion, they also estimated reasonable bulk densities as 3.0 g/cm^3 for the prograde model and as 3.5 g/cm^3 for the retrograde model, respectively. In this study, we investigate the failure mode of both models.

6.4.15 (33342) 1998 WT24

From radar observations at Arecibo and Goldstone, Busch et al. [18] estimated physical properties of (33342) 1998 WT24. The pole direction was obtained as $\lambda = 15 \pm 5°$, $\beta = -22 \pm 5°$,

while the spin period was determined as 3.6970 ± 0.0002 hr. This shape model seems have large basins, which might be formed by impacts. Their shape model, on the other hand, may not be compatible with the lightcurve data by [90]. [18] estimated the bulk density as 3 g/cm^3 from the fact that this asteroid, classified as E-class, may include enstatite achondrite of which bulk density is about 3 g/cm^3. They also concluded that its spin state is affected by a YORP effect and decreases with an average rate of 2×10^{-7} deg/s·yr.

6.4.16   (52760) 1998 ML14

Ostro et al. [116] modeled the shape of (52760) 1998ML14, using asteroid radar imaging data sets with the same approach done by [75]. The shape looks almost spherical, but there are some angular points. The pole direction was estimated as $\alpha = 292°$, $\delta = -31°$, while the rotation period was determined as 14.83 ± 0.15 hr. They assumed the uniform bulk density as 2.5 g/cm^3, which is a S-class object (433) Eros.

6.4.17   (66391) 1999 KW4

Ostro et al. [120] obtained physical properties of (66391) 1999 KW4 by radar observations. This asteroid is a binary system; the primary (Alpha) is oblate, while the secondary (Beta) is elongated. In the current study, we only consider the structure of Alpha. The rotation period was obtained as 2.7645 ± 0.0003 hr, while the pole direction was detected as $\lambda = 326 \pm 3°$, $\beta = -65 \pm 3°$. The total mass and the bulk density were estimated as $2.353 \pm 0.100 \times 10^{12}$ kg and 1.97 ± 0.24 g/cm^3, respectively. They also pointed out that Alpha's porosity is about 50% and its oblate shape has an equatorial ridge at the object's potential-energy minimum.

6.4.18   (136617) 1994 CC

This asteroid is a triple system. Similar to (66391) 1999 KW4, we only investigate Alpha here. [47] estimated the mass by radar observations at Arecibo and Goldstone as $2.5935 \pm 0.1 \times 10^{10}$ kg (Alpha). Brozovic et al. [15] used radar, photometric, and spectroscopic observations to determine

(136617) 1994 CC's physical properties. Using the [47] mass and their size estimation, they obtained a bulk density of 2.1 ± 0.6 g/cm^3. Also, they obtained the pole direction as $\lambda = 336°$, $\beta = 22°$ consistent with [47]. The rotation period was given as 2.38860 ± 0.00009 hr.

6.4.19   2002 CE26

Radar observations by Shepard et al. [167] revealed that 2002 CE26 is a binary system. The primary, 3.5 ± 0.4 km in diameter, spins with a synodic period of 3.2931 ± 0.0003 hr. The pole direction is $\lambda = 317°$, $\beta = -20°$. The primary mass is $1.95 \pm 0.25 \times 10^{13}$ kg, and the bulk density is estimated as $0.9 + 0.5/ - 0.4$ g/cm^3.

6.4.20   2008 EV5

2008 EV5 was observed by Busch et al. [20]. The pole direction was determined as $\lambda = 180 \pm 10°$, $\beta = -84 \pm 10°$, while the rotation period was given as 3.725 ± 0.001 hr. The size is ~ 150 meter in diameter. The volume estimation was 0.035 km$^3 \pm 40\%$. Based on methods by Magri et al. [99], they reported that the maximal near-surface bulk density is 3.0 ± 1.0 g/cm^3. The shape includes an impact crater around the ridge. The equatorial ridge observed implies that this body may experience a YORP spin-up that reconfigures the shape.

6.5   Analysis for the failure modes of real shapes

6.5.1   Methods

We review the physical parameters used in this investigation. Here, we keep using dimensionless values. Ω_t^* and Ω_p^* are the spin rates at structural failure of the entire volume and the partial volume, respectively. Those parameters are given by Eq.(6.3). We also define Ω_t^* as the effective shape, which can be compared with $\Omega_{sph}^* = 1.07$ (a sphere case). Ω_a^* is the spin rate at which $\bar{T}_{11}^a$ becomes zero-tension somewhere except for the edges first. This can be computed by Eq.(6.5). $\Omega^\diamond$ is the spin rate at which surface shedding occurs first, which can be given by Eq.(6.4). We will also calculate the spin rate at which the minimal friction angle of the entire volume flips over, i.e., $\Omega_t^\odot$.

ϕ_t^* and ϕ_p^* are the minimal friction angles of structural failure of the entire volume and the partial volume, which can be obtained from Eq.(6.2). Also, we assume that the material friction angle ϕ_F is 40°.

This chapter computes those parameters to characterize asteroids by the failure modes. To do so, we propose a shape classification due to the failure modes. This classification allows us to understand how asteroids fails by a YORP-type spin-up. We give the definition of the classification in the next section.

6.5.2   Shape Classification

We categorize the 21 sample shapes by a two-alphabetic classification. The first letter describes bodies' shape by 'S', 'E', and 'B', which stand for 'spherical', 'ellipsoidal', and 'bifurcated', respectively. To classify the shape into these types, we use Ω_t^* and Ω_a^*. A bifurcated body is determined first. Let us assume $\bar{T}_{11}^a(x) = 0$. The shape is classed as 'B' if, for a small quantity $\epsilon > 0$, there is another quantity $\delta > 0$ such that $\bar{T}_{11}^a(x \pm \epsilon) < -\delta < 0$ at Ω_a^*. This statement is equivalent to the condition where $\bar{T}_{11}^a$ through the location of cross sections has a peak of the zero-tension, not at the edges, at Ω_a^*. This occurs when a body has a bifurcated shape. Note that this condition is not the condition of structural failure, so we will use the partial volume stress to determine the accurate conditions.

If the shape is not classed as 'B', then we go to the next step to determine it as either 'S' or 'E'. If $0.97 \leq \Omega_t^* \leq 1.07$, we characterize it as 'S'. On the other hand, if Ω_t^* is not in that region, an object is considered elongated, so it is denoted as 'E'. The threshold between 'S' and 'E', i.e., 0.97, is defined so that a range of 10% from Ω_{sph}^* is involved in the spherical shape.

The second letter indicates the failure modes: 'S' for surface shedding and 'F' for structural failure. We use different definitions between a bifurcated shape and other shapes. For 'S' or 'E' type, if $\Omega_t^* < \Omega^\diamond$, then structural failure occurs first, so the letter is 'F'; otherwise, the body deforms by surface shedding, so the letter is 'S'. On the other hand, if the first letter is 'B', the failure modes are determined by the following condition. If $\min(\Omega_p^*) < \Omega^\diamond$, then the body should

reshape by structural failure, so the shape is classified as 'F; otherwise, it should be 'S'. Note that for a uniformly rotating ellipsoid, structural failure of any body part is identical to that of the whole body; on the other hand, a bifurcated body deforms at its neck, so the neck part reaches failure earlier than the whole body. For this reason, different classifications comes from different structural failure conditions.

We show a few examples for the classification. Let us assume that some asteroids are classified as SS. This classification means that these asteroids' shape is spherical, i.e., $0.97 \leq \Omega_t^* \leq 1.07$, and surface shedding occurs first, i.e., $\Omega_t^* \geq \Omega^\diamond$. On the other hand, if an asteroid is classified as BF, the shape is bifurcated and structural failure occurs first, i.e., $\min(\Omega_p^*) < \Omega^\diamond$.

6.5.3   Results

Table 6.2 summarizes the spin limits. Ω_{min} and Ω_{max} are the minimal and maximal current spin rates, respectively, given by the density uncertainty of each asteroid. $\hat{\rho}^\dagger$ is the lowest density for which a body is stable and holds its original shape. For the shape classification, all the asteroids are involved in four categories: ES, SF, EF, and BF. We note that we do not find the classes SS and BS. Examples for these types are described in Fig.6.3.

6.5.3.1   Type ES

Objects of this type are elongated and the first failure mode is surface shedding. (1620) Geographos, (2100) Ra-Shalom, (4660) Nereus, (6489) Golevka, and (10115) 1992 SK are categorized as this type.

First, Fig.6.4 shows $\bar{T}_{11}^a$ for these objects at Ω_t^*. The stress (vertical axis) is normalized by the definition given in Section 6.3 and the location of cross sections (horizontal axis) is also described by a dimensionless value that the body edges are adjusted to ± 1[1] . For surface shedding, $\bar{T}_{11}^a$ at either of the edges should be above the zero-stress condition at Ω_t^*. All bodies experience tension

---

[1] Because of our discretization method, ± 1 does not always correspond to the body edges perfectly. Therefore, the area average $\bar{\sigma}_a^*$ at ± 1 is not zero. However, our computation satisfies the zero surface traction condition and this can be seen if ± 1 matches the edges perfectly.

on either side, so they should be shed at Ω_t^*. (1620) Geographos has a peak around the right edge, but not exactly at that point. This implies that surface shedding occurs relatively earlier than Ω_t^*. (2100) Ra-Shalom also seems to be able to experience surface shedding on the right side; however, compared to (1620) Geographos, the location of material shedding is at the very end of the body. For (6489) Golevka, since $\bar{T}_{11}^a$ at the left side is above the zero-stress condition, surface materials may be shed at this location, which is opposite to other bodies. For (10115) 1992SK, $\bar{T}_{11}^a$ reaches zero-tension in an area at the right edge.

Second, Fig.6.5 describes ϕ_t^* with respect to Ω. The black dashed line shows $\phi_F = 40°$. As seen in the analysis for an ellipsoid, for each object, there is $\Omega_t^{\odot}$ such that the curve is separated into Regions 1 and 2. Note that as ϕ_F becomes smaller, Ω_t^* decreases. Therefore, we can say that ES type transits to EF type, depending on ϕ_F.

6.5.3.2 Type SF

This type includes (29075) 1950 DA (prograde), (52760) 1998 ML14, (66391) 1999 KW4, (136617) 1994 CC, 2002 CE26, and 2008 EV5. This spherical and non-bifurcated type experiences structural failure first.

Figure 6.6 shows $\bar{T}_{11}^a$ at Ω_t^* for these objects. It is below zero-stress at all the locations and the most compressive part is around the middle. This result is consistent with the result for a sphere. Since they are spherical, those normalized stresses are almost the same. Note that $\bar{T}_{11}^a$ is below zero-tension, but this does not mean that it is below the structural failure condition.

ϕ_t^* is described in Fig.6.7. The type relaxes more than ES type. Since Region 2 extends to a wider region, Ω_t^* almost reaches $\Omega_{sph}^* = 1.07$ and $\Omega_t^{\odot}$ moves to a lower value. For (29075) 1950 DA (prograde), (136617) 1994 CC, and (52760) 1998 ML14, ϕ_t^* around $\Omega_t^{\odot}$ is nearly zero, so it is difficult to detect $\Omega_t^{\odot}$ correctly. Therefore, in Table 6.2, we describe such cases as ≤ 0.20 to mean that their shape can be considered close to be a perfect sphere. Consequently, it is found that for this type, structural failure for a whole body may occur before surface shedding.

6.5.3.3   Type EF

Type EF is similar to Type SF, but is different in terms of the shape that is more elongated than Type SF. This type includes (1580) Betulia, (4660) Nereus, (29075) 1950 DA (retrograde), and (33342) 1998 WT24. The area stress for this type looks like that for Type SF, but the elongation causes it to become less compressive (see Fig.6.8). Eq.(6.32) indicates that the area stress is a function of A_1; it becomes close to zero as A_1 decreases.

ϕ_t^* is more constrained than that of Type SF. In Region 1, ϕ_t^* becomes larger than that of Type SF when Ω is not close to $\Omega_t^{\odot}$. In Region 2, the slope has a higher inclination, so Ω_t^* shifts to a lower value. On the contrary, (33342) 1998 WT24 has some similar trends of Type SF; therefore, this object may be considered somewhat between SF and EF.

6.5.3.4   Type BF

Type BF is an elongated and bifurcated object that may experience structural failure first. This type includes (243) Ida, (433) Eros, (8567) 1996 HW1, (2063) Bacchus, (4179) Toutatis, (4769) Castalia, and (25143) Itokawa.

Figure 6.10 shows $\bar{T}_{11}^a$ of each object. The stress of this type includes a peak around the middle, consistent with the location of its bifurcation. The peak highly depends on a body's rotation. It does not appear at a low spin rate, but becomes sharp as the spin rate increases. Among the BF objets, the peak of (8567) 1996 HW1 is above zero-tension, so it experiences strong tension at Ω_t^*. (243) Ida, (25143) Itokawa, and (4179) Toutatis have similar trends as well. On the other hand, (433) Eros, (2063) Bacchus, and (4769) Castalia have relatively weak peaks, which are below zero-tension, but the peaks are noticeable.

Figure 6.11 indicates ϕ_t^* and ϕ_p^*. The solid lines are for ϕ_t^*, while the dashed lines are for ϕ_p^*. ϕ_t^* of this type looks similar to that of Type EF, while ϕ_p^* is more constrained than ϕ_t^*. To enhance the effect of their bifurcation, we choose a slice so that its mean point corresponds to the peak location and the width is 8% of the body maximal length. For all objects, Ω_p^* is less than Ω_t^*

(Table 6.2). It implies that their bifurcation part fails earlier than the whole volume. Specifically, (4179) Toutatis, (8567) 1996 HW1, and (25143) Itokawa significantly depend on the condition of the neck part because Ω_p^* is much smaller than Ω_t^*. For all but (4769) Castalia, it is found that

$$\phi_p^* > \phi_t^*. \tag{6.36}$$

The difference between ϕ_t^* and ϕ_p^* can be more noticeable when an asteroid has a strong bifurcation. Therefore, asteroids that have a large difference of these angles, such as (8567) 1996 HW1 and (25143) Itokawa, have a strong bifurcation. On the other hand, other asteroids such as (2063) Bacchus have a weak bifurcation.
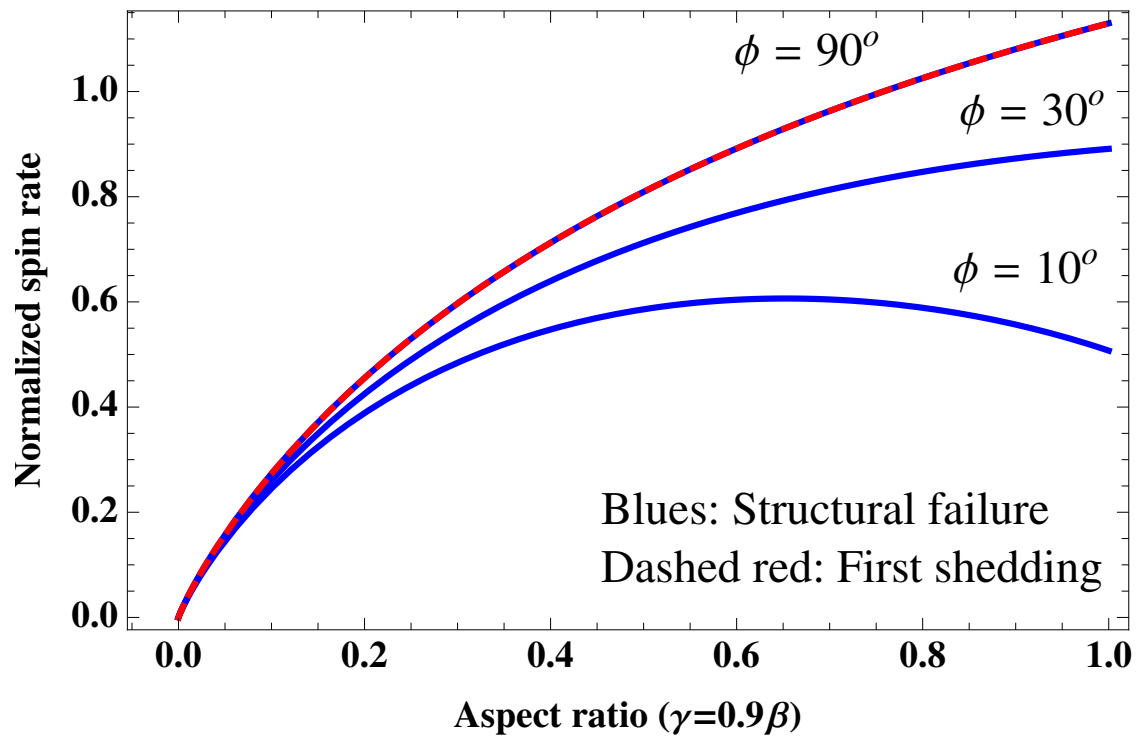
(a)
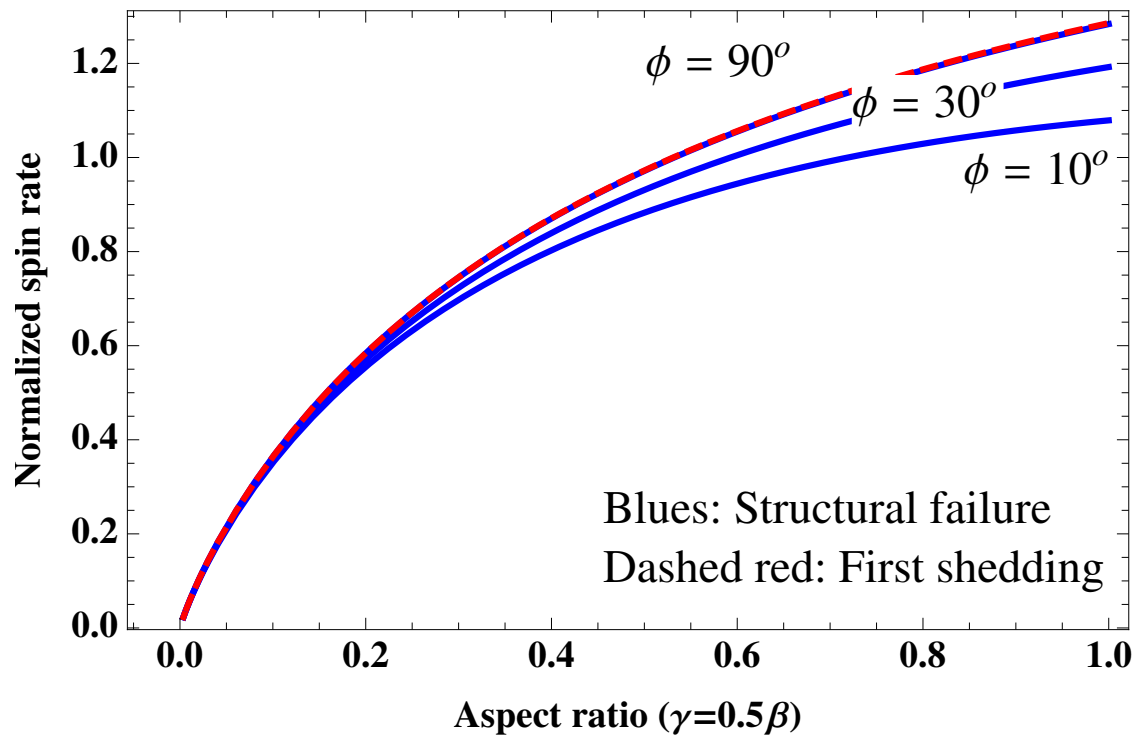
(b)

Figure 6.2: Limit spins (see [63]) and the first shedding. The former is given by the blue lines, while the latter is shown by the dashed red line. The limit spin is obtained by Eq.(6.21), which is identical to Case 6 defined by Holsapple [63]. Here, we only show the results of tension. It is found that the first shedding is equivalent to structural failure of an ellipsoid with $\phi = 90°$.

(a)

(b)

(c)

(d)
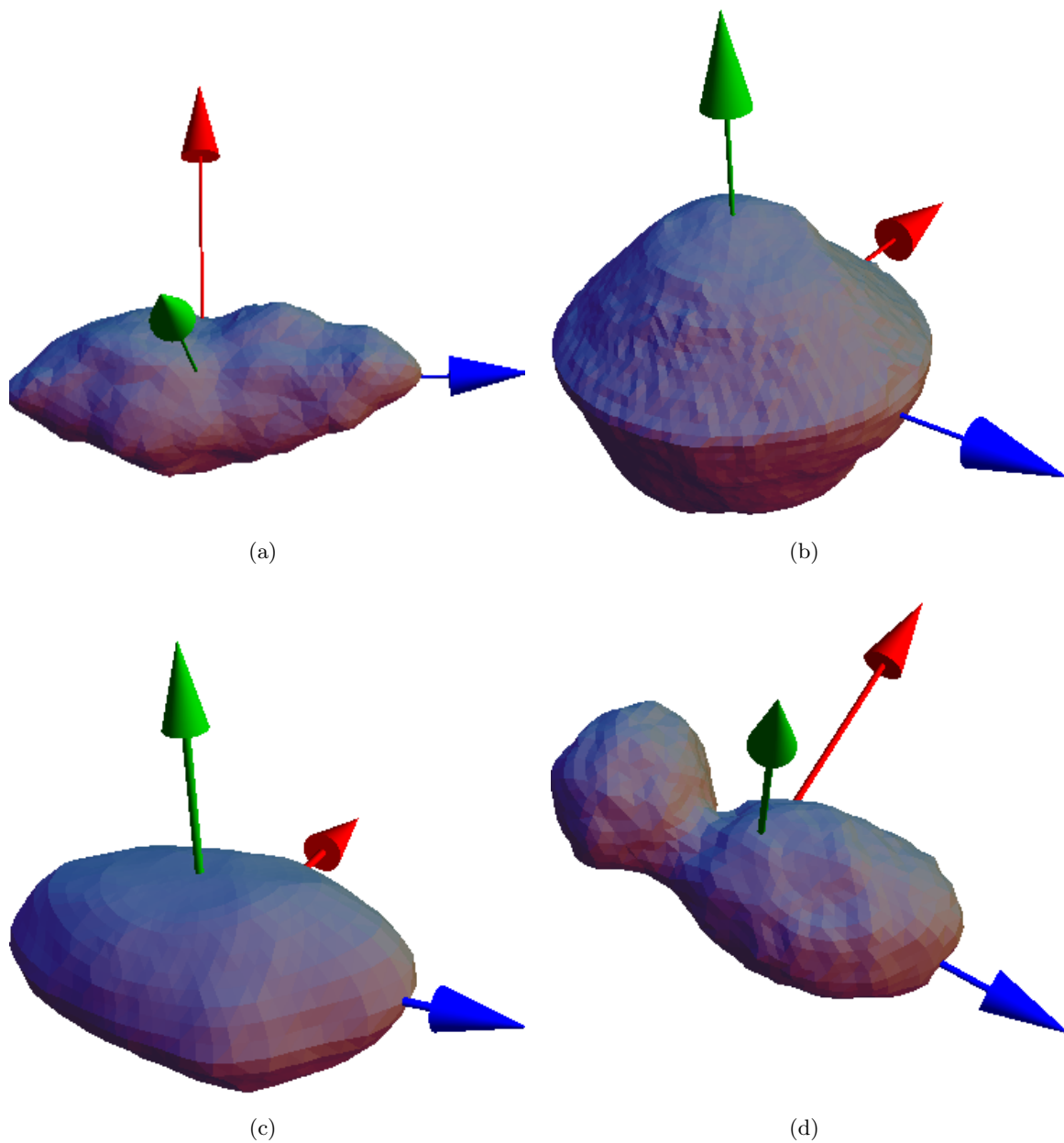
Figure 6.3: Shape classification. The blue, red, and green arrows are for the minimal, intermediate, and maximal principal axes, respectively. 6.3(a) is (1620) Geographos, Type ES; 6.3(b) is (66391) 1999 KW4, Type SF; 6.3(c) is (4660) Nereus, Type EF; and 6.3(d) is (8567) 1996 HW1, Type BF.
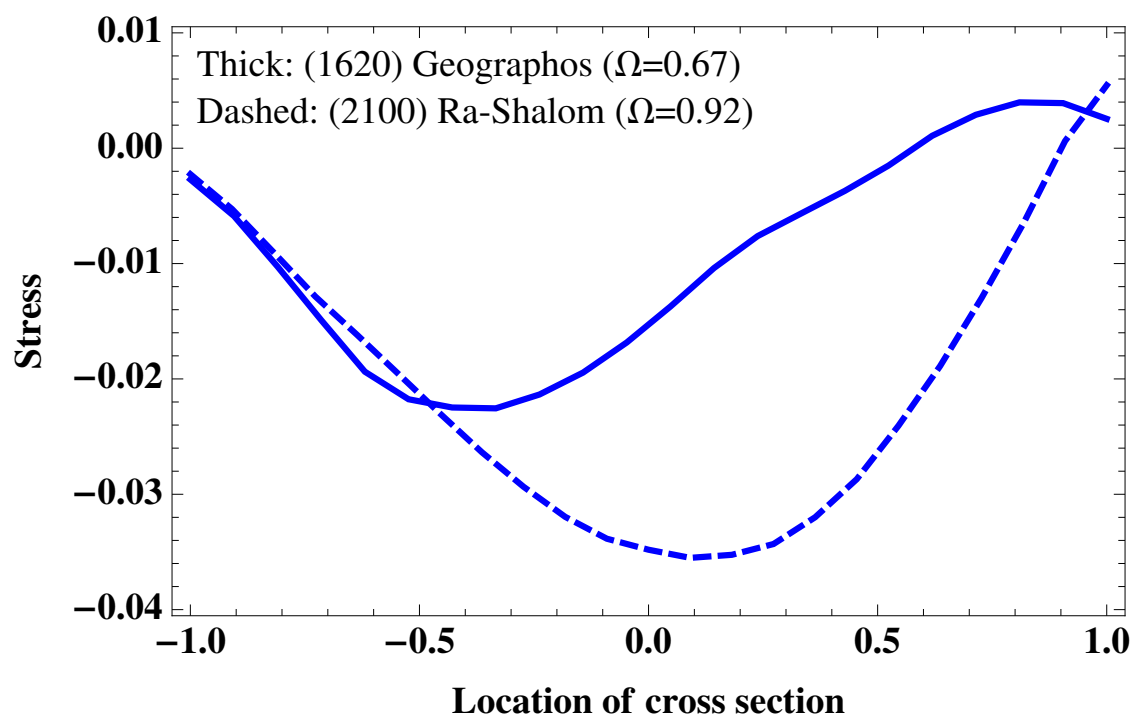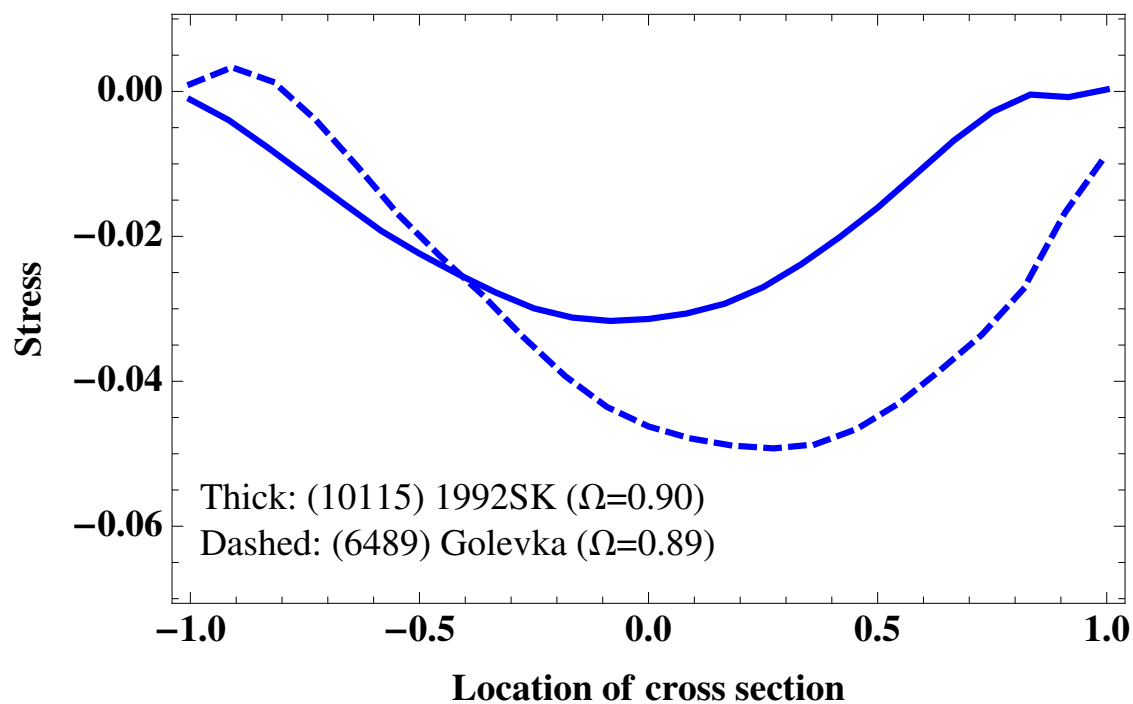
Figure 6.4: Area stress for Type ES at Ω_t^*.
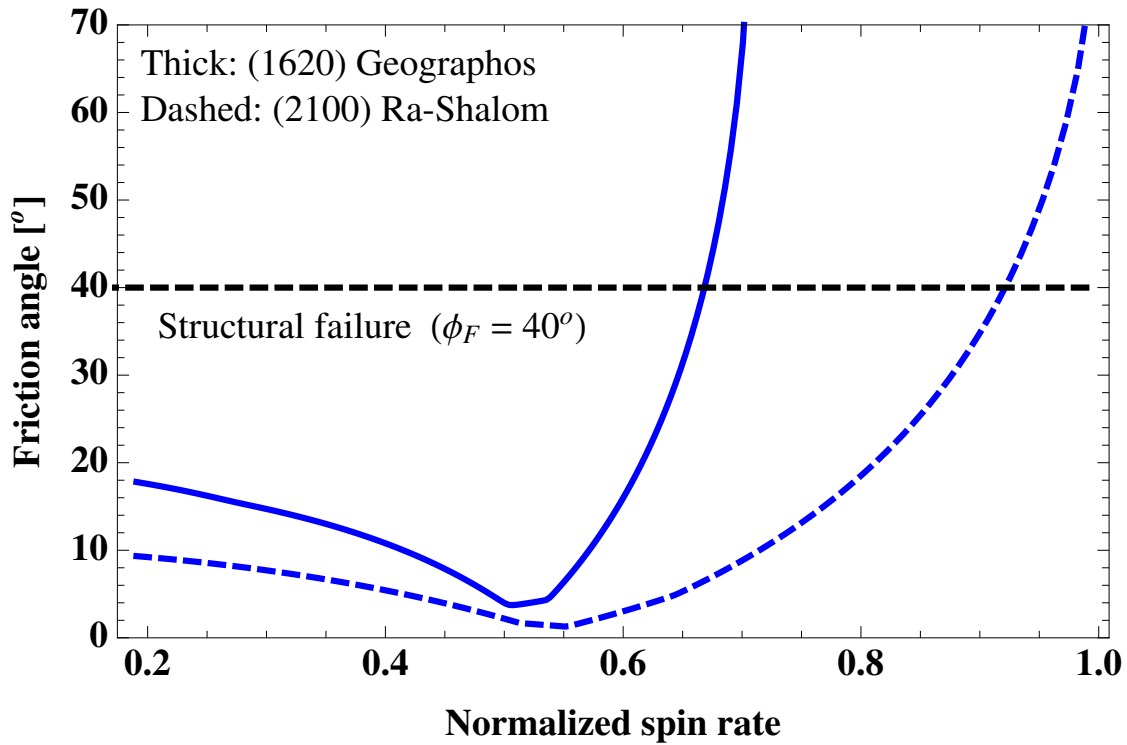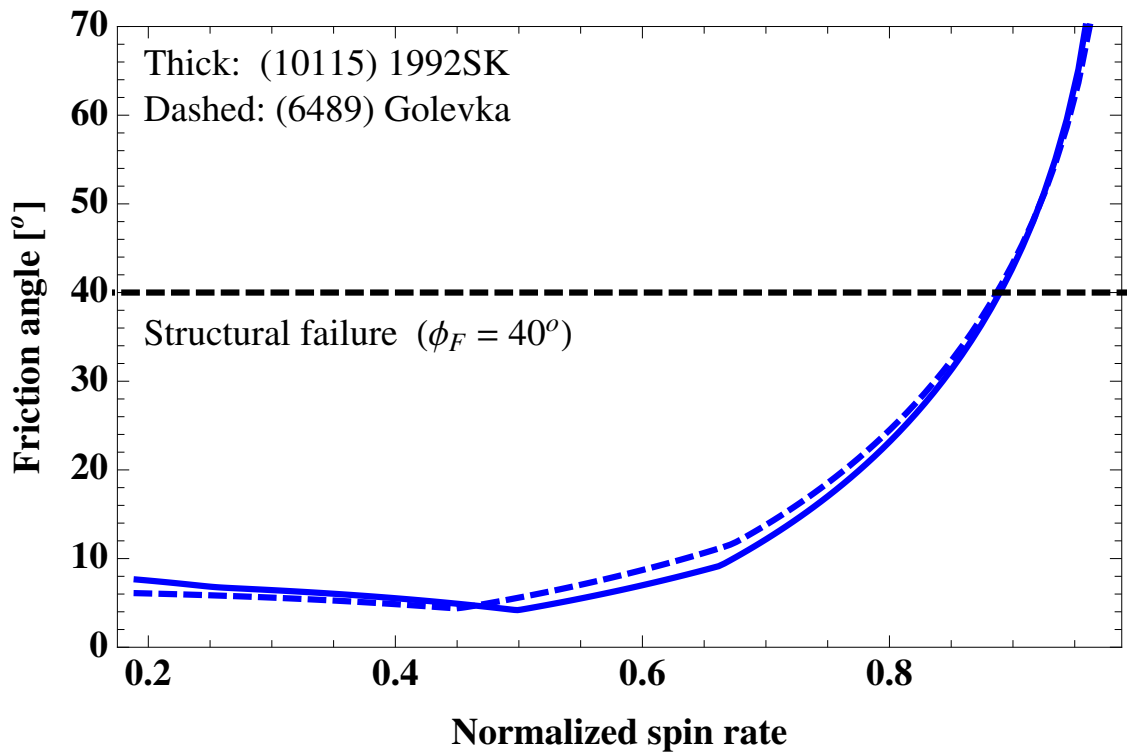
Figure 6.5: Type ES. Minimal friction angles associated with the total volume stress.
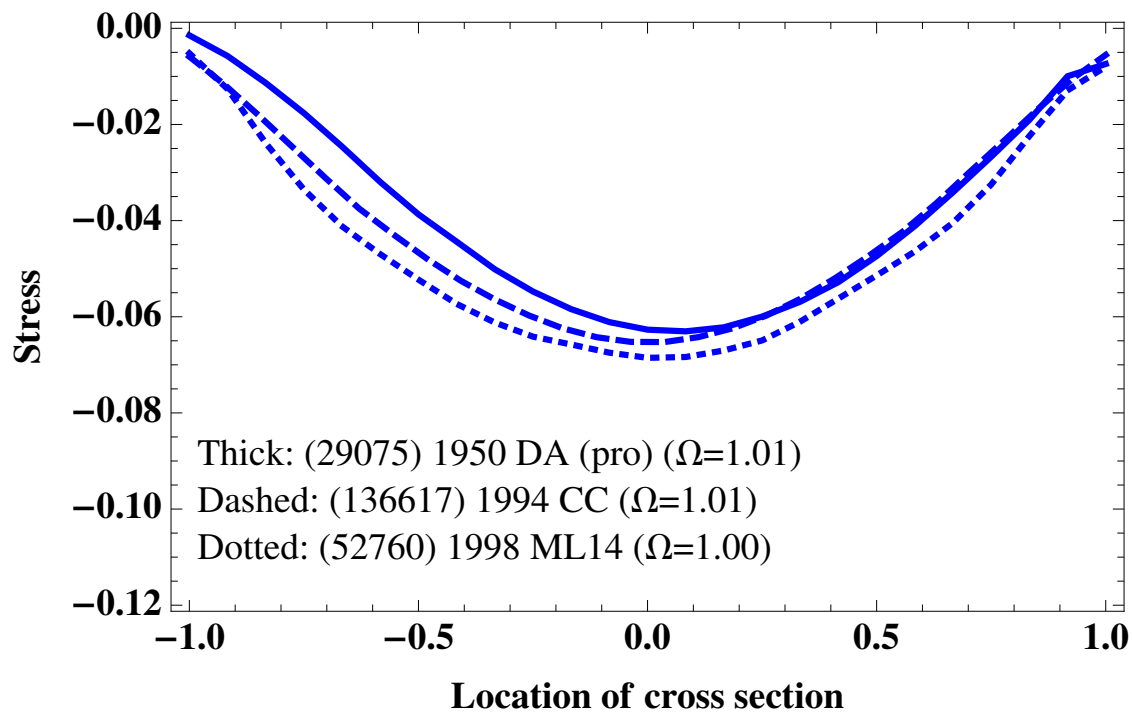
(a)
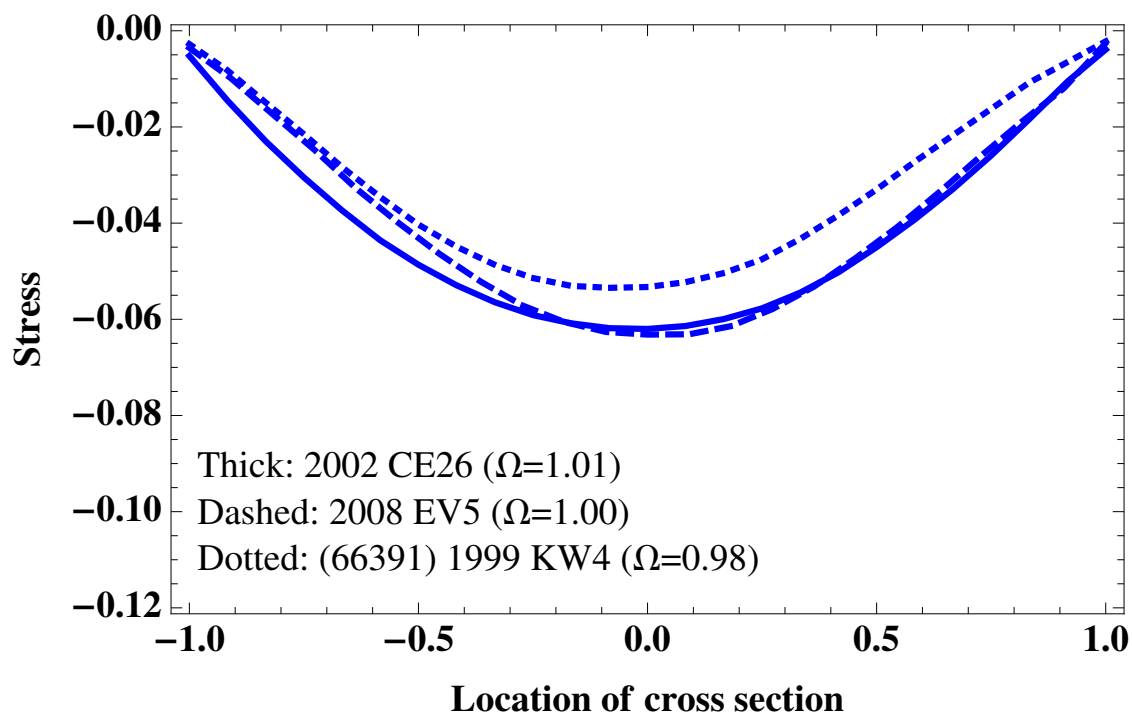
(b)

Figure 6.6: Area stress of Type SF at Ω_t^*.
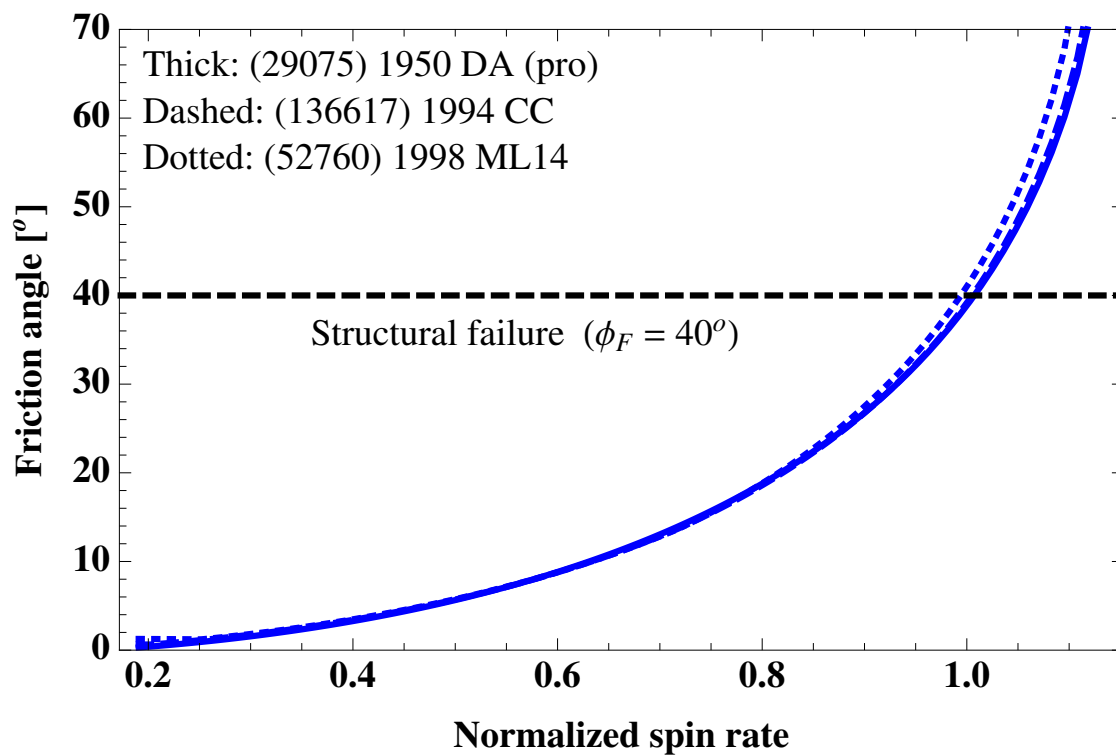
(a)
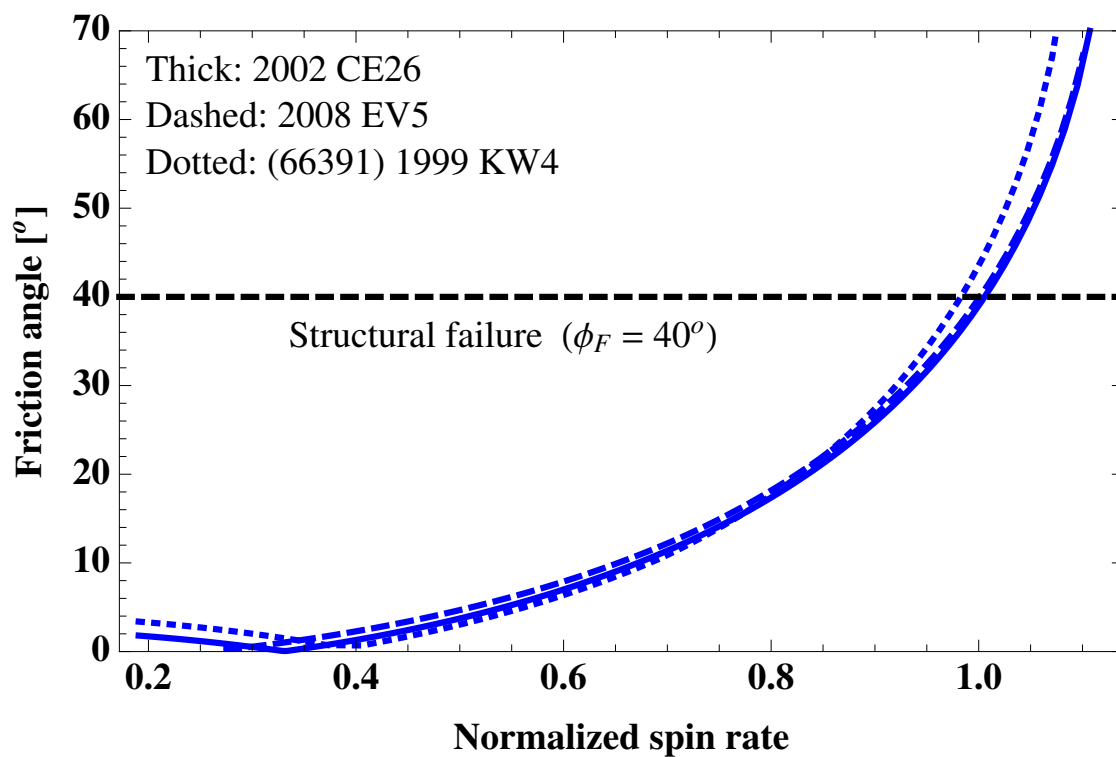
(b)

Figure 6.7: Type SF. Minimal friction angles associated with the total volume stress.
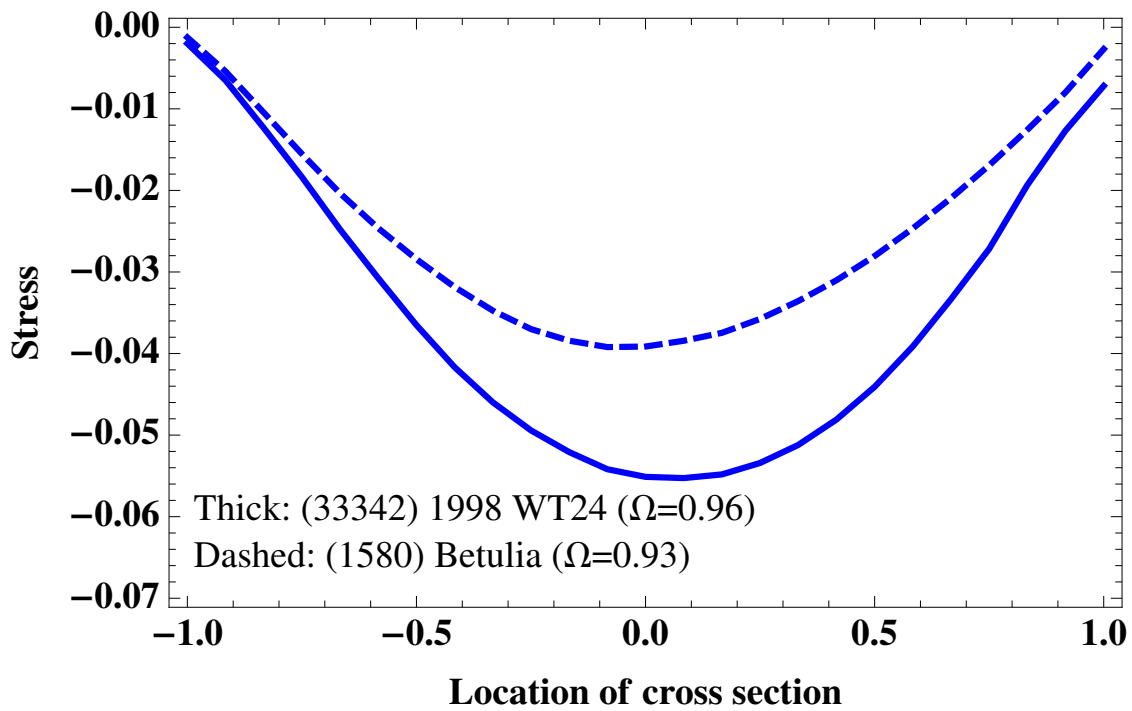
(a)
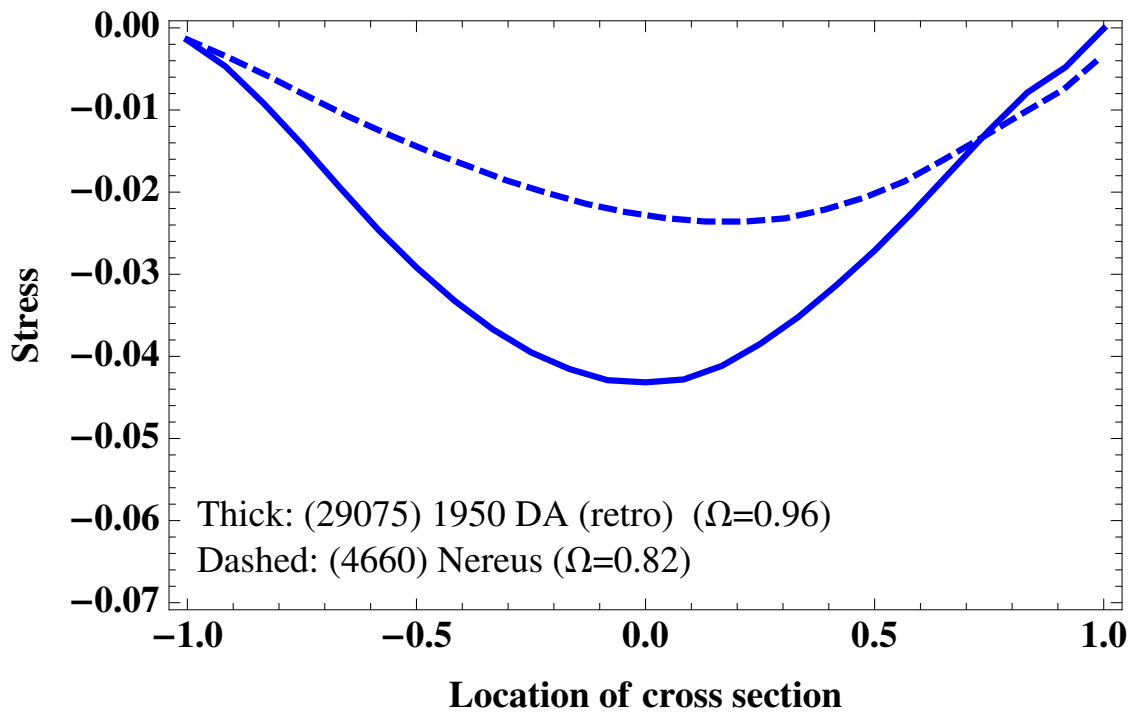
(b)

Figure 6.8: Area averaged stress for Type EF at Ω_t^*.
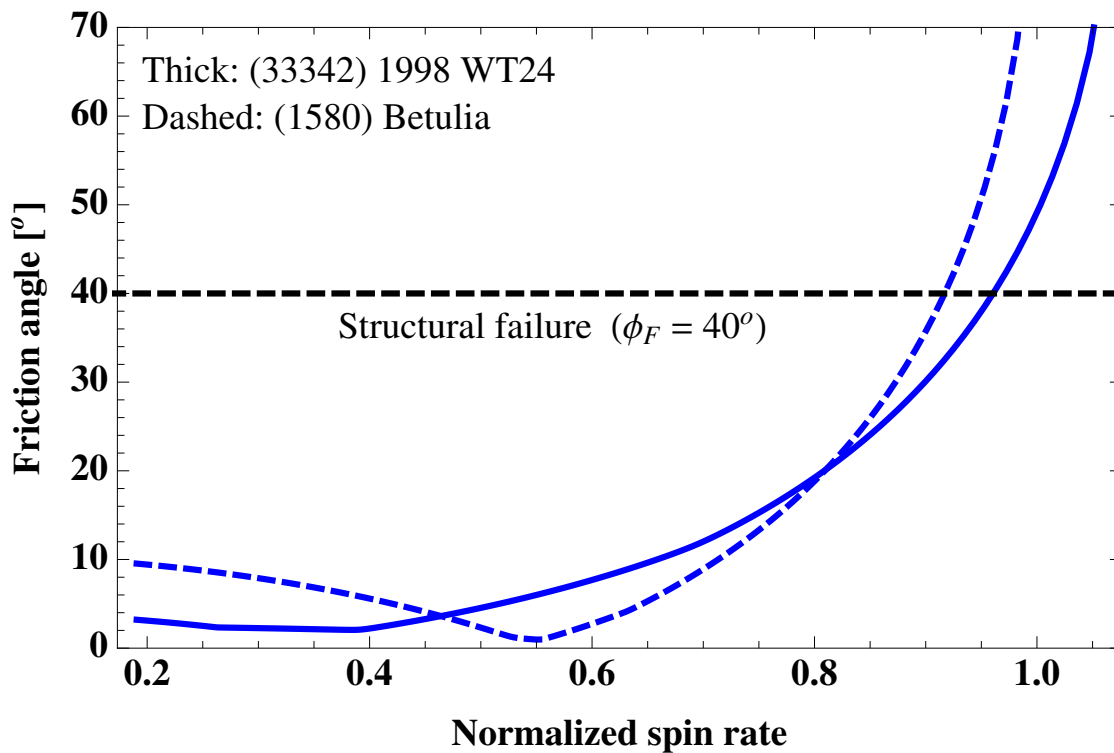
(a)
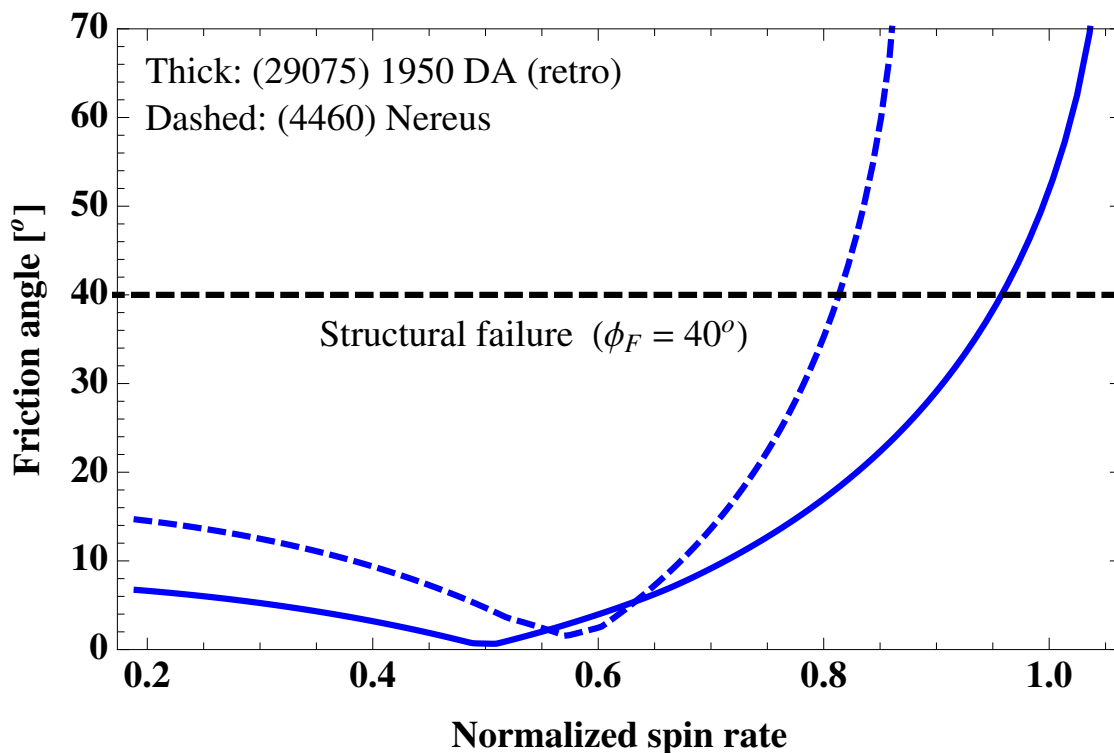
(b)

Figure 6.9: Type EF. Minimal friction angles associated with the total volume stress.
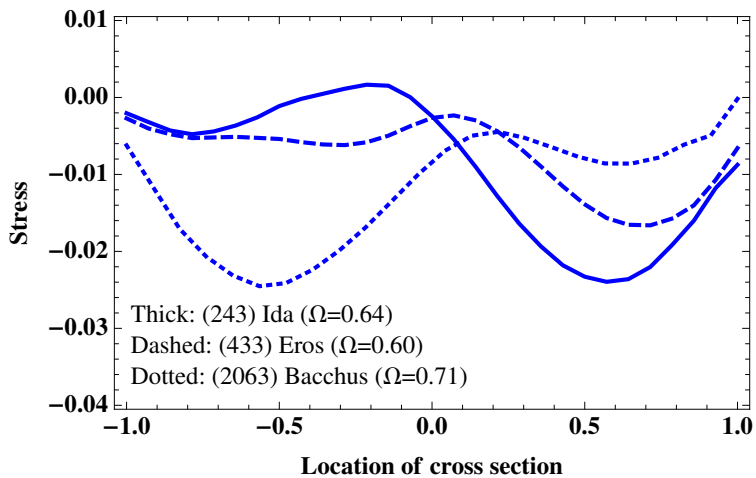
(a)
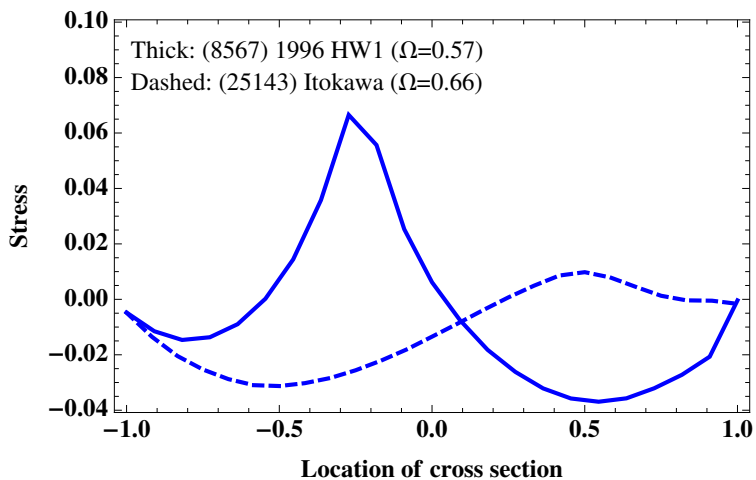
(b)
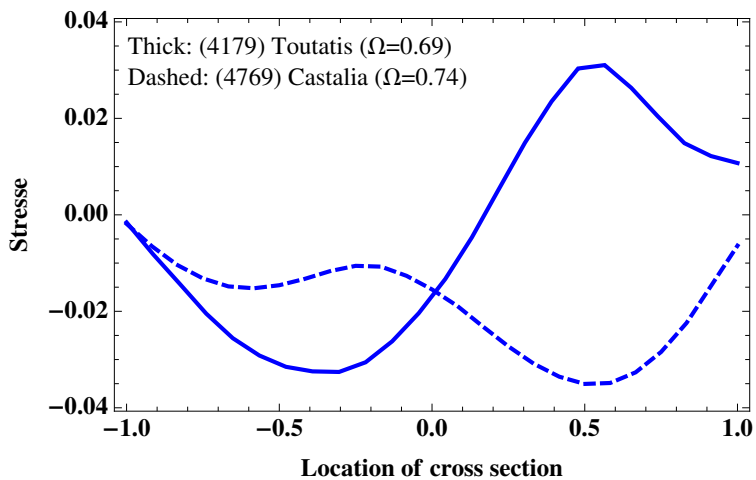
(c)

Figure 6.10: Area stress of Type BF at Ω_t^*.
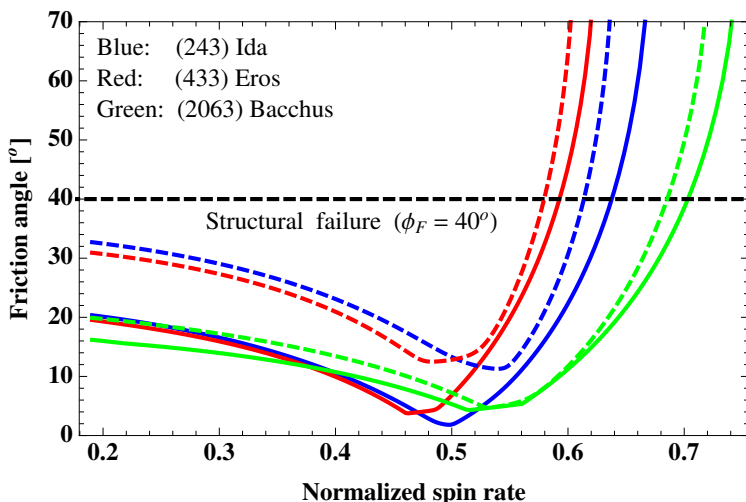
(a)
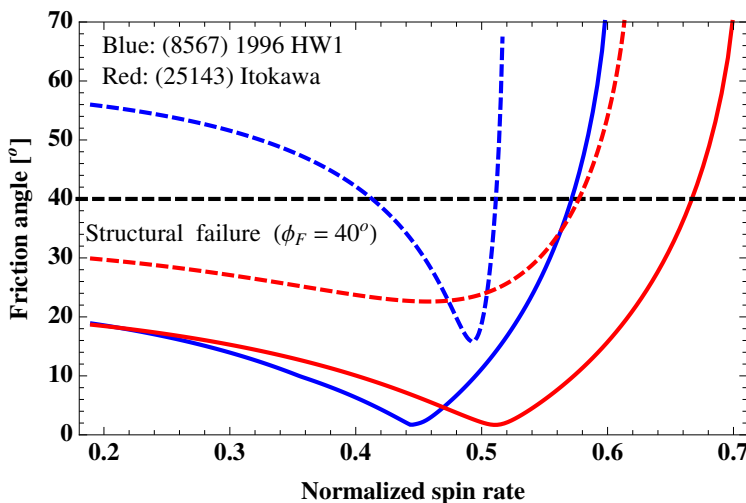
(b)
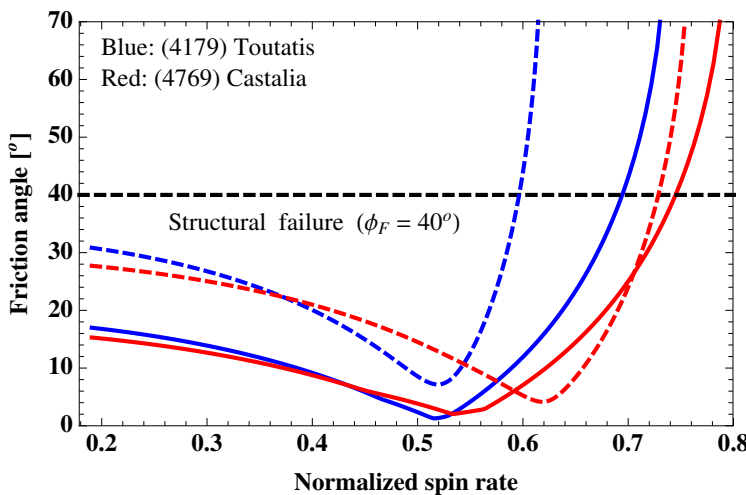
(c)

Figure 6.11: Type BF. Minimal friction angles associated with the total volume stress (solid) and that associated with the partial volume stress (dashed).

6.6   Discussion

6.6.1   Ellipsoid and Real Shapes

Section 6.5 showed that the stress configurations of real shapes are different from those of ellipsoids. These real shapes are classified according to their shape configurations and failure modes. Here, based on these results, we summarize the difference between ellipsoids and real shapes.

First, let us discuss structural failure of a partial volume and a total volume. We introduced the partial and total volume stresses to determine the minimal friction angles for a partial volume and a total volume, respectively. For ellipsoids, structural failure of these averages is identical because any place in an ellipsoid reaches yield at the same time; therefore, we have $\phi_t^* = \phi_p^*$ and $\Omega_t^* = \Omega_p^*$ (see Eq.(6.30) and (6.31)). On the other hand, real shapes do not have those equivalent relations. ϕ_p^* and Ω_p^* depend on the location of a slice. For example, let us consider a bifurcated body. If a narrow region is chosen as a slice, ϕ_p^* and Ω_p^* are constrained more than ϕ_t^* and ϕ_p^*, respectively. On the other hand, if a wider region is selected, the partial volume relaxes more than the total volume. Since we chose narrower regions of Type BF on purpose, the partial volume should be constrained (see Fig.6.11). We have to note the case of (4769) Castalia. There is a region where $\phi_p^* < \phi_t$ when $0.6 \leq \Omega \leq 0.7$. This comes from several reasons. The first is that since (4769) Castalia's bifurcation part is twisted and lies in a small region, our experimental part may include not only the bifurcation part but also some wider region. The second results from the simplification for computing the partial volume stress.

Second, the area stress $\bar{T}_{11}^a$ of real shape is different from that of ellipsoids. For ellipsoids, as shown in Eq.(6.32), the area stress can be described as a quadratic form, so the stress along the minimal principal axis is minimum at the middle and becomes zero at the extremities. On the other hand, for real shapes, the stress configuration does not look like that of ellipsoids. For Type ES, bodies reach tension near the extremities, but experience compression in other regions. For Type BF, there is a cross section experiencing a stress peak. This section usually appears around a bifurcation region.

Table 6.2: Results for surface shedding, total structural failure, and partial structural failure. The following quantities are listed: Ω_{min} and Ω_{max}, the minimal and maximal spin rates across the reported density uncertainty, respectively; $\Omega^{\diamond}$, the spin condition of surface shedding; Ω_t^*, the spin rate at structural failure of a total volume; $\Omega_t^{\odot}$, the spin rate at $\phi_t^* = 0$; Ω_a^*, the spin rate at $\bar{T}_{11}^a(x) = 0$; Ω_p^*, the spin rate at structural failure of a partial volume; and $\hat{\rho}^{\dagger}$, the minmal density to keep the original shape.

Asteroid system	Ω_{min}	Ω_{max}	$\Omega^{\diamond}$	Ω_t^*	$\Omega_t^{\odot}$	Ω_a^*	Ω_p^*	$\hat{\rho}^{\dagger}$	Shape type
(1620) Geographos	0.37	0.73	0.64	0.67	0.50	0.64	-	1.3	ES
(2100) Ra-Shalom	0.096	0.19	0.91	0.92	0.55	0.92	-	-	ES
(6489) Golevka	0.32	0.63	0.85	0.89	0.43	0.87	-	-	ES
(10115) 1992 SK	0.26	0.52	0.85	0.90	0.50	0.91	-	-	ES
(29075) 1950 DA (prograde)	0.90	1.80	1.07	1.01	≤ 0.20	1.08	-	3.2	SF
(52760) 1998 ML14	0.13	0.25	1.02	1.00	0.25	1.11	-	-	SF
(66391) 1999 KW4 (Alpha)	0.93	1.05	1.04	0.98	0.40	1.06	-	2.0	SF
(136617) 1994 CC (Alpha)	0.89	1.13	1.06	1.01	≤ 0.20	1.10	-	2.5	SF
2002 CE26 (Alpha)	1.02	1.64	1.08	1.01	0.33	1.11	-	1.3	SF
2008 EV5	0.51	1.02	1.02	1.00	0.28	1.09	-	1.1	SF
(1580) Betulia	0.31	0.62	0.94	0.92	0.56	0.98	-	-	EF
(4660) Nereus	0.13	0.25	0.84	0.82	0.58	0.85	-	-	EF
(29075) 1950 DA (retrograde)	0.90	1.80	0.96	0.96	0.45	1.02	-	3.5	EF
(33342) 1998 WT24	0.52	1.03	1.03	0.96	0.40	1.04	-	1.2	EF
(243) Ida	0.47	0.57	0.69	0.64	0.50	0.64	0.62	-	BF
(433) Eros	0.44	0.45	0.82	0.60	0.46	0.60	0.58	-	BF
(4179) Toutatis	0.020	0.041	0.64	0.69	0.52	0.63	0.60	-	BF
(4769) Castalia	0.47	0.93	0.83	0.74	0.54	0.76	0.72	-	BF
(2063) Bacchus	0.13	0.26	0.73	0.71	0.52	0.71	0.68	-	BF
(8567) 1996 HW1	0.22	0.44	0.72	0.57	0.45	0.52	0.42-0.51	0.7-1.1*	BF
(25143) Itokawa	0.22	0.24	0.73	0.66	0.51	0.64	0.58	-	BF

* For (8567) 1996 HW1, as seen in Fig.6.11(b), since Ω is bounded at both lower and upper limits, $\hat{\rho}^{\dagger}$ is described as the minimal and maximal densities.

Next, the minimal friction angle causing the first shedding condition before structural failure depends on shapes. For ellipsoids, the first shedding condition is equivalent to structural failure of the total volume with a friction angle of 90°. In such a case, materials should be resistant to shear stress; in other words, a yield condition becomes a simple no-tension criterion. Natural soils, however, have no such feature; therefore, an ellipsoid never experience surface shedding. On the other hand, real shapes do not necessarily have a friction angle of 90° to experience the first shedding. Our study shows that the first shedding for the ES objects occurs even when the friction angle is 40°. This difference comes from the fact that since those asteroids are more elongated and sharper than perfect ellipsoids, the centrifugal force can overcome the gravity attraction more easily.

6.6.2   Current Rotation and Bulk Density

This section discusses constraints on the bulk density of real shapes. Some asteroids shown in this chapter experience a relatively high spin and may be close to failure modes. We compare the current spin state ranging from Ω_{min} to Ω_{max} with the spin limit, i.e., $\min(\Omega^{\diamond}, \Omega_t^*, \Omega_p^*)$. Asteroids constrained by the current configurations are: (1620) Geographos from Type ES; (29075) 1950 DA (prograde), (66391) 1999 KW4, (136617) 1994 CC, 2002 CE26, and 2008 EV5 from Type SF; (29075) 1950 DA (retrograde) and (33342) 1998 WT24 from Type EF; (8567) 1996 HW1 from Type BF. In Table 6.2, we show the minimal bulk density $\hat{\rho}^{\dagger}$ given from constraints by the current configuration. If the actual density is smaller than $\hat{\rho}^{\dagger}$, a body cannot hold the original shape any longer.

The density of (1620) Geographos, an ES type asteroid, is constrained by the relation $\Omega^{\diamond} = 0.64 < \Omega_{max} = 0.73$. This allows us to determine the lower bound of the bulk density. From the definition of Ω, we obtain the minimal density as 1.3 g/cm^3. Ostro et al. [118] estimated the surface density as 2 to 3 g/cm^3. Due to a compaction effect, interior bulk density is usually larger than surface bulk density; therefore, we can consider that this constraint is consistent with their conclusion. Again, we assume the uniform density distribution.

SF asteroids, (29075) 1950 DA (prograde), (66391) 1999 KW4, (136617) 1994 CC, 2002 CE26, and 2008 EV5, experience a fast spin almost near their spin limit. Unlike Type ES, those asteroids fail by structural failure. Ω_t^* of these asteroids are below their Ω_{max}. Our result for 2002 CE26 shows that the minimal bulk density obtained here is almost the upper bound of the estimation by Shepard et al. [167], i.e., 1.4 g/cm^3. Similarly, the minimal bulk density of (29075) 1950 DA (prograde) is 3.2 g/cm^3, which is slightly larger than the estimation 3.0 g/cm^3 by [19] who consider a zero-material strength condition.

EF asteroid, (33342) 1998 WT24 and (29075) 1950 DA (retrograde), are also constrained by the current configuration. For both cases, our results correspond to the previous estimations by Busch et al. [18] and by Busch et al. [19], respectively

The most interesting asteroid is (8567) 1996 HW1, a BF type asteroid. This highly bifurcated body is sensitive to structural failure at the neck. Comparing Ω_p^* with the current spin state, we estimate the lower and upper bounds as 0.7 and 1.1 g/cm^3, respectively. Unlike other bodies, which only have the lower bound, the bulk density of this asteroid is bound on both sides. If the stress state violates this small constraint, then structural failure should start from the neck. Note that if we choose a small friction angle as ϕ_F, then the range of the bulk density given here becomes smaller!

6.7   Conclusion

We investigated two failure modes of asteroids due to a YORP-type spin acceleration: surface shedding and structural failure. The method in this chapter searched for the first shedding condition by tracking the dynamical equilibrium points. On the other hand, we used limit analysis to determine the upper bound for structural failure of a partial volume and a total volume. Our prime result is that the failure modes of real shapes are different from those of ellipsoids. To emphasize this feature, we proposed a shape classification in terms of their internal properties and failure modes and applied it to 21 test real shape modes, assuming that the actual friction angle is 40°. Those asteroids were categorized into four different shape types: spheroidal shapes failing

by structural failure (Type SF), ellipsoidal shapes experiencing either structural failure or surface shedding (Type EF or ES), and bifurcated shapes breaking into multi-components from the neck (Type BF). Type SF and EF look similar to perfect ellipsoidal shapes. On the other hand, features of Type ES and BF are different from those perfect ellipsoids. ES type asteroids experiences strong tension around their extremities at the limit spin at structural failure of a total volume, which leads the first shedding before structural failure, although ellipsoidal shapes need a friction angle of 90° to experience material shedding first (or, more precisely, at the same time as structural failure). This implies that shape diversities let the first shedding occur at lower friction angles. On the other hand, structural failure of BF type asteroids depends on their bifurcated structure. A body experiences a higher stress peak as its bifurcation becomes stronger. Those features plus a fast spin rate allowed us to constrain physical configuration of asteroids situated near the failure modes. For these objects, we determined the lower bound of their bulk density and re-evaluated the bulk density estimations by earlier works. In particular, we highly constrained the bulk density of (8567) 1996 HW1, a BF type asteroid, in the range between 0.7 and 1.1 g/cm^3.

Acknowledgements

Chapter 7

Application: the Breakup Event of P/2013 R3

7.1   Introduction

Recent years have seen several observations of a previously unrecognized class of small bodies, what have been called "Active Asteroids." These are bodies that display intermittent phenomenon traditionally associated with comets, yet which appear for bodies that are thought to be asteroids with no or minimal volatiles. A survey of recent observations is given in Jewitt et al. [81]; however, since that time, there have been several additional and striking examples of this phenomenon [83, 82]. It is important to note that the observed characteristics of these active asteroids are not uniformly similar. An excellent example of this is the contrast between bodies P/2013 P5 and P/2013 R3. The former was observed to have several streamers of dusty material emanating from a single main body at several different epochs in relatively close spacing. The latter, however, was observed to be components that were mutually escaping from each other, with these individual components undergoing additional fractures at later epochs. While the root cause of these events is thought to be rotational disruption [83, 82], the differing observed morphologies may indicate different modes of failure (e.g., [61]). Specifically, while P/2013 P5 may be indicative of mass-shedding of regolith from the surface of an asteroid, P/2013 R3 appears to be consistent with a body breaking into multiple components. In this chapter we focus on this latter active asteroid and, under the hypothesis that it was a single asteroid that underwent rotational disruption, develop constraints on its physical properties.

Analytical modeling of this body can provide clues about the origin and mechanism of these

events. We explore a model for the breakup of an ellipsoidal rubble pile that was firstly discussed in Scheeres et al. [153] and that was later expanded in Sánchez and Scheeres [135]. In the present model a body that has cohesion can be spun beyond the rate at which centrifugal accelerations can be balanced with mutual gravitational attractions. Depending on the strength of the cohesive bonds, which may be less than a few hundred pascals [135], at some spin rate the body may fracture along planes of weakness, with the components then departing each other on possibly hyperbolic orbits. The trigger for the fracture may be either a secular increase in spin rate due to the YORP effect, or a small impact that generates seismic waves that cause bonds close to the failure limit to fail [103].

Four images of P/2013 R3 taken at different epochs between October and December in 2013 show that this object experienced subsequent breakups [82]. It is reported that the proto-body has broken into more than 10 components as a result of this breakup event. The maximum size of the components may be on the order of a few hundred meters. In this chapter we assume that the YORP effect causes the body to spin up to its critical spin, so detailed discussions of the spin-up mechanism are omitted. Based on the observational estimates by Jewitt et al. [82], we derive the initial spin period and the cohesive strength of P/2013 R3. Additional observations of this system and more precise astrometric analysis of the observations may provide further constraints on the body.

7.2   Modeling of the Breakup Process

7.2.1   Breakup Scenario

Suppose that the proto-body uniformly rotates in a principal axis mode and is only subject to its self-gravitational, centrifugal, frictional and cohesive forces. If the proto-body spins fast enough, it can fail structurally and break up intomultiple components. The proto-body and the smaller components as a result of the breakup are assumed to be a biaxial ellipsoid and spheres, respectively. If shear strength is zero over some cross section, the breakup should start from this

cross section. However, if shear strength is nonzero, the body will keep its shape at a faster spin rate. Applying the Mohr-Coulomb yield criterion (e.g., [28]), we represent shear strength by a friction angle and cohesive strength. After a breakup, the components as a result of this event are inserted into their mutual orbits.

The breakup model shown in Fig. 7.1 defines two processes. Process 1 represents mechanical failure of the proto-body. The condition of this failure mode will be determined by considering the yield condition of the averaged stress over the central cross section. Process 2 describes its subsequent orbital motion as a result of mechanical failure. In general, since each component may be non-spherical, there is angular momentum transfer, resulting in a change of the spin vector during the initial disruption [158]; however, the critical region for such a transfer of angular momentum is only at distances of a few radii of each component [60]. For the case of P/2013 R3, since the initial velocity of the components are consistent with the system escape velocity [82], the shape effect on the transfer is negligible. Therefore, it is a reasonable simplification of the model to assume that each component is a sphere and that the initial spin state is conserved across the breakup.

We also assume that the entire process occurs in a plane. The initial condition of the translational velocity is determined by multiplying the spin rate by the relative distance between the centers of mass of the two components about to split, and its direction is taken to be perpendicular to the angular velocity of the proto-body. While there is evidence that fast rotators may tumble [126], since the normal vector of a failing cross section is always on the orbital plane, the critical component of the spin vector is identical to the component normal to the orbital plane; therefore, calculations of cohesive strength should be independent of other spin components and the initial spin rate given here is equivalent to its lower bound.

It is emphasized that the terms "breakup" and "structural failure", used by Hirabayashi and Scheeres [61], are distinguished in this study. The term "breakup" describes that a proto-body is split into smaller pieces, while the term "structural failure" indicates structural instability, meaning that the original shape permanently changes due to large plastic deformation, but does not necessarily break up into multiple components. If a body experiences centrifugal accelerations

exceeding gravitational accelerations, any deformation may lead to break up. A single breakup is discussed here, although the present technique can be applicable to any similar cascade of breakup events. We note that the dispersion velocity between different components is proportional to their relative distance. Thus, late-separate components may have split at a similar time as the main component; however, since their speeds are less, they may not have been distinguished until later.

We suppose that the dimensions of the proto-body are $2a$ by $2a\beta$ by $2a\beta$, where $0 < \beta < 1$, and the diameters of the smaller components, denoted as R, are chosen to be equal to a half of the volume of the proto-body. The proto-body uniformly rotates with a spin rate ω along its maximum principal axis. The density, ρ, is constant over the body.

7.2.2   Structural Breakup Condition (Process 1)

The assumption of equal sizes of the smaller components implies that the breakup occurs in the middle of the proto-body. This comes from the fact that the central cross section normal to the minimum principal axis is the most sensitive to failure. Table 2 in Jewitt et al. [82], showing the effective radii of the smaller components, also indicates that the components look similar.

To obtain the breakup condition, we use the gravitational potential at an arbitrary point inside a biaxial ellipsoid, which is written as

$$U(x,y,z) = \pi\rho G(-A_0 a^2 + A_x x^2 + A_y y^2 + A_z z^2), \tag{7.1}$$

where

$$A_0 = \beta^2 \int_0^\infty \frac{ds}{\Delta}, \tag{7.2}$$

$$A_x = \beta^2 \int_0^\infty \frac{ds}{(s+1)\Delta}, \tag{7.3}$$

$$A_y = A_z = \beta^2 \int_0^\infty \frac{ds}{(s+\beta^2)\Delta}, \tag{7.4}$$

and $\Delta = \sqrt{s+1}(s+\beta^2)$. See the details in [59].

The failure condition of the central cross section is given by considering the yield condition of the area stress over this cross section. To calculate the area stress, we use the technique proposed

by Davidsson [34]. The yield condition is characterized by the Mohr-Coulomb yield criterion, which is given in Eq. (3.1). Since the friction angle of a typical soil material ranges between $30°$ and $45°$ [91], by taking the mean of these friction angles, the spin rate of the yield condition, ω_p, is approximately described as

$$\omega_p \sim \sqrt{\frac{4Y}{\rho a^2} + 2\pi\rho G A_x}, \tag{7.5}$$

where G is the gravitational constant and A_x is described in Eq. (7.3). If $Y = 0$, $\omega_p = \sqrt{2\pi\rho G A_x}$, corresponding to the condition at which the pressure on the central cross section becomes zero and at which a breakup occurs. This is identical to the highest spin rate of structural failure of a cohesionless ellipsoid [161]. At this condition, the components as a result of a breakup do not fly off, but rest on each other without contact forces instead. We note that such configurations are dynamically unstable and can lead to escape after an extended period of dynamical interaction [148, 78, 124]. However, the case of P/2013 R3 is not consistent with this scenario as the components are seen to be immediately escaping from each other. For a body with cohesion, the spin rate of its breakup can be higher than that of any structural failure conditions and is high enough to lead to immediate escape (see the discussion on the lower size limit of binaries in [135]).

7.2.3   Mutual Orbit After the Breakup (Process 2)

The dispersion velocity of P/2013 R3 is 0.2 - 0.5 m/s at a relative distance of 3060 km (see Table 7.1), which is beyond the Hill sphere of the system, less than 250 km. This indicates that the small components are likely inserted in a hyperbolic orbit. Under this assumption, the following discussion explores the mutual orbit dynamics. The total energy conservation for irregular bodies is written as [142],

$$E = \int_B \frac{v^2}{2} dm - \frac{1}{2} \int_B \int_B \frac{Gdmdm}{r}, \tag{7.6}$$

where B indicates the entire body distribution. Note that the second term in Eq. (7.6) includes self-gravity potentials.

Consider the initial state, i.e., the configuration where P/2013 R3 is about to break up. Assuming that the proto-body is an ellipsoid with dimensions of $a \times a\beta \times a\beta$ yields

$$E_{initial} = \frac{1}{2}I\omega_0^2 + \frac{\rho}{2}\int_V U(x,y,z)dV, \tag{7.7}$$

where ω_0 is the initial spin rate, I is the moment of inertia of the proto-body, and $U(x,y,z)$ is given in Eq. (7.1). The first term on the right hand side in Eq. (7.7) is given as

$$\frac{1}{2}I\omega_0^2 = \frac{1}{10}Ma^2(1+\beta^2)\omega_0^2, \tag{7.8}$$

where M indicates the mass of the whole system, i.e., $M = 4\pi\rho a^3\beta^2/3$. The self-potential of an ellipsoid can be given as [143]

$$\frac{\rho}{2}\int_V U(x,y,z)dV = -\frac{2}{5}M\pi\rho Ga^2 A_0, \tag{7.9}$$

where A_0 is introduced in Eq. (7.2).

For the configuration at a post-disruption epoch, assuming that the components are spheres with the same radius $R = a(\beta^2/2)^{1/3}$, we describe the total energy as

$$
\begin{aligned}
E_{last} &= \frac{m_1 m_2 \Delta v^2}{2M} + \frac{1}{2}I_1\omega_0^2 + \frac{1}{2}I_2\omega_0^2 \\
&\quad -\frac{Gm_1 m_2}{d} - \frac{G}{2}\int_{m_1}\int_{m_1}\frac{dm_1 dm_1}{r} - \frac{G}{2}\int_{m_2}\int_{m_2}\frac{dm_2 dm_2}{r}, \\
&= \frac{1}{8}M\Delta v^2 - \frac{GM^2}{4d} + \frac{1}{5}MR^2\omega_0^2 - \frac{2}{5}M\pi\rho GR^2,
\end{aligned} \tag{7.10}
$$

where $m_1 = m_2 = M/2$, $I_1 = I_2 = MR^2/5$, Δv is the dispersion velocity, and d is the relative distance between two components at a given epoch.

From energy conservation, $E_{initial} = E_{last}$, leading to,

$$
\begin{aligned}
&\frac{1}{5}a^2(1+\beta^2)\omega_0^2 - \frac{4}{5}\pi\rho Ga^2 A_0 \\
&= \frac{1}{4}\Delta v^2 - \frac{GM}{2d} + \frac{2}{5}R^2\omega_0^2 - \frac{4}{5}\pi\rho GR^2.
\end{aligned} \tag{7.11}
$$

This relation can be solved for the initial spin rate ω_0 as

$$\omega_0 = \sqrt{\frac{\Phi}{\Psi}}, \tag{7.12}$$

where

$$\Psi = \frac{a^2}{5}\left((1+\beta^2) - 2\left(\frac{\beta^2}{2}\right)^{\frac{2}{3}}\right),$$

$$\Phi = \frac{\Delta v^2}{4} - \frac{2\pi\rho G a^3 \beta^2}{3d} - \frac{4\pi\rho G a^2}{5}\left(\frac{\beta^2}{2}\right)^{\frac{2}{3}} + \frac{4\pi\rho G a^2 A_0}{5}.$$

Assuming that Eq. (7.5) equals Eq. (7.12), the initial spin state can also be related to the minimum level of cohesion needed for this body.

7.3   Application to P/2013 R3

The observations by Jewitt et al. [82] provide the relative velocity and the distance between the components at some epochs (Table 7.1), although angle-of-view effects affect their plane-of-sky projections (Jewitt, personal communications, 2014). For the diameter of the proto-body, Jewitt et al. [82] reported that since they only measured the product, Area×Albedo = π Radius^2×Albedo, if the albedo is different, so is the estimated radius. The assumption of an albedo of 0.05 renders radius uncertainties by a factor of $\sqrt{2}$. Furthermore, although there is less dust in December than in October, there is still no guarantee that the dust has gone in December. Therefore, a radius from 0.2 km to 0.5 km defines the lowest and highest possibility of the radius of the proto-body[1] . However, based on the estimates on December 13, 2013, it is strongly suspected that the effective radius may be less than 0.35 km (Jewitt 2014, personal communication). On the other hand, the aspect ratios of asteroids, β, is considered to be larger than 0.5 (c.f., the asteroid LightCurve Data Base by Warner, Harris, and Pravec, revised on November 10, 2012). Given these estimates, the present analysis provides lower bounds on the initial spin period and cohesive strength.

Consider the first breakup event that occurred before October 1, 2013. Equations (7.5) and (7.12) provide the spin period of the proto-body relative to cohesive strength with different dispersion velocities and aspect ratios (Fig. 7.2). In the figure, the solid lines show the case $\beta = 0.5$, while the dashed lines describe the case $\beta = 1.0$. The upper curves are the possibly slowest spin

---

[1] A radius of 0.2 km is equal to the radius of the largest component, while that of 0.5 km is computed from the effective radii on October 1, 2013.

periods that result from a dispersion velocity of 0.2 m/s and a size of 1.0 km, while the lower curves are the possibly fastest spin periods that result from a dispersion velocity of 0.5 m/s and a size of 0.4 km. The actual initial spin period should be laid between the fastest and slowest spin periods. On a given curve, the bulk density increases as the spin period becomes shorter. The empty triangles and squares show the cases $\rho = 1000$ kg/m^3 and $\rho = 1500$ kg/m^3, respectively. If the density of this asteroid ranges between these values, then the initial spin period and cohesive strength are further constrained. From the distribution of the triangles and squares, for P/2013 R3, the cohesive strength ranges from 40 Pa to 210 Pa, while the initial spin period is between 0.48 hr and 1.9 hr. Note that in the range of friction angles of typical soils, i.e., $30°$ and $45°$, the cohesive strength changes up to a 20 % of the given values, while the initial spin period does not.

7.4   Discussion

Broadband optical colors show that this object may be a C-type asteroid [82]. This type of an asteroid has relatively low bulk densities; for example, the bulk density of (206) Mathilde ranges between 1100 kg/m^3 and 1500 kg/m^3 [193], while that of (101955) Bennu is on the order of 1250 kg/m^3 [29]. Thus, it is reasonable to consider that the bulk density of P/2013 R3 may be between 1000 kg/m^3 and 1500 kg/m^3. The empty triangles and squares in Fig. 7.2 give the end points for each curve; therefore, the actual configuration could likely be between these points. This provides the following two interpretations.

First, although the spin curve by Pravec et al. [127] implies that the spins of asteroids ranging from 0.4 km to 1.0 km in size may be bounded at the spin barrier, 2.2 hr, our result suggests that the breakup of P/2013 R3 could have occurred at a shorter spin period than the spin barrier. As shown in Fig. 7.2, the slowest spin period is 1.9 hr, occurring when $\rho = 1000$ kg/m^3, $2a = 1.0$ km, and $\Delta v = 0.2$ m/s. This condition may be an extreme case in our problem. Again, since the effective radius measured from the October 1, 2013 data is still affected by the dust cloud, Jewitt et al. [82] state that the 330 m effective radius measured from the December 13, 2013 data is more accurate. Thus, we believe that a size of 1.0 km ($> 2 \times 330$ m) may be too large. This explains

that the initial spin of this asteroid should be faster than the spin barrier.

Second, the possible cohesive strength ranges from 40 Pa to 210 Pa. This estimate is comparable to that inferred for rubble pile asteroids in Sánchez and Scheeres [135]. If P/2013 R3 is a rubble pile and the size distribution of its particles extends down to the μm level, then van der Waals forces may supply the needed cohesive strength for such an asteroid. The cohesive strength of a cohesive self-gravitating aggregate was determined by Sánchez and Scheeres[135] to be directly related to the average grain size and the Hamaker constant[2] . Using a Hamaker constant of $\sim$0.036 N/m, which is consistent with lunar regolith [123], for an asteroid with cohesive strength of 40 - 210 Pa and with a friction angle of 37.5°, we end up with an average particle size of 1.2 - 6.1 μm, consistent with the size range of the sample from (25143) Itokawa [180]. Therefore, it is reasonable to believe that a rubble-pile asteroid with hundreds of meters in size could have cohesive strength matching the values calculated through this analysis. Furthermore, the possibility that P/2013 R3 is a monolith is quite low because (i) for the present case cohesive strength is highly bounded and (ii) cohesive strength of a typical rock is at least on the order of 10 MPa [91, 80].

Based on the observations by [82], we showed the possible ranges of the initial spin period and cohesive strength of P/2013 R3. However, once additional observations of this asteroid are carried out, they will provide information that can give further constraints on this breakup event. Also, detailed analysis of the subsequent breakups in this event can also be used to develop additional constraints on these parameters.

Acknowledgements

---

[2] The Hamaker constant is directly related to the strength of the cohesive forces between any two bodies whose surfaces are in contact.
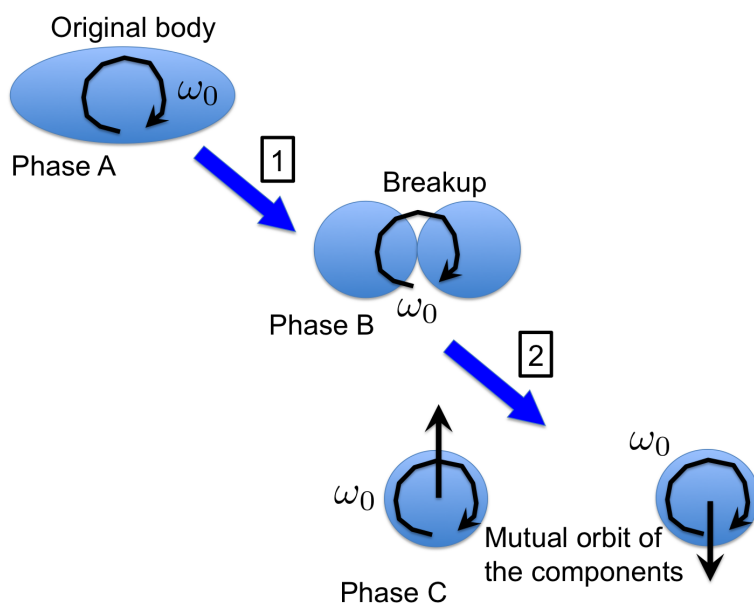
Figure 7.1: A model for a breakup. The proto-body (phase A) would break into two components (phase B) at the critical spin period, followed by orbital motions (phase C). At phase C, the different components may also be split, but would have mutual speeds that are lower. This event consists of two processes: process 1 being the transition from phase A to phase B and process 2 being that from phase B to phase C.
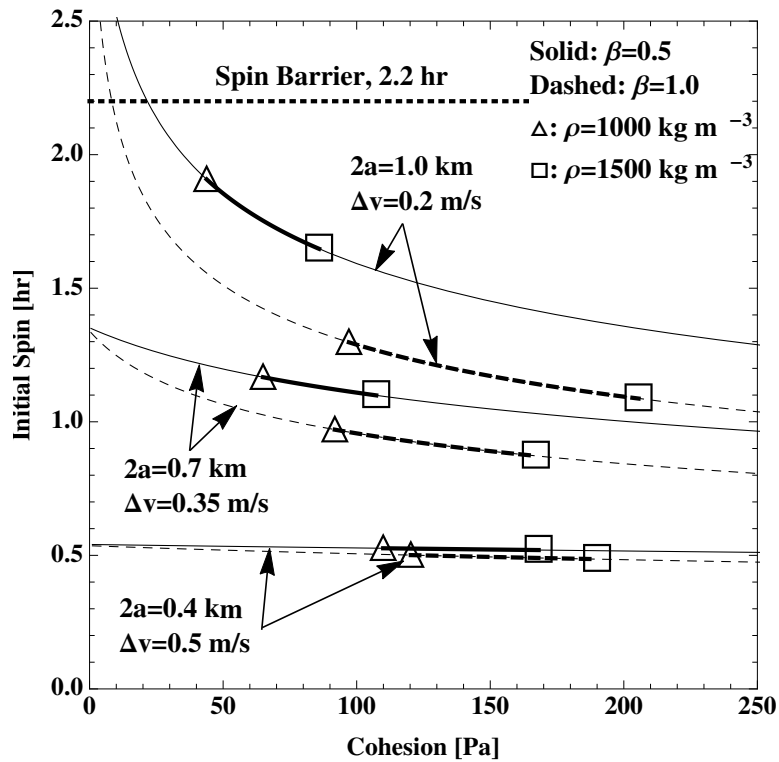
Figure 7.2: Possible initial spin period due to different dispersion velocities and initial sizes, i.e., Δv ranging from 0.2 m/s to 0.5 m/s and $2a$ from 0.4 km to 1.0 km (see Table 7.1). The solid lines show the initial spin period with $\beta = 0.5$, while the dashed lines describe that with $\beta = 1.0$. The actual spin periods should be laid between the fastest and slowest spin periods. The empty triangles and squares indicate bulk densities of 1000 kg/m³ and 1500 kg/m³, respectively; as a C-type asteroid, this asteroid should be between these points.

Table 7.1: Measured Properties of P/2013 R3

Property	Value	Reference
Relative Distance, d, [km] (Oct. 1, 2014)	3060	
Diameter of the Initial Body, $2a$, [km]	0.4 - 1.0	[82]
Relative Velocity, Δv, [m/s]	0.2 - 0.5	

Chapter 8

Conclusion

This thesis research explored the internal structure of (216) Kleopatra and its failure mode. We developed (i) a limit analysis technique for determining lower and upper bounds for structural failure of an irregular body, (ii) a dynamical analysis technique for giving a condition of surface shedding for a cohesionless case, and (iii) a finite element model taking into account plastic deformation.

First, on the assumption that a material is cohesionless, we considered the size effect on dynamical and structural stability of the shape of (216) Kleopatra at the current spin period. We separately investigated the conditions of surface shedding and structural failure. For the condition of structural failure, we obtained lower and upper bounds for structural failure of this object. An elastic finite element model showed that the internal stress configuration may be above a lower bound condition. The technique for giving the yield condition of the averaged stress over a partial volume demonstrated that the neck of (216) Kleopatra is the most sensitive to structural failure and, for a friction angle of 32°, a typical angle of a geological material, only the size scale ranging from 1.18 to 1.32 allows the body to be structurally stable. This result is consistent with the size estimate by the Descamps et al. (2011) size. For the condition of surface shedding, we constructed zero-velocity curves of this body to find constraints on the motion and the spin period at which the dynamical equilibrium point touches the surface. The result shows that (216) Kleopatra with a size scale between 1.0 and 1.5 cannot experience surface shedding shedding at the current spin period, and the satellites orbiting about this body do not result from the shedding process.

Second, removing the assumption of zero-cohesion, we investigate structural failure of this body by a finite element model. Focusing on the size estimates by Ostro et al. [117], Descamps et al. [36], and Marchis et al. [102], we constructed a finite element model involving plastic deformation. The constitutive model of plastic deformation was modeled based on a non-associated flow rule characterized by the Drucker-Prager criterion. Because of dependency of solutions on histories, the loading path was defined so that the gravitational and centrifugal forces were linearly incremented over the simulation process. Although this asteroid is spinning in free space, six degrees of freedom were artificially fixed to make calculations converge properly in our model. The prime result of this study was that it was necessary for (216) Kleopatra to have cohesive strength to keep its current shape. the Ostro et al. (2000) size, the Descamps et al. (2011) size, and the Marchis et al. (2012) size required apparent cohesive strength of 1.77×10^3 kPa, 2.54×10^2 kPa, and 6.85×10^2 kPa, respectively. For the failure modes of (216) Kleopatra, the Ostro et al. (2000) size would experience compression of the bottom of the neck, the Descamps et al. (2011) size would have global landslides on the surface, but would not have internal failure, and the Marchis et al. (2012) size would fail due to tension of the top of the neck. We concluded that (216) Kleopatra could be a rubble pile, but would be sensitive to different failure modes, depending on its sizes.

Third, we investigated the failure mode of 21 asteroids due to a YORP-type spin acceleration: surface shedding and structural failure. Using the techniques for determining surface shedding and for obtaining an upper bound condition of structural failure, we compared these modes of asteroids to determine a possible failure mode of them. The prime result is that the failure modes of real shapes are different from those of ellipsoids. We also proposed a shape classification to emphasize the effects on their failure modes. There are four different shape types: spheroidal shapes failing by structural failure (Type SF), ellipsoidal shapes experiencing either structural failure or surface shedding (Type EF or ES), and bifurcated shapes breaking into multi-components from the neck (Type BF). For some asteroids, since the current configuration may be close to their failure point, we could also constrain their bulk density.

Fourth, we studied the internal structure of P/2013 R3 by its breakup event. We demon-

strated that the initial spin period and cohesion can be constrained by its breakup event. The result showed that cohesion could be between 40 and 210 Pa, which is laid in the range of cohesion for a typical geological material and the initial spin period may range between 0.48 and 1.9 hr.

The technique will be quite useful for giving constraints on the internal structural of an asteroid once further observations are conducted.

Bibliography

[1] Shinsuke Abe, Tadashi Mukai, Naru Hirata, Olivier S. Barnouin-Jha, Andrew F. Cheng, Hirohide Demura, Robert W. Gaskell, Tatsuaki Hashimoto, Kensuke Hiraoka, Takayuki Honda, Takashi Kubota, Masatoshi Matsuoka, Takahide Mizuno, Ryosuke Nakamura, Daniel J. Scheeres, and Makoto Yoshikawa. Mass and local topography measurements of itokawa by hayabusa. Science, 312(5778):1344–1347, 2006.

[2] Joshua Ashenberg. Mutual gravitational potential and torque of solid bodies via inertia integrals. Celestial Mechanics and Dynamical Astronomy, 99:149–159, 2007.

[3] Erik Asphaug and Willy Benz. Size, density, and structure of comet shoemaker-levy 9 inferred from the physics of tidal breakup. Icarus, 1996.

[4] Erik Asphaug, Steven J. Ostro, R. S. Hudson, and Daniel J. Scheeres. Distruption of kilometre-sized asteroids by energetic collisions. Nature, 393:437–440, June 1998.

[5] Julie Bellerose and Daniel J. Scheeres. Energy and stability in the full two body problem. Celestial Mechanics and Dynamical Asronomy, 100:63–91, 2008.

[6] M. J. S. Belton, C. R. Chapman, P. C. Thomas, M. E. Davles, R. Greenberg, K. Klassen, D. Byrnes, L. D'Amario, S. Synnott, T. V. Johnson, A. McEwen, W. J. Merline, D. R. Davis, J-M. Petit, A. Storrs, J. Veverka, and B. Zellner. 243 ida from the orbit of its satellite dactyl. Nature, 374:785–788, 1995.

[7] Lance A. M. Benner, R. Scott Hudson, Steven J. Ostro, Keith D. Rosema, Jon D. Giorgini, Donald K. Yeomans, Raymond F. Jurgens, David L. Mitchell, Ron Winkler, Randy Rose, Martin A. Slade, Michael L. Thomas, and Petr Pravec. Radar observations and asteroid 2063 bacchus. Icarus, 139:309–327, 1999.

[8] Lance A. M. Benner and Steven J. Ostro. Asteroid radar research.

[9] N. Borderies. Mutual gravitational potential of n solid bodies. Celestial Mechanics, 18:295–307, 1978.

[10] William F. Bottke, Michael C. Nolan, Richard Greenberg, and Robert A. Kolvoord. Collisional lifetimes and impact statistics of near-earth asteroids. In Tom Gehrels, editor, Hazards due to comets & asteroids. The University of Arizona Press, 1994.

[11] William F. Bottke, Michael C. Nolan, Richard Greenberg, and Robert A. Kolvoord. Velocity distributions among colliding asteroids. Icarus, 107:255–268, 1994.

[12] Daniel T. Britt, Donald K. Yeomans, Kevin Housen, and G. Consolmangno. Asteroid density, porosity, and structure. In Jr. William F. Bottke, Alberto Cellino, Paolo Paolicchi, and Richard P. Binzel, editors, Asteroid III, pages 485–500. The University of Arizona Press, 2002.

[13] Dirk Brouwer and Gerald M. Clemence. Methods of Celestial Mechanics. Academic Press, 1961.

[14] Marina Brozovic, Lance A. M. Benner, Christopher Magri, Steven J. Ostro, Daniel J. Scheeres, Jon D. Giorgini, Michael C. Nolan, Jean-Luc Margot, Raymond F. Jurgens, and Randy Rose. Radar observations and a physical model of contact binary asteroid 4486 mithra. Icarus, 208:207–220, 2010.

[15] Marina Brozovic, Lance A. M. Benner, Patrick A. Taylor, Michael C. Nolan, Ellen S. Howell, Christopher Magri, Daniel J. Scheeres, John D. Giorgini, Joseph T. Pollock, Peter Pravec, Adrian Galad, Julia Fang, Jean-Luc Margot, Michael W. Busch, Michael K. Shepard, Daniel E. Reichart, Keven M. Ivarsen, Joshua B. Haislip, Aaron P. LaCluyze, Joseph Jao, Martin A. Slade, Kenneth J. Lawrence, and Michael D. Hicks. Radar and optical observations and physical modeling of triple near-earth asteroid (136617) 1994 cc. Icarus, 216:241–256, 2011.

[16] Marina Brozovic, Steven J. Ostro, Lance A. M. Benner, Jon D. Giorgini, Raymond F. Jurgens, Randy Rose, Michael C. Nolan, Alice A. Hine, Christopher Magri, Daniel J. Scheeres, and Jean-Luc Margot. Radar observations and a physical model of asteroid 4660 nereus, a prime space radar observation and a physical model of asteroid 4660 nereus, a prime space mission target. Icarus, 201:153–166, 2009.

[17] Schelte J. Bus and Richard P. Binzel. Phase ii of the small main-belt asteroid spectroscopic survey: A feature-based taxonomy. Icarus, 158:146–177, 2002.

[18] Michael W. Busch, Lance A. M. Benner, Steven J. Ostro, Jon D. Giorgini, Raymond F. Jurgens, Randy Rose, Daniel J. Scheeres, Christopher Magri, Jean-Luc Margot, Michael C. Nolan, and Alice A. Hine. Physical peroperties of near-earth asteroid (33342) 1998 wt24. Icarus, 195:614–621, 2008.

[19] Michael W. Busch, Jon D. Giorgini, Steven J. Ostro, Lance A. M. Benner, Raymond F. Jurgens, Randy Rose, Michael D. Hicks, Petr Pravec, Peter Kusnirak, Michael Ireland, Daniel J. Scheeres, Stephen B. Broschart, Christopher Magri, Michael C. Nolan, Alice A. Hine, and Jean-Luc Margot. Physical modeling of near-earth asteroid (29075) 1950 da. Icarus, 190:608–621, 2007.

[20] Michael W. Busch, Steven J. Ostro, Lance A. M. Benner, Marina Brozovic, Jon D. Giorgini, Joseph S. Jao, Daniel J. Scheeres, Christopher Magri, Michael C. Nolan, Ellen S. Howell, Patrick A. Taylor, Jean-Luc Margot, and Walter Brisken. Radar observations and the shape of near-earth asteroid 2008 ev5. Icarus, 212:649–660, 2011.

[21] Michael W. Busch, Steven J. Ostro, Lance A. M. Benner, Jon D. Giorgini, Raymond F. Jurgens, Randy Rose, Christopher Magri, Petr Pravec, Daniel J. Scheeres, and Stephen B. Brochart. Radar and optical observations and physical modeling of near-earth asteroid 10115 (1992 sk). Icarus, 181:145–155, 2006.

[22] Robin M. Canup and Larry W. Esposito. Accretion in the roche zone: Coexistence of rings and ringmoons. Icarus, 113:331–352, 1995.

[23] A. Cellino, R. Pannunzio, V. Zappala, P. Farinella, and P. Paolicchi. Do we observe light curves of binary asteroids? Astronomy and Astrophysics, 144:355–362, 1985.

[24] J. Chakrabarty. Theory of Plasticity. Elsevier Butterworth-Heinemann, third edition edition, 2006.

[25] Subrahmanyan Chandrasekhar. The virial theorem in hydromagnetics. Journal of Mathematical Analysis and Applications, 1:240–252, 1960.

[26] Subrahmanyan Chandrasekhar. Ellipsoidal Figures of Equilibrium. Yale University, 1963.

[27] Subrahmanyan Chandrasekhar. Ellipsoidal Figures of Equilibrium. Dover, 1987.

[28] W. F. Chen and D. J. Han. Plasticity for Structural Engineers. Springer-Verlag, 1988.

[29] Steven R Chesley, Davide Farnocchia, Michael C Nolan, David Vokrouhlickỳ, Paul W Chodas, Andrea Milani, Federica Spoto, Benjamin Rozitis, Lance AM Benner, William F Bottke, et al. Orbit and bulk density of the osiris-rex target asteroid (101955) bennu. Icarus, 235:5–22, 2014.

[30] C. Chree. The equations of an isotropic elastic solid in polar and cylindrical co-ordinates their solution and application. Transactions of the Cambridge Philosophical Society, 14:250, 1889.

[31] C. Chree. Xxxiii. some applications of physics and mathematics to geology. The London, Edinburgh, and Dublin philosophical magazine and journal of science, 32(196), September 1891.

[32] M. A. C. Chree. The equilibrium of an isotropic elastic solid ellipsoid under the action of normal surface forces of the second degree, and bodily forces derived from a potential of the second degree. Quarterly Journal, pages 89–118, 1886.

[33] Bjorn J. R. Davidsson. Tidal splitting and rotational breakup of solid sphere. Icarus, 142:525–535, 1999.

[34] Bjorn J. R. Davidsson. Tidal splitting and rotational breakup of solid biaxial ellipsoids. Icarus, 149:375–383, 2001.

[35] Imke de Pater and Jack J. Lissauer. Planetary Sciences. Cambridge University Press, second edition, 2010.

[36] P. Descamps, F. Marchis, J. Berthier, J.P. Emery, G. Duchêne, I. de Pater, M.H. Wongb, L. Lim, H.B. Hammel, F. Vachier, P. Wiggins, J.-P. Teng-Chuen-Yu, A. Peyrot, J. Pollock, M. Assafin, R. Vieira-Martins, J.I.B. Camargo, F. Braga-Ribas, and B. Macomber. Triplicity and physical characteristics of asteroid (216) kleopatra. Icarus, 211:1022–1033, 2011.

[37] Anthony R. Dobrovolskis. Internal stresses in phobs and other triaxial bodies. Icarus, 52:136–148, 1982.

[38] Anthony R. Dobrovolskis. Tidal disruption of solid bodies. Icarus, 88:24–38, 1990.

[39] David W. Dunham, Wayne Osborn, Glen Williams, Jack Brisbin, Andreas Gada, Toshio Hirose, Paul Maley, Harold Povenmire, James Stamm, Jeff Thrush, Chris Aikman, Murray Fletcher, Mitsuru Soma, and Wang Sichao. The sizes and shapes of (4) vesta, (216) kleopatra, and (381) myrrha from occultations observed during january 1991. In asteroids comets, meteors, page 54, 1991.

[40] Daniel D. Durda. The formation of asteroid satellites in catastrophic collisions. Icarus, 120:212–219, 1996.

[41] Daniel D. Durda, Jr. William F. Bottke, Brian L. Enke, William J. Merline, Erik Asphaug, Derek C. Richardson, and Zoe M. Leinhardt. The formation of asteroid satellites in large impacts: results from numerical simulations. Icarus, 167:382–396, 2004.

[42] Yoshiharu Eriguchi, Izumi Hachisu, and Daiichiro Sugimoto. Dumb-bell-shape equilibria and mass-shedding pear-shape of selfgravitating incompressible fuild. Progress of Theoretical Physics, 67(4):1068–1075, 1982.

[43] Larry Esposito. Planetary Rings. Cambridge University Press, 2006.

[44] Eugene G. Fahnestock, Taeyoung Lee, Melvin Leok, N. Harris McClamroch, and Daniel J. Scheeres. Polyhedral potential and variational integrator computation of the full two body problem. American Institute of Aeronautics and Astronautics, (6289), 2006.

[45] Eugene G. Fahnestock and Daniel J. Scheeres. Simulation of the full two rigid body problem using polyhedral mutual potential and potential derivatives approach. Celestial Mech. Dyn. Astr., 96:317–339, 2006.

[46] Eugene G. Fahnestock and Daniel J. Scheeres. Simulation and analysis of the dynamics of binary near-earth asteroid (66391) 1999kw4. Icarus, 194:410–435, 2008.

[47] Julia Fang, Jean-Luc Margot, Marina Brozovic, Michael C. Nolan, Lance A. M. Benner, and Patrick A. Taylor. Orbits of near-earth asteroid triples 2001 sn263 and 1994 cc: properties, origin, and evolution. The astronomical journal, 14(5), 2011.

[48] A. Fujiwara, Junichiro. Kawaguchi, Donald K. Yeomans, M. Abe, T. Mukai, T. Okada, J. Saito, Hajime Yano, Makoto Yoshikawa, Daniel J. Scheeres, O. Barnouin-Jha, Andrew F. Cheng, H. Demura, R. W. Gaskell, H. Ikeda, T. Kominato, H. Miyamoto, A. M. Nakamura, R. Nakamura, S. Sasaki, and K. Uesugi. The rubble-pile asteriod itokawa as observed by hayabusa. Science, 312:1330–1334, 2006.

[49] Robert Gaskell. Gaskell eros shape model v1.0. near-a-msi-5-erosshape-v1.0. Technical report, NASA Planetary Data System, 2008.

[50] Robert Gaskell, J. Saito, M. Ishiguro, T. Kubota, T. Hashimoto, N. Hirata, S. Abe, O. Barnouin-Jha, and Daniel J. Scheeres. Itokawa shape model v1.0. hay-a-amica-5-itokawashape-v1.0. Technical report, NASA Planetary Data System, 2008.

[51] G. E. O. Giacaglia and W. H. Jefferys. Motion of a space station. i. Celestial Mechanics, 4:442–467, 1971.

[52] V. Guibout and Daniel J. Scheeres. Stability of surface motion on a rotating ellipsoid. Celestial Mechanics and Dynamical Asronomy, 87:263–290, 2003.

[53] Ana H.F. Guimarães, Nicole Albers, Frank Spahn, Martin Seiß, Ernesto Vieira-Neto, and Nikolai V. Brilliantov. Aggregates in the strength and gravity regime: Particles sizes in saturn's rings. Icarus, 220:660–678, 2012.

[54] Alan W. Harris, Eugene G. Fahnestock, and Petr Pravec. On the shapes and spins of "rubble pile" asteroids. Icarus, 199:310–318, 2009.

[55] Sam Helwany. Applied Soil Mechanics with ABAQUS Applications. John Wiley and Sons, Inc., 2007.

[56] D. Hestroffer, J. Berthier, P. Descamps, P. Tanga, A. Cellino, M. Lattanzi, M. Di Martino, and V. Zappala. Asteroid (216) kleopatra tests of the radar-derived shape model. Astronomy and Astrophysics, 392:729–733, 2002.

[57] D. Hestroffer, F. Marchis, T. Fusco, and J. Berthier. Adaptive optics observations of asteroid (216) kleopatra. Astronomy and Astrophysics, 394:339–343, 2002.

[58] M. Hirabayashi, D. J. Scheeres, Paul Sánchez, and Travis Gabriel. Constraints on the physical properties of main belt comet p/2013 r3 from its breakup event. The Astrophysical Journal Letters, Submitted, 2014.

[59] Masatoshi Hirabayashi. Structural failure of two-density-layer cohesionless biaxial ellipsoids. Icarus, 236:178–180, 2014.

[60] Masatoshi Hirabayashi and Daniel J. Scheeres. Recursive computation of mutual potential between two polyhedra. Celestial Mechanics and Dynamical Asronomy, 117:245–262, 2013.

[61] Masatoshi Hirabayashi and Daniel J. Scheeres. Analysis of asteroid (216) Kleopatra using dynamical and structural constraints. The astrophysical journal, 780(2), 2014.

[62] E.W. Hobson. The Theory of Spherical And Ellipsoidal Harmonics. Cambridge University Press, 1931.

[63] Keith A. Holsapple. Equilibrium figures of spinning bodies with self-gravity. Icarus, 172:272–303, 2004.

[64] Keith A. Holsapple. Spin limits of solar system bodies: From the small fast-rotators to 2003 el61. Icarus, 187:500–509, 2007.

[65] Keith A. Holsapple. Spinning rods, elliptical disks and solid ellipsoidal bodies: Elastic and plastic stresses and limit spins. International journal of Non-Linear Mechanics, 43:733–742, 2008.

[66] Keith A. Holsapple. On the "strength" of the small bodies of the solar system: A review of strength theories and their implementation for analyses of impact disruptions. Planetary and Space Science, 57:127–141, 2009.

[67] Keith A. Holsapple. On yorp-induced spin deformations of asteroids. Icarus, 205:430–442, 2010.

[68] Keith A. Holsapple and Patrick Michel. Tidal disruptions: A continuum theory for solid bodies. Icarus, 183:331–348, 2006.

[69] Keith A. Holsapple and Patrick Michel. Tidal disruptions: Ii. a continuum theory for solid bodies with strength, with applications to the solar system. Icarus, 193:283–301, 2008.

[70] K. A. Hosapple. Equilibrium configurations of solid cohesionless bodies. Icarus, 154:432–448, 2001.

[71] Kevin R. Housen and Keith A. Holsapple. Scale effects in strength-dominated collisions of rocky asteroids. Icarus, 142:21–33, 1999.

[72] R. S. Hudson and S. J. Ostro. Physical model of asteroid 1620 geographos from radar and optical data. Icarus, 140:369–378, 1999.

[73] R. S. Hudson and S. J. Ostro. Physical model of asteroid 1620 geographos from radar and optical data. Icarus, 140:369–378, 1999.

[74] R. Scott Hudson and Steven J. Ostro. Shape of asteroid 4769 castalia (1989 pb) from inversion of radar images. Science, 264:940–943, 1994.

[75] R. Scott Hudson and Steven J. Ostro. Shape and non-principal axis spin state of asteroid 4179 toutatis. Science, 270:84–86, 1995.

[76] R. Scott Hudson, Steven J. Ostro, Raymond F. Jurgens, Keith D. Rosema, John D. Giorgini, Ron Winkler, Randy Rose, D. Choate, R. A. Cormier, C. R. Franck, and Robert Frye. Radar observations and physical model of asteroid 6489 golevka. Icarus, 148:37–51, 2000.

[77] R. Scott Hudson, Steven J. Ostro, Raymond F. Jurgens, Keith D. Rosema, John D. Giorgini, Ron Winkler, Randy Rose, D. Choate, R. A. Cormier, C. R. Franck, and Robert Frye. Radar observations and physical model of asteroid 6489 golevka. Icarus, 148:37–51, 2000.

[78] Seth A. Jacobson and Daniel J. Scheeres. Dynamics of rotationally fissioned asteroids: Source of observed small asteroid systems. Icarus, 214:161–178, 2011.

[79] Seth A. Jacobson and Daniel J. Scheeres. Dynamics of rotationally fissioned asteroids: Source of observed small asteroid systems. Icarus, 214:161–178, 2011.

[80] J. C. Jaeger and N. G. W. Cook. Fundamentals of Rock Mechanics. John Wiley & Sons, second edition, 1972.

[81] David Jewitt. The active asteroids. The Astronomical Journal, 143(3):66, 2012.

[82] David Jewitt, Jessica Agarwal, Jing Li, Harold Weaver, Max Mutchler, and Stephen Larson. Disintegrating asteroid P/2013 R3. The astrophysical journal letters, 784(L8):1–5, 2014.

[83] David C. Jewitt, Jessica Agarwal, Harold Weaver, Max Mutchler, and Stephen Larson. The extrordinary multi-tailed main-belt comet P/2013 P5. The astrophysical journal letters, 778:L21, 2013.

[84] David C. Jewitt, Harold Weaver, Jessica Agarwal, Max Mutchler, and Michal Drahus. A collision in 2009 as the origin of the debris trail of asteroid P/2010 A2. Nature, 467:817–819, 2010.

[85] Mikko Kaasalainen, Peter Pravec, Yurij N. Krugly, Lenka Sarounova, Johanna Torppa, Jenni Virtanen, Sanna Kaasalainen, Anders Erikson, Andreas Nathues, Josef Durech, Marek Wolf, Johan S. V. Lagerros, Mats Lindgren, Claes-Ingvar Lagerkvist, Robert Koff, John Davies, Rita Mann, Peter Kusnirak, Ninel M. Gaftonyuk, Vasilij G. Shevchenko, Vasilij G. Chiorny, and Irina N. Belskaya. Photometry and models of eight near-earth asteroids. Icarus, 167:178–196, 2004.

[86] Mikko Kaasalainen and Matti Viikinkoski. Shape reconstruction of irregular bodies with complementary data sources. Astronomy and Astrophysics, 543:A97, 2012.

[87] Jon Kadish, J. R. Barber, and P. D. Washabaugh. Stress in rotating spheres grown by accretion. International journal of solids and structures, 42:5322–5334, 2005.

[88] Jon Kadish, J.R. Barber, P. D. Washabaugh, and Daniel J. Scheeres. Stresses in accreted planetary bodies. Solids and structures, 45:540–550, 2008.

[89] Peter Kohnke. Theory Reference for the Mechanical APDL and Mechanical Applications. ANSYS, Inc., Southpointe 275 Technology Drive Canonsburg, PA 15317, 12.1 edition, 2009.

[90] Yu. N. Krugly, I. N. Belskaya, V. G. Chiorny, V. G. Shevchenko, and N. M. Gaftonyuk. Ccd photometry of near-earth asteroids in 2001. In Proceedings of Asteroids, Comets, Meteors - ACM 2002. International Conference, 29 July - 2 August 2002, Berlin, Germany. Ed. Barbara Warmbein. ESA SP-500. Noordwijk, Netherlands: ESA Publications Division, pages 903–906, 2002.

[91] T. William Lambe and Robert V. Whitman. Soil Mechanis. John Wiley & Sons, 1969.

[92] Zoe M. Leinhardt, Derek C. Richardson, and Thomas Quinn. Direct n-body simulations of rubble pile collisions. Icarus, 146:133–151, 2000.

[93] Sheueling Lien and James T. Kajiya. A symbolic method for calculating the integral properties of arbitrary nonconvex polyhedra. IEEE Computer Graphics and Applications, 4:35–41, 1984.

[94] A. E. H. Love. A Treatise on the Mathematical Theory of Elasticity. Cambridge University Press, 1944.

[95] Andrzej J. Maciejewski. Reduction, relative equilibria and potential in the two rigid bodies problem. Celestial Mechanics and Dynamics Astronomy, 63:1–28, 1995.

[96] William Duncan MacMillan. The Theory of The Potential. McGraw-Hill Book Company, 1930.

[97] Per Magnusson. Spin vectors of 22 large asteroids. Icarus, 85:229–240, 1990.

[98] Per Magnusson, M. Dahlgren, M. A. Barucci, L. Jorda, Richard P. Binzel, S. M. Slivan, C. Blanco, D. Riccioli, B. J. Buratti, F. Colas, J. Berthier, G. de Angelis, M. di Martino, E. Dotto, J. D. Drummond, U. Fink, M. Hicks, W. Grundy, W. Winsniewski, N. M. Gaftonyuk, E. H. Geyer, T. Bauer, M. Hoffmann, V. Ivanova, B. Komitov, Z. Donchev, P. Denchev, Yu. N. Krugly, F. P. Velichko, V.G. Chiorny, D. F. Lupishko, V. G. Shevchenko, T. Kwiatkowski, A. Kryszczynska, J. F. Lahulla, J. Licandro, O. Mendez, S. Mottola, A. Erikson, Steven J. Ostro, Petr Pravec, W. Pych, D. J. Tholen, R. Whiteley, W. J. Wild, M. Wolf,

and Lenka Sarounova. Photometric observations and modeling of asteroid 1620 geographos. Icarus, 123:227–244, 1996.

[99] Christopher Magri, S. J. Guy J. Consolmagno, Steven J. Ostro, Lance A. M. Benner, and Brett R. Beeney. Radar constraints on asteroid regolith properties using 433 eros as ground truth. Meteoritics and Planetary Science, 36:1697–1709, 2001.

[100] Christopher Magri, Ellen S. Howell, Michael C. Nolan, Patrick A. Taylor, Yanga R. Fernandez, Michael Mueller, Ronald J. Vervack Jr., Lance A. M. Benner, Jon D. Giorgini, Steven J. Ostro, Daniel J. Scheeres, Michael D. Hicks, Heath Rhoades, James M. Somers, Ninel M. Gaftonyuk, Vladimir V. Kouprianov, Yurij N. Krugly ad Igor E. Molotov, Michael W. Busch, Jean-Luc Margot, Vladimir Benishek, Vojislava Protitch-Benishek, Adrian Galad, David Higgins, Peter Kusnirak, and Donald P. Pray. Radar and photometric observations and shape modeling of contact binary near-earth asteroid (8567) 1996 hw1. Icarus, 214:2011–227, 2011.

[101] Christopher Magri, Steven J. Ostro, Daniel J. Scheeres, Michael C. Nolan, Jon D. Giorgini, Lance A. M. Benner, and Jean-Luc Margot. Radar observations and a physical model of asteroid 1580 betulia. Icarus, 186:152–177, 2007.

[102] F. Marchis, J.E. Enriquez, J.P. Emery, M. Mueller, M. Baek, J. Pollock, M. Assafin, R. Vieira Martins, J. Berthier, F. Vachier, D.P. Cruikshank, L.F. Lim, D.E. Reichart, K.M. Ivarsen, J.B. Haislip, and A.P. LaCluyze. Multiple asteroid systems: Dimensions and thermal properties from spitzer space telescope and ground-based observations. Icarus, 221:1130–1161, 2012.

[103] Francesco Marzari, Alessandro Rossi, and Daniel J. Scheeres. Combined effect of yorp and collisions on the rotation rate of small main belt asteroids. Icarus, 214:622–631, 2011.

[104] Patrick Michel, Willy Benz, and Derek C. Richardson. Catastrophic disruption of asteroids and family formation: a review of numerical simulations including both fragmentation and gravitational reaccumulations. Planetary and Space Science, 52(12):1109 – 1117, 2004. Catastrophic Disruption of Small Solar System Bodies.

[105] Patrick Michel, Willy Benz, Paolo Tanga, and Derek C. Richardson. Collisions and gravitational reaccumulation: Forming asteroid families and satellites. Science, 294(5547):1696–1700, 2001.

[106] Patrick Michel, Paolo Tanga, Willy Benz, and Derek C. Richardson. Formation of asteroid families by catastrophic disruption: Simulations with fragmentation and gravitational reaccumulation. Icarus, 160:10–23, 2014.

[107] J. K. Miller, A.S. Konopliv, P. G. Antreasian, J. J. Bordi, S. Chesley, C. E. Helfrich, W. M. Owen, T. C. Wang, B. G. Williams, D. K. Yeomans, and Daniel J. Scheeres. Determination of shape, gravity, and rotational state of asteroid 433 eros. Icarus, 155:3–17, 2002.

[108] David A. Minton. The topographic limits of gravitationally bound, rotating sand piles. Icarus, 195:698–704, 2008.

[109] David L. Mitchell, Steven J. Ostro, and Keith D. Rosema. Radar observations of asteroid 7 iris, 9 metis, 12 victoria, 216 kleopatra, and 654 zelinda. Icarus, 118:105–131, 1995.

[110] O. Montenbruck. Satellite Orbits, Models, Methods, and Applications. Springer, 2000.

[111] Carl D. Murray and Stanley F. Dermott. Solar System Dynamics. Cambridge University Press, 1999.

[112] R. M. Nedderman. Statics and Kinematics of Granular Materials. Cambridge University Press, 1992.

[113] Keiji Ohtsuki. Capture probability of colliding planetesimals: Dynamical constraints on accretion of planets, satellites, and ring particles. Icarus, 106:228–246, 1993.

[114] S. J. Ostro, Donald B. Campbell, and Irwin I. Shapiro. Mainbelt asteroid: Dual-polarization radar observations. Science, 229:442–446, 1985.

[115] Steven J. Ostro, John F. Chandler, Alice A. Hine, Keith D. Rosema, Irwin I. Shapiro, and Donald K. Yeomans. Radar images of asteroid 1989 pb. Science, 248:1523–1528, 1990.

[116] Steven J. Ostro, R. Scott Hudson, Lance A. M. Benner, Michael C. Nolan, Jon D. Giorgini, Daniel J. Scheeres, Raymond F. Jurgens, and Randy Rose. Radar observations of asteroid 1998 ml14. Meteoritics and Planetary Science, 36:1225–1236, 2001.

[117] Steven J. Ostro, R. Scott Hudson, Michael C. Nolan, Jean-Luc Margot, Daniel J. Scheeres, Donald B. Campbell, Christopher Magri, Jon D. Giorgini, and Donald K. Yeomans. Radar observations of asteroid 216 kleopatra. Science, 288:836–839, 2000.

[118] Steven J. Ostro, Raymond F. Jurgens, Keith D. Rosema, Jon D. Giorgini, Ron Winkler, Donald K. Yeomans, Dennis Choate, Randy Rose, Martin A. Slade, S. Denise Howard, Daniel J. Scheeres, and David L. Mitchell. Radar observations of asteroid 1620 geographos. Icarus, 121:44–66, 1996.

[119] Steven. J. Ostro, Jean-Luc Margot, Lance A. M. Benner, Jon D. Giorgini, Daniel J. Scheeres, Eugene G. Fahnestock, Stephen B. Broschart, Julie Bellerose, Michael C. Nolan, Christopher Magri, Petr Pravec, Petr Scheirich, Randy Rose, Raymond F. Jurgens, Eric M. De Jong, and Shigeru Suzuki. Radar imaging of binary near-earth asteroid (66391) 1999 KW4. Science, 314(5803):1276–1280, 2006.

[120] Steven J. Ostro, Jean-Luc Margot, Lance A. M. Benner, Jon D. Giorgini, Daniel J. Scheeres, Eugene G. Fahnestock, Stephen B. Broschart, Julie Bellerose, Michael C. Nolan, Christopher Magri, Petr Pravec, Petr Scheirich, Randy Rose, Raymond F. Jurgens, Eric M. De Jong, and Shigeru Suzuki. Radar imaging of binary near-earth asteroid (66391) 1999kw4. Science, 314:1276–1280, 2006.

[121] Steven J. Ostro, Petr Pravec, Lance A. M. Benner, R. Scott Hudson, Lenka Sarounova, Michael D. Hicks, David L. Rabinowits, James V. Scotti, David J. Tholen, Marek Wolf, Raymond F. Jurgens, Michael L. Thomas, Jon D. Giorgini, Paul W. Chodas, Donald K. Yeomans, Randy Rose, Robert Frye, Keith D. Rosema, Ron Winkler, and Martin A. Slade. Radar and optical observations of asteroid 1998 ky26. Science, 285:557, 1999.

[122] M. K. Paul. An expansion in power series of mutual potential for gravitating bodies with finite sizes. Celestial Mechanics, 44:49–59, 1988.

[123] H. Perko, J. Nelson, and W. Sadeh. Surface Cleanliness Effects on Lunar Regolith Shear Strength, chapter 94, pages 689–698. American Society of Civil Engineers, 1996.

[124] P. Pravec, D. Vokrouhlický, D. Polishook, D. J. Scheeres, A. W. Harris, A. Galád, O. Vaduvescu, F. Pozo, A. Barr, P. Longa, F. Vachier, F. Colas, D. P. Pray, J. Pollock, D. Reichart, K. Ivarsen, J. Haislip, A. LaCluyze, P. Kušnirák, T. Henych, F. Marchis, B. Macomber, S. A. Jacobson, Y. N. Krugly, A. V. Sergeev, and A. Leroy. Formation of asteroid pairs by rotational fission. Nature, 466(7310):1085–1088, 2010.

[125] Petr Pravec and Alan W. Harris. Binary asteroid population 1. angular momentum content. Icarus, 190:250–259, 2007.

[126] Petr Pravec, Alan W. Harris, P. Scheirich, P. Kušnirák, L. Šarounová, C. W. Hergenrother, S. Mottola, M. D. Hicks, G. Masi, Yu. N. Krugly, V. G. Shevchenko, Michael C. Nolan, E. S. Howell, Mikko Kaasalainen, A. Galád, P. Brown, D. R. DeGraff, J. V. Lambert, W. R. Cooney, Jr., and S. Foglia. Tumbling asteroids. Icarus, 173:108–131, 2005.

[127] Petr Pravec, Alan W. Harris, and B. D. Warner. Nea rotations and binaries. Near Earth Objects, our Celestial Neighbors: Opportunity and Risk, Proceedings IAU Symposium, (236), 2007.

[128] Petr Pravec, Marek Wolf, and Lenka Sarounova. Lightcurves of 26 near-earth asteroids. Icarus, 136:124–153, 1998.

[129] William H. Press, Saul A. Teukolsky, William T. Vetterling, and Brian P. Flannery. Numerical Recipes The Art of Scientific Computing, Third Edition. Cambridge University Press, 2007.

[130] N. Rambaux and E. Bois. Theory of the mercury's spin-orbit motion and analysis of its main librations. Astronomy and Astrophysics, 413:381–393, 2004.

[131] Derek C. Richardson. Tree code simulations of planetary rings. Monthly Notices of the Royal Astronomical Society, 269(2):493–511, July 1994.

[132] Derek C. Richardson, Thomas Quinn, Joachim Stadel, and George Lake. Direct large-scale n-body simulations of planetesimal dynamics. Icarus, pages 45–49, 2000.

[133] Derek C. Richardson, Jr. William F. Bottke, and Stanley G. Love. Tidal distortion and disruption of earth-crossing asteroids. Icarus, 134:47–76, 1998.

[134] David Parry Rubincam. Radiative spin-up and spin-down of small asteroids. Icarus, 148:2–11, 2000.

[135] Paul Sánchez and D. J. Scheeres. The strength of regolith and rubble pile asteroids. Meteoritics & Planetary Science, 49(5):788–811, 2014.

[136] Paul Sanchez and Daniel J. Scheeres. Simulating asteroid rubble piles with a self-gravitating soft-sphere distinct element mothed model. The astrophysical journal, 727:120, February 2011.

[137] Paul Sanchez and Daniel J. Scheeres. Dem simulation of rotation-induced reshaping and disruption of rubble-pile asteroids. Icarus, 2012.

[138] Franco Scaltriti and Vincenzo Zappala. Photoelectric photometry of asteroids 37, 80, 97, 216, 270, 313, and 471. Icarus, 34:428–435, 1978.

[139] H. Schaub and J. L. Junkins. Analytical mechanics of space systems, 2nd ed. AIAA education series, 2009.

[140] Daniel J. Scheeres. Dynamics about uniformly rotating triaxial ellipsoids: Applications to asteroids. Icarus, 110:225–238, 1994.

[141] Daniel J. Scheeres. The effect of c22 on orbit energy and angular momentum. Celestial Mechanics and Dynamical Asronomy, 73:339–348, 1999.

[142] Daniel J. Scheeres. Stability in the full two-body problem. Celestial Mechanics and Dynamics Astronomy, 83:155–169, 2002.

[143] Daniel J. Scheeres. Bounds on rotation periods of disrupted binaries in the full 2-body problem. Celestial Mechanics and Dynamical Astronomy, 89:127–140, 2004.

[144] Daniel J. Scheeres. Relative equilibria for general gravity fields in the sphere-restricted full 2-body problem. Celestial Mechanics and Dynamical Asronomy, 94:317–349, 2006.

[145] Daniel J. Scheeres. The dynamical evolution of uniformly rotating asteroids subject to yorp. Icarus, 188:430–450, 2007.

[146] Daniel J. Scheeres. Rotation fission of contact binary asteroids. Icarus, 189:370–385, 2007.

[147] Daniel J. Scheeres. Minimum energy asteroid reconfigurations and catastrophic disruptions. Planetary and Space Science, 57:154–164, 2009.

[148] Daniel J. Scheeres. Stability of the planar full 2-body problem. Celestial Mechanics and Dynamical Asronomy, 104:103–128, 2009.

[149] Daniel J. Scheeres. Stability of the planar full 2-body problem. Celestial Mechanics and Dynamics Astronomy, 104:103–128, 2009.

[150] Daniel J. Scheeres. Orbital motion in strongly perturbed environments: Applications to Asteroid, Comet, and Planetary Satellite Orbiters. Springer, 2012.

[151] Daniel J. Scheeres, Eugene G. Fahnestock, Steven J. Ostro, Jean-Luc Margot, Lance A. M. Benner, Stephen B. Broschart, Julie Bellerose, John D. Giorgini, Michael C. Nolan, Christopher Magri, Petr Pravec, Petr Scheirich, Randy Rose, Raymond F. Jurgens, Eric M. De Jong, and Shigeru Suzuki. Dynamical configration of binary near-earth asteroid (66391) 1999 kw4. Science, 314:1280–1283, 2006.

[152] Daniel J. Scheeres, Eugene G. Fahnestock, Steven J. Ostro, Jean-Luc Margot, Lance A. M. Benner, Stephen B. Broschart, Julie Bellerose, John D. Giorgini, Michael C. Nolan, Christopher Magri, Petr Pravec, Petr Scheirich, Randy Rose, Raymond F. Jurgens, Eric M. De Jong, and Shigeru Suzuki. Dynamical configration of binary near-earth asteroid (66391) 1999 kw4. Science, 314:1280–1283, 2006.

[153] Daniel J. Scheeres, Christine M. Hartzell, Paul Sanchez, and Micheal Swift. Scaling forces to asteroid surfaces: The role of cohesion. Icarus, 210:968–984, 2010.

[154] Daniel J. Scheeres and S. J. Ostro. Orbits close to asteroid 4769 castalia. Icarus, 121:67–87, 1996.

[155] Daniel J. Scheeres and S. J. Ostro. Orbits close to asteroid 4769 castalia. Icarus, 121:67–87, 1996.

[156] Daniel J. Scheeres, Steven J. Ostro, and R. Scott Hudson. Dynamics of orbits close to asteroid 4179 toutatis. Icarus, 132:53–79, 1998.

[157] Daniel J. Scheeres, Steven J. Ostro, Robert A. Werner, E. Asphaug, and R. Scott Hudson. Effects of gravitational interations on asteroid spin states. Icarus, 147:106–118, 2000.

[158] DJ Scheeres, SJ Ostro, RA Werner, E Asphaug, and RS Hudson. Effects of gravitational interactions on asteroid spin states. Icarus, 147(1):106–118, 2000.

[159] B. E. Schutz. The mutual potential and gravitational torques of two bodies to fourth order. Celestial Mechanics and Dynamical Asronomy, 24:173–181, 1981.

[160] Ronald F Scott. Principles of Soil Mechanics. Addison-Wesley, 1963.

[161] Ishan Sharma. The equilibrium of rubble-pile satellites: The darwin and roche ellipsoids for gravitationally held granular aggregates. Icarus, 200:636–654, 2009.

[162] Ishan Sharma. Equilibrium shapes of rubble-pile binaries: The darwin ellipsoids for gravitationally held granular aggregates. Icarus, 205:638–657, 2010.

[163] Ishan Sharma. Structural stability of rubble-pile asteroids. Icarus, 223:367–382, 2013.

[164] Ishan Sharma, James T. Jenkins, and Joseph A. Burns. Tidal encounters of ellipsoidal granular asteroids with planets. Icarus, 183:312–330, 2006.

[165] Ishan Sharma, James T. Jenkins, and Joseph A. Burns. Dynamical passage to approximate equilibrium shapes for spinning, gravitating rubble asteroids. Icarus, 200:304–322, 2009.

[166] Michael K. Shepard, Beth Ellen Clark, Michael C. Nolan, Lance A. M. Benner, Steven J. Ostro, Jon D. Giorgini, Faith Vilas, Kandy Jarvis, Susan Lederer, Lucy F. Lim, Tim McConnochie, James Bell, Jean-Luc Margot, Andrew S. Rivkin, Christopher Magri, Daniel J. Scheeres, and Peter Pravec. Multi-wavelength observations of asteroid 2100 ra-shalom. Icarus, 193:20–38, 2008.

[167] Michael K. Shepard, Jean-Luc Margot, Christopher Magri, Michael C. Nolan, Jpsua Schlieder, Benjamin Estes, Schelte J. Bus, Eric L. Volquardsen, Andrew S. Rivkin, Lance A. M. Benner, Jon D. Giorgini, Steven J. Ostro, and Michael W. Busch. Radar and infrared observations of binary near-earth asteroid 2002 ce26. Icarus, 184:198–210, 2006.

[168] Michael K. Shepard, Jean-Luc Margot, Christopher Magri, Michael C. Nolan, Jpsua Schlieder, Benjamin Estes, Schelte J. Bus, Eric L. Volquardsen, Andrew S. Rivkin, Lance A. M. Benner, Jon D. Giorgini, Steven J. Ostro, and Michael W. Busch. Radar and infrared observations of binary near-earth asteroid 2002 ce26. Icarus, 184:198–210, 2006.

[169] Micheal K. Shepard, Lance A. M. Benner, Steven J. Ostro, Alan W. Harris, Keith D. Rosema, Irwin I. Shapiro, John F. Chandler, and Donald B. Campbell. Radar observations of asteroid 2100 ra-shalom. Icarus, 147:520–529, 2000.

[170] Colin Snodgrass, Cecilia Tubiana, Jean-Baptiste Vincent, Holger Sierks, Stubbe Hviid, Richard Moissl, Hermann Boehnhardt, Cesare Barbieri, Detlef Koschny, Philippe Lamy, Hans Rickman, Rafael Rodrigo, Benoit Carry, Stephen C. Lowry, Ryan J. M. Laird, Paul R. Weissman, Alan Fitzsimmons, Simone Marchi, and the OSIRIS team. A collision in 2009 as the origin of the debris trail of asteroid P/2010 A2. Nature, 467:814–816, 2010.

[171] Stein Sture, Nicholas C. Costes, Susan N. Batiste, Mark R. Lankton, Khalid A. AlShibli, Boris Jeremic, Roy A. Swanson, and Melissa Franck. Mechanics of granular materials at low effective stresses. Journal of Aerospace Engineering, 11:67–72, 1998.

[172] Raymond Sullivan, R. Anderson, J. Biesiadecki, T. Bond, and H. Stewart. Cohesions, friction angles, and other physical properties of martian regolith from mars exploration rover wheel trenches and wheel scuffs. Journal of Geophysical Research, 116(E02006), 2011.

[173] S. Takahashi, K. Shinokawa, F. Yoshida, T. Mukai, W. H. Ip, and K. Kawabata. Photometric and polarimetric observations and model simulations of (216) kleopatra. Earth Planets Space, 56:997–1004, 2004.

[174] P. Tanga, D. Hestroffer, J. Berthier, A. Cellino, M. G. Lattanzi, M. Di Martino, and Vincenzo Zappala. Hst/fgs observations of the asteroid (216) kleopatra. Icarus, 153:451–454, 2001.

[175] Edward F. Tedesco, Paul V. Noah, Meg Noah, and Stephan D. Price and. The supplemental iras minor planet survey. The astrophysical journal, 123:1056–1085, February 2002.

[176] David James Tholen. Asteroid Taxonomy from Cluster Analysis of Photometry. PhD thesis, The University of Arizona, 1984.

[177] P. C. Thomas, M. J. S. Belton, B. Carcich, C. R. Chapman, M. E. Davies, R. Sullivan, and J. Veverka. The shape of ida. Icarus, 120:20–32, 1996.

[178] Pasquale Tricarico. Figure-figure interaction between bodies having arbitrary shapes and mass distributions: a power series expansion approach. Celestial Mechanics and Dynamical Astronomy, 100:319–330, 2008.

[179] Dimitrios Tsoulis, Olivier Jamet, Jerome Verdum, and Nicolas Gonindard. Recursive algorithm for the computation of the potential harmonic coefficients of a constant density polyhedron. J Geod, 83:925–942, 2009.

[180] Akira Tsuchiyama, Masayuki Uesugi, Takashi Matsushima, Tatsuhiro Michikami, Toshihiko Kadono, Tomoki Nakamura, Kentaro Uesugi, Tsukasa Nakano, Scott A. Sandford, Ryo Noguchi, Toru Matsumoto, Junya Matsuno, Takashi Nagano, Yuta Imai, Akihisa Takeuchi, Yoshio Suzuki, Toshihiro Ogami, Jun Katagiri, Mitsuru Ebihara, Trevor R. Ireland, Fumio Kitajima, Keisuke Nagao, Hiroshi Naraoka, Takaaki Noguchi, Ryuji Okazaki, Hisayoshi Yurimoto, Michael E. Zolensky, Toshifumi Mukai, Masanao Abe, Toru Yada, Akio Fujimura, Makoto Yoshikawa, and Junichiro Kawaguchi. Three-dimensional structure of hayabusa samples: Origin and evolution of itokawa regolith. Science, 333:1125–1128, 2011.

[181] David Vokrouhlický and David Čapek. Yorp-induced long-term evolution of the spin state of small asteroids and meteroids: Rubincam's approximation. Icarus, 159:449–467, 2002.

[182] Curt von Braun. The Gravitational Potential of Two Arbitrary Rotating Bodies with Applications to the Earth-Moon System. PhD thesis, The University of Texas at Austin, 1991.

[183] Kevin J. Walsh, Derek C. Richardson, and Patrick Michel. Rotational breakup as the origin of small binary asteroids. Nature, 454:188–191, 2008.

[184] Kevin J. Walsh, Derek C. Richardson, and Patrick Michel. Spin-up of rubble-pile asteroids: Disruption, satellite formation, and equilibrium shapes. Icarus, 220:514–529, 2012.

[185] P. D. Washabaugh and Daniel J. Scheeres. Energy and stress distributions in ellipsoids. Icarus, 159:314–321, 2002.

[186] S. J. Weidenschilling. Hektor: Nature of origin of a binary asteroid. Icarus, 44:807–809, 1980.

[187] Robert A. Werner. The gravitational potential of a homogeneous polyhedron or don't cut corners. Celestial Mechanics and Dynamical Asronomy, 59:253–278, 1994.

[188] Robert A. Werner. Spherical harmonic coefficients for the poltential of a constant-density polyhedron. Computers and Geosciences, 23(10):1071–1077, 1997.

[189] Robert A. Werner and Daniel J. Scheeres. Exterior gravitation of polyhedron derived and compared with harmonic and mason gravitation represenations of asteroid 4769 castalia. Celestial Mechanics and Dynamical Asronomy, 65:313–344, 1997.

[190] Robert A. Werner and Daniel J. Scheeres. Mutual potential of homogeneous polyhedra. Springer, 91:337–349, October 2005.

[191] Eugene P. Wigner. Group Theory and its Application to the Quantum Mechanics of Atomic Spectra. Academic Press, 1959.

[192] Hajime Yano, T. Kubota, H. Miyamoto, T. Okada, Daniel J. Scheeres, Y. Takagi, K. Yoshida, M. Abe, O. Barnouin-Jha, A. Fujiwara, S. Hasegawa, T. Hashimoto, M. Ishiguro, M. Kato, J. Kawaguchi, J. Saito, S. Sasaki, and M. Yoshikawa. Touchdown of the hayabusa spacecraft at the muses sea on itokawa. Science, 312:1350–1353, 2006.

[193] Donald K. Yeomans, J.-P. Barriot, D. W. Dunham, R. W. Farquhar, J. D. Giorgini, C. E. Helfrich, A. S. Konopliv, J. V. McAdams, J. K. Miller, W. M. Owen Jr., Daniel J. Scheeres, S. P. Synnott, and B. G. Williams. Estimating the mass of asteroid 253 mathilde from tracking data during the near flyby. Science, 278:2106–2109, 1997.

[194] Yang Yu and Hexi Baoyin. Orbital dynamics in the vicinity of asteroid 216 kleopatra. The astronomical journal, 143:62–71, 2012.

[195] Yang Yu and Hexi Baoyin. Resonant orbits in the vicinity of asteroid 216 kleopatra. Astrophysics and Space Science, 343:74–82, 2013.

[196] Vincenzo Zappala, M. Di Martino, and Franco Scaltriti. Photoelectric analysis of asteroid 216 kleopatra: Implications for its shape. Icarus, 53:458–464, 1983.